# Durham E-Theses

*Tem and Cathodoluminescence investigations of CdS grown by different techniques*

Mam, Keriya

# TEM AND CATHODOLUMINESCENCE INVESTIGATIONS OF CdS GROWN BY DIFFERENT TECHNIQUES

By
## Keriya MAM, BSc, MSci

*A thesis presented in candidature for the degree of Master of Philosophy in the University of Durham*

*Department of Physics*
*2005*

# Abstract

This work presents the results of an investigation of cadmium sulphide with various characterisation techniques such as TEM-Cathodoluminescence, SEM, XRD, PL and optical transmittance.

A model based on a convolution method is proposed to predict CL signal emission. It was assumed that the CL can originate from electron and X-ray sources. Measurement of CL signal and noise over a wide range of magnifications showed that signal-to-noise is too low when STEM is operating at higher magnifications than 3000 times. This may lead to some extent to some CL imaging limitations. The origin of this phenomenon is discussed.

A study of the suitability of a combined transmission electron microscope (TEM)/cathodoluminescence (CL) imaging and spectroscopy apparatus for investigations of CdS is presented. Photoluminescence (PL) was used to evaluate the effect of the $Ar^+$ and $I^+$ ion beam thinning used in TEM specimen preparation of CdS: a minor increase in yellow emission (594 nm) resulted. However, excitation of luminescence spectra in the TEM had a quenching effect on red luminescence (734 nm), this being considered due to the high excitation density compared to that in PL. Significant electron beam damage to the CdS single crystal could be avoided by using scanning transmission electron microscope (STEM) illumination in preference to the conventional TEM mode. Dislocation images were correlated with contrast in the STEM-CL imaging mode. The potential of the apparatus to make further direct correlations of CL images with diffraction contrast TEM imaging was assessed using the Rose visibility criterion.

Finally, optical and structural properties of thin films CdS grown by chemical bath deposition and metal organic chemical deposition were investigated. For both growth methods, TEM diffraction pattern confirm that the crystallographic structure of CdS was hexagonal, with a strong selected (002) orientation. It was found that either air annealing or $CdCl_2$ treatment on CBD CdS increased modestly the grain size of 6 nm. While for MOCVD CdS, the growth temperature and the II/VI play an important role in obtaining large grain. Hence, sample grown at 330°C with a II/VI of 0.78 revealed a better crystalline quality due to the presence of the excitonic bound centred around 2.55 eV and exhibited the largest grains of about 97 nm.

# Declaration

I declare that with the exception of those procedures listed below all the work presented in this thesis was carried out by the candidate. I also declare that none of this work has previously been submitted for any degree and that it is not being submitted for any other degree.

Samples were provided by:

Dr. A. Szczerbakow, Institute of Physics, Polish Academy of Sciences, Warsaw, Poland: CdS single crystal.

Pr. S.J.C. Irvine, Opto-electronic Materials Research Laboratory, North East Wales Institute: all MOCVD CdS samples

Mr M.D. Archbold, Department of Physics, Durham University, Durham, UK: all CBD CdS samples

........................................
Dr. K. Durose
Supervisor

........................................
Mr K. Mam
Candidate

# Acknowledgements

This thesis is dedicated to
My mother and father

# Abbreviations

**BF** - Bright Field

**BS** – Backscattered Electron

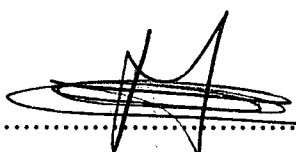**CBD** – Chemical Bath Deposition

**CDF** - Centred Dark Field

**CTEM** - Conventional TEM

**DF** - Dark Field

**GIXRD** – Glazing Incident X-ray diffraction

**HCP** – Hexagonal Close-Packed

**ITO** – Indium Tin Oxide

**MBE** – Molecular Beam Epitaxy

**MOVPD** – Metal Organic Vapour Phase Deposition

**MOVPE** – Metal Organic Vapour Phase Epitaxy

**PMT** – Photo-multiplier Tube

**PL** – Photoluminescence

**SAD** - Selected Area Diffraction

**SE** – Secondary Electron

**SEM** – Scanning Electron Microscopy

**STEM** – Scanning Transmission Electron Microscopy

**STEM-CL** – Cathodoluminescence Measurment in STEM

**TCO** – Transparent Conducting Oxide

**(S)TEM-CL** – STEM-CL or TEM-CL

**TEM** – Transmission Electron Microscopy

**TEM-CL** – Cathodoluminescence Measurement in TEM

# Contents

# Chapter 1

# Introduction

## 1.1 Introduction

Cadmium sulphide (CdS), is an important II/VI compound semiconductor material. It is used extensively in photosensors, transducers, optical detectors, and other devices. In the last five decades, CdS has been one of the most investigated thin film semiconductors for photovoltaics. CdS first got attention as a hetero-junction partner in the 1950's demonstrating 6% efficiency for the first all thin film $Cu_xS/CdS$ junction [1]. Today CdS is considered as the best-suited window material for both CdTe and $CuIn(Ga)Se_2$ solar cells [1-3]. The most important parameter for transparent thin films used for optical window applications is the bandgap energy. CdS polycrystalline films possess a direct band gap of 2.42–2.45 eV at room temperature. Since heterojunctions based on CdS thin layers are very promising structure for solar cells, a comprehensive optical and structural characterisation is required of CdS grown in technologically important conditions. For solar energy applications, CdS films are required to have, high optical transparency and low electrical resistivity.

The purpose of this work was to investigate the optical and structural properties of single crystal and polycrystalline thin films CdS: Properties of the polycrystalline thin film can differ from those of single crystals.

Single crystal CdS was mainly used for a study of the CdS with the unusual technique of combined transmission electron microscopy and cathodoluminescence (TEM-CL). TEM is a well known technique for the study of structure and defects in semiconductors whereas CL is a characterisation tool based on the emission of light as a result of electron bombardment. In semiconductors this emission is a result of radiative recombination of electrons and holes generated by incident electrons. The energy of an emitted photon yields information about the energy states participating in the recombination. Hence a CL spectrum contains information concerning the fundamental band-gap, donor and acceptor levels, and excitonic structure. The advantage of a TEM-CL system is the ability to correlate the spectroscopic CL information with structural information from TEM at very high spatial resolution.

Thin film CdS used as a window layer in CdTe-based solar cells, may be grown by many different techniques. In this work, the films investigated were grown by: i) chemical bath deposition (CBD), and ii) metal organic chemical vapour deposition (MOCVD). Clearly the development of CdS-based solar cell devices has been extremely successful. At present, high efficiencies of 16.5% and 16.0 % have been measured for CBD and MOCVD-grown CdS respectively [4, 5]. Despite this a number of materials issues remain [6]. The difficulty in obtaining large grain size, high-quality films with good optoelectronic properties for device applications is a major concern in most of the low-cost thin-film deposition techniques. It is essential to increase the grain size of CdS because the quality of sequentially deposited CdTe critically depends on the quality of CdS substrate. The enhancement of CdS properties has been in progress for some time now and the efforts to deposit large-grain CdS films on low cost substrates are still ongoing.

In the first section of this work the principal properties of thin film cadmium sulphide are described in Chapter 2. A description of experimental techniques is given in Chapter 3, followed by the experimental results which are divided into three chapters as follows:

- Chapter 4 is divided in two parts. The first describes a simple model of the spatial resolution of STEM-CL image. In the second part some limitations of CL acquisition are discussed.

- In Chapter 5, the features observed in TEM-CL and PL spectra of single crystal of CdS are identified and the effects of electron beam degradation are investigated. STEM-CL image of dislocation is correlated with TEM imaging to investigate the effect of dislocation on CL emission.

- Following this, in Chapter 6, some optical and structural properties of thin film CdS grown by CBD and MOCVD techniques are described. In particular the grain size distributions, crystalline phase and optical transmission of the layers were investigated in detail. The action of annealing and $CdCl_2$ treatment for CBD grown films and the influence of the growth conditions for MOCVD were studied.

Overall discussion and conclusions are given in Chapter 7. Computer code is given in Appendices A.

# 1.2 References

1.    R. H. Bube, *Photovoltaic materials / Richard H. Bube.* (1998) Imperial College Press

2.    T. L. Chu and S. S. Chu, *Thin film II-VI photovoltaics,* Solid-State Electronics **38** (1995) 533-549

3.    D. Bonnet, *The CdTe thin film solar cell - an overview,* Int. J. Solar Energy **12** (1992) 1-14

4.    T. Aramoto and H. H. Seiji Kumazawa, Takashi Arita, Satoshi Shibutani, Tuyoshi Nishio, Junji Nakajima, Miwa Tsuji, Akira Hanafusa, Takeshi Hibino, Kuniyoshi Omura, Hideaki Ohyama, and Mikio Murozono, *16.0% Efficient Thin-Film CdS/CdTe Solar Cells,* Japanese Journal of Applied Physics, Part 1 **36** (1997) pp. 6304-6305

5.    X. Wu, J. C. Keane, R. G. Dhere, C. DeHart, D. S. Albin, A. Duda, T. A. Gessert, S. Asher, D. H. Levi, and P. Sheldom, *16.5 % Efficient CdS/CdTe ploycrystalline thin-film solar cell,* 17th European Photovoltaic Solar Energy Conference, Munich, Germany, (2001)

6.    K. Durose, P. R. Edwards, and D. P. Halliday, *Materials aspects of CdTe/CdS solar cells,* Journal of Crystal Growth **197** (1999) 733-742

Chapter 2

# General Properties of Cadmium Sulphide

## 2.1 Structural Properties

The properties of CdS films can be quite different from bulk material, reflecting their preparation history. The most common phase of CdS bulk crystal is the hexagonal (wurtzite) structure, whereas the cubic (zincblende) phase of CdS is metastable, appearing in low-dimensional structures such as thin films or nanocrystalline systems [1]. Despite a large number of studies that have been devoted to CdS thin films, questions remain about the internal structure of the films. For instance, the attribution of the X-ray or electron diffraction patterns to the hexagonal or the cubic form of CdS is controversial, with hexagonal, cubic, or mixed structures, being reported as a function of the preparation conditions [2, 3]. CdS is known to present polymorphism, but, as compared with vapour phase deposition, it seems that this phenomenon is favoured by growth in solutions. Polytypic material can be described as a sort of intermediate between face-centred cubic and hexagonal structures. To be more specific, the stacking sequence of close packed planes in a hexagonal structure is ab-ab-ab-... while that of fcc materials is abc-abc-abc-... In polytypic material neither stacking sequence dominates, and either a random sequence or more complicated repetitive sequence is found [4].

Presently the processes for obtaining the cubic phase for CdS as well as the evolution from one phase to the other are not fully controlled. The formation of the cubic or hexagonal phase depends on many factors including the deposition technique. In CBD, the structure of the film is influenced by the composition of the bath, temperature and pH of the solution. For example, Oliva et al. [5, 6] have reported the cubic zincblende phase when the CdS film was prepared from a bath containing cadmium chloride, potassium hydroxide, ammonium nitrate and thiourea at a temperature of 75°C. On the other hand Rakhshani et al. [7] have reported that hexagonal (wurtzite) phase films were prepared from a chemical bath containing cadmium nitrate, sodium citrate, aqueous ammonia and thiourea, the temperature of the bath was 60°C. There are reports of both cubic and hexagonal phases for the CdS films prepared by CBD [8-10]. As regards transformation, the cubic-hexagonal transition is favoured by thermal annealing [11]. For instance, in CdS films that are CBD deposited onto silicon substrates, the cubic-hexagonal phase transition was promoted by a 400°C anneal for 0.5 hour in air [11]. In other work, the CdS cubic-hexagonal phase transition is reported to occur at annealing temperatures of 300-400°C [12, 13].

## 2.2 Optical Properties

The band gap energy of thin films is one of the most important parameters of solar cell window layers. CdS polycrystalline films possess a direct band gap of 2.42–2.45 eV at room temperature. High optical transparency is one of the first requirements for solar cell applications. It depends on the band gap energy value and the thickness measured on the films, and shows a strong dependence on the film preparation procedure. The optical properties related to the deposition techniques are discussed by several authors [5, 14, 15]. In spite of this, the optical properties of both structures (cubic and hexagonal) are broadly similar [13, 16].

For instance in CBD-grown CdS, it has been shown that the higher the temperature at which the samples were prepared, the lower their bandgap energy [17]. Also, samples subjected to annealing treatments present lower bandgap energy than those in the same as-grown conditions [17]. This trend should be correlated to the structural properties of the samples to find the origin of the bandgap shifting. It can be due to film thickness [14], grain size [18, 19] or even the presence of different phases [12, 20]. Although the difference of bandgap in the two phases is only 30 meV (2.48 eV for hexagonal and 2.45 eV) [21], the phase changes therefore are unlikely to account for all of the bandgap changes observed. Other parameters affecting the bandgap are strain, non-stochiometric films, and defects.

## 2.3 CdS Growth

A large variety of deposition techniques have been utilised to obtain solar cell quality layers of CdS. These preparation techniques include: sputtering [22], vacuum evaporation [23], spray pyrolysis [24], electrodeposition [25] and chemical bath deposition (CBD) [3, 9, 12, 14, 26, 27]. Among these various techniques, CBD, has proven to be the most suitable method to produce CdS films for photovoltaic applications, because this technique offers the advantages of a conformal coverage on rough surfaces at minimal thicknesses, both easily and at a low cost [28-30]. This method also ensures no pinholes, which is very important for solar cell devices. Since CBD is in most widespread use, the technique is briefly discussed:

CBD is a wet chemical method based on the slow, controlled decomposition of thiourea in alkaline solution and the presence of $Cd^{2+}$ ions. Kaur's original work used cadmium acetate and the reaction proceeds in aqueous solution as follows [31]:

$$Cd(CH_3COO)_2 + (NH_2)_2C=S + 2OH^- \rightarrow CdS(s) + H_2CN_2 + 2H_2O + 2CH_3COO^-.$$
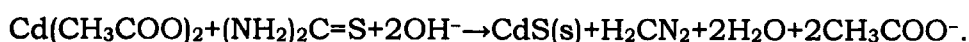
The reaction proceeds heterogeneously on an immersed substrate at 90°C. There are many variations of the bath chemistry and treatment concentrations which influence the purity and physical form of the deposit. This deposition technique is explained in section 3.3.2.

# 2.4 CdCl$_2$ Treatment of CdS

Even though resistivity and optical transmittance depend strongly on the preparation conditions, pure (undoped) as-grown CdS films generally show high resistivity. Thus it is difficult to produce undoped films with the required electro-optical properties just by controlling the preparation conditions. An effective way to obtain CdS films with the desired parameters is to introduce dopants, and there have been many reports on this [32-35], using Cu and Bi for example. Ion implantation is potentially attractive as an alternative doping technique but too costly for solar cell devices. Reports are available on ion implantation studies on CdS films prepared by different methods [36, 37]. Since defect formation is associated with ion implantation, lattice disorder will be produced and consequently the optical and electrical properties will be changed. Parikh et al. [38] have studied the effects of lattice disorder on CdS films produced in single crystals on implantation with different types of ions using Raman backscattering/channelling and transmission electron microscopy. During ion implantation in semiconductors, it is possible to expect three types of changes: (i) the electrical properties of the material - due to the introduction of implanted species, (ii) lattice disorder (structural re-arrangement), and (iii) bandgap and optical transparency (electronic structure).

There is a growing literature on the intermediate use of CdCl$_2$ on CdS to recrystallise it and enhance the n-conductivity. Within the CdS films, CdCl$_2$ leads to grain size enhancement and a simultaneous decrease in the number of high-resistance paths in the CdS films. Romeo et al. [39] reported on CdS treated directly with evaporated CdCl$_2$ and observed a grain size increase. The proposed reason for this change is the CdCl$_2$-

assisted coalescing of smaller grains in the CdS films. Such treatments probably have their origin in the processing of CdS photoconductors and were also used extensively in the sintering of screen printed CdS for solar cells. For example Lee et al. [40] reported that sintering of CdS with 9% $CdCl_2$ effected sintering at 700°C but $CdCl_2$ segregated at the grain boundaries.

# 2.5 Use of CdS in Solar Cell Devices

Cadmium sulphide, CdS, is known to be an excellent heterojunction partner of p-type cadmium telluride, "CdTe", or p-type copper indium diselenide, "$CuInSe_2$". Very thin CdS films are commonly used as window layers in high-efficiency thin film solar cells based on CdTe or $CuInSe_2$ [29, 30]. The minimum thickness should allow a CdS conformal coverage of the substrate without the formation of defects (e.g. pinholes) that could shunt the cell.

## 2.5.1 CdTe/CdS Thin Film Technologies

The cadmium telluride (CdTe) based thin film solar cell is one of the most promising candidates for terrestrial application. CdTe is typically used in conjunction with cadmium sulphide (CdS) for the formation of p-n heterojunctions. Its bandgap of 1.5 eV is well suited to terrestrial application, its direct gap results in a high absorption over the whole solar spectra. The initial CdTe/CdS thin film device is attributed to Bonnet et al. [41], who fabricated 5 % cells by evaporating CdS on a CdTe film. Yamuchi et al. [42] reported the production of CdTe-based cells with efficiencies over 10 %, which made possible the commercialisation of these with modules around 6 % efficiency. The technological advances of the close-space vapour transport deposition technique lead to the fabrication of a 15.8 % cell onto a borosilicate glass substrate, which was reported by Ferekides et al. [43]. A 16.5 % efficient CdTe/CdS ploycrystalline thin-film solar cell has

been produced by Wu et al. [44]. Recently, Cunnungham et al. [45], et al. reported a CdTe/CdS solar cell with an area of 0.55 m², and 10.5 % efficiency. The status and prospects for CdTe-based photovoltaics are also reviewed by several authors [43, 46-48].

## 2.5.2 CdS in CIGS Thin Film Technologies

In the early of the thin film Cu(In,Ga)Se₂ solar cell, evaporated CdS thin films were used to create a heterojunction with CIGS [49]. Due to a low conductivity and relatively small bandgap (2.45 eV) of the CdS films, the cell had a low fill factor FF and low quantum response in the blue light region of the solar spectrum. In order to improve these quantities, from the mid to late 1980s, the thickness of the evaporated CdS was reduced and a ZnO window layer with a better conductivity and a wider bandgap (3.3 eV) was deposited onto it [50]. A further optimisation consisted in replacing the evaporated CdS by a film deposited from chemical bath solutions [51]. Today the best CIGS solar cell performances [52, 53] are obtained by using a 50 nm thick deposited (CBD) CdS in conjunction with the ZnO. The recipe and the deposition method of the CBD-CdS buffer have been developed since the work of Kessler et al. [54]. The key aspects of CIS-based photovoltaics are also reviewed by several authors [46, 55].

# 2.6 References

1. R. J. Bandaranayake, G. W. Wen, J. Y. Lin, H. X. Jiang, and C. M. Sorensen, *Structural phase behavior in II–VI semiconductor nanoparticles*, Applied Physics Letters **67** (1995) 831-833

2. J. M. Dona and J. Herrero, *Chemical Bath Deposition of CdS Thin Films: An Approach to the Chemical Mechanism Through Study of the Film Microstructure*, Journal of The Electrochemical Society **144** (1997) 4081-4091

3. D. Lincot and R. Ortega-Borges, *Mechanism of Chemical Bath Deposition of Cadmium Sulphide Thin Films in the Ammonia-Thiourea System. In Situ Kinetic Study and Modelization.*, Journal of The Electrochemical Society **140** (1993) 3464

4. D. Lincot, B. Mokili, M. Froment, R. Cortès, M.-C. Bernard, C. Witz, and J. Lafait, *Phase Transition and Related Phenomena in Chemically Deposited Polycrystalline Cadmium Sulphide Thin Films*, J. Phys. Chem. B **101** (1997) 2174-2181

5. A. I. Oliva, O. Solis-Canto, R. Castro-Rodriguez, and P. Quintana, *Formation of the band gap energy on CdS thin films growth by two different techniques*, Thin Solid Films **391** (2001) 28-35

6. R. Castro-Rodriguez, A. I. Oliva, V. Sosa, F. Caballero-Briones, and J. L. Pena, *Effect of indium tin oxide substrate roughness on the morphology, structural and optical properties of CdS thin films*, Applied Surface Science **161** (2000) 340-346

7. A. E. Rakhshani and A. S. Al-Azab, *Characterization of CdS films prepared by chemical-bath deposition*, J. Phys. Condens. Matter **12** (2000) 8745-8755

8. S. A. Al Kuhaimi, *Influence of preparation technique on the structural, optical and electrical properties of polycrystalline CdS films*, Vacuum **51** (1998) 349-355

9. N. Lejmi and O. Savadogo, *The effect of heteropolyacids and isopolyacids on the properties of chemically bath deposited CdS thin films*, Solar Energy Materials and Solar Cells **70** (2001) 71-83

10. P. J. Sebastian and H. Hu, *Identification of the impurity phase in chemically deposited CdS thin films*, Advanced Materials for Optics and Electronics **4** (1994) 407-412

11. D. Lincot, M. Froment, and H. Cachet, *Advances in Electrochemical Science and Engineering Vol. 6, Wiley-VCH, Weinheim In: R.C. Alkire and D.M. Kolb, Editors, Advances in Electrochemical Science and Engineering Vol. 6, Wiley-VCH, Weinheim (1999), pp. 165–235.*

12. O. Zelaya-Angel and R. Lozada-Morales, *Sphalerite-wurtzite phase transformation in CdS*, Physical Review B (Condensed Matter) **62** (2000) 13064-13069

13. P. Hofmann, K. Horn, A. M. Bradshaw, R. L. Johnson, D. Fuchs, and M. Cardona, *Dielectric function of cubic and hexagonal CdS in the vacuum ultraviolet region*, Physical Review B (Condensed Matter) **47** (1993) 1639-1642

14.  J. P. Enriquez and X. Mathew, *Influence of the thickness on structural, optical and electrical properties of chemical bath deposited CdS thin films,* Solar Energy Materials and Solar Cells **76** (2003) 313-322

15.  S. A. A. Kuhaimi, *Influence of preparation technique on the structural, optical and electrical properties of polycrystalline CdS films,* Vacuum **51** (1998) 349-355

16.  M. Cardona, M. Weinstein, and G. A. Wolff, *Ultraviolet Reflection Spectrum of Cubic CdS,* Phys. Rev. **140** (1965) A633–A637

17.  A. Cortes, H. Gomez, R. E. Marotti, G. Riveros, and E. A. Dalchiele, *Grain size dependence of the bandgap in chemical bath deposited CdS thin films,* Solar Energy Materials and Solar Cells **82** (2004) 21-34

18.  R. J. Bandaranayake, G. W. Wen, J. Y. Lin, H. X. Jiang, and C. M. Sorensen, *Structural phase behavior in II-VI semiconductor nanoparticles,* Applied Physics Letters **67** (1995) 831-833

19.  M. Ichimura, F. Goto, and E. Arai, *Structural and optical characterization of CdS films grown by photochemical deposition,* Journal of Applied Physics **85** (1999) 7411-7417

20.  O. Zelaya-Angel, J. J. Alvarado-Gil, R. Lozada-Morales, and H. Vargas, *Band-gap shift in CdS semiconductor by photoacoustic spectroscopy: Evidence of a cubic to hexagonal lattice transition,* Applied Physics Letters **64** (1994) 291-293

21.  J. G. Mendoza-Alvarez, J. Gonzalez-Hernandez, F. Sanchez-Sinencio, O. Zelaya, and S. S. Chao, *Luminescence and particle size in microcrystalline CdTe thin films,* Journal of Crystal Growth **86** (1990) 391-395

22.  F. El Akkad and M. A. Naby, *Properties of RF-sputtered CdS thin films,* Solar Energy Materials **18** (1989) 151-158

23.  A. Chemseddine and M. L. Fearheiley, *Improved CdS buffer/window layers for thin film solar cells,* Thin Solid Films **247** (1994) 3-7

24.  S. Martinuzzi, *Trends and problems in CdS/Cu$_x$S thin film solar cells: a review,* Solar Cells **5** (1982) 243-268

25.  A. S. Baranski, M. S. Bennett, and W. R. Fawcett, *The physical properties of CdS thin films electrodeposited from aqueous diethylene glycol solutions,* Journal of Applied Physics **54** (1983) 6390-6394

26.  J. Herrero, M. T. Gutierrez, C. Guillen, J. M. Dona, M. A. Martinez, A. M. Chaparro, and R. Bayon, *Photovoltaic windows by chemical bath deposition,* Thin Solid Films **361-362** (2000) 28-33

27.  C. Guillen, M. A. Martinez, C. Maffiote, and J. Herrero, *Chemistry of CdS/CuInSe$_2$ structures as controlled by CdS deposition bath,* J. Electrochem. Soc. **148** (2001) G602-606

28.  H. Moutinho, R. G. Dhere, K. Ramanathan, P. Sheldon, and L. Kazmerski, *Growth analysis of cadmium sulphide thin films by atomic force microscopy,* IEEE (1996) 945-948

29.  B. Dimmler, E. Gross, R. Menner, M. Powalla, D. Hariskos, M. Ruckh, U. Rühle, and H. W. Schock, *Thin film solar modules based on CIS prepared by the co-evaporation method,* IEEE (1996) 757-762

30.  A. Catalano, *Polycrystalline thin-film technologies: Status and prospects,* Solar Energy Materials and Solar Cells **41-42** (1996) 205-217

31. I. Kaur, D. K. Pandya, and K. L. Chopra, *Growth kinetics and ploymorphism of chemically deposited CdS films*, J. Electrochem. Soc. **127** (1980) 943-948

32. Y. Gunal and H. Mamikoglu, *On the temperature dependence of the intergrain barriers in polycrystalline CdS thin films*, Thin Solid Films **185** (1990) 1-7

33. Y. Kashiwaba, I. Kanno, and T. Ikeda, *p-Type Characteristics of Cu-Doped CdS Thin Films*, Jpn. J. Appl. Phys. **31** (1992) 1170-1175

34. P. J. Sebastian, *p-type CdS thin films formed by in situ Cu doping in the chemical bath*, Applied Physics Letters **62** (1993) 2956-2958

35. H. Chavez, M. Jordan, J. C. McClure, G. Lush, and V. P. Singh, *Physical and electrical characterization of CdS films deposited by vacuum evaporation, solution growth and spray pyrolysis*, Journal of Materials Science: Materials in Electronics **8** (1997) 151-154

36. B. Tell and W. M. Gibson, *Properties of ion-implanted Bi in CdS*, J. Appl. Phys. **40** (1969)

37. K. L. Narayanan, K. P. Vijayakumar, K. G. M. Nair, and R. Kesavamoorthy, *Raman scattering studies of Ar+ implanted CdS films prepared by vacuum evaporation*, Phys. Status Solidi A **164** (1997) 725-732

38. N. R. Parikh, D. A. Thompson, and G. J. C. Carpenter, *Ion implantation damage in CdS*, Radiation Effects **98** (1986) 289-300

39. A. Romeo, D. L. Batzner, H. Zogg, C. Vignali, and A. N. Tiwari, *Influence of CdS growth process on structural and photovoltaic properties of CdTe/CdS solar cells*, Solar Energy Materials and Solar Cells **67** (2001) 311-321

40. J. S. Lee and H. B. Im, *Effects of junction formation conditions on the photovoltaic properties of sintered CdS/CdTe solar cells*, Journal of Materials Science **21** (1986) 980-984

41. D. Bonnet and H. Rabenhorst, *New results on the development of a thin-film p-CdTe-n-CdS heterojunction solar cell*, IEEE (1972) 129-132

42. K. Yamaguchi, H. Matsumoto, N. Nakayama, and S. Ikegami, *Photovoltaic Effect in CdTe-CdS Junctions Prepared by Vapor Phase Epitaxy*, Jpn. J. Appl. Phys. **15** (1976) 1575-1576

43. C. S. Ferekides, U. Balasubramanian, R. Mamazza, V. Viswanathan, H. Zhao, and D. L. Morel, *CdTe thin film solar cells: device and technology issues*, Solar Energy **77** (2004) 823-830

44. X. Wu, J. C. Keane, R. G. Dhere, C. DeHart, D. S. Albin, A. Duda, T. A. Gessert, S. Asher, D. H. Levi, and P. Sheldom, *16.5 % Efficient CdS/CdTe ploycrystalline thin-film solar cell*, 17th European Photovoltaic Solar Energy Conference, Munich, Germany, (2001)

45. D. Cunnungham, K. Davies, L. Grammond, E. Mopas, N. O'Connor, M. Rubcich, M. Sadeghi, D. Skinner, and T. Trumbly, *Large area Apollo module performance and reliability*, Conference Record, 28th IEEE Photovoltaic Specialists Conference, Alaska (2000) 13-18

46. R. W. Birkmire and E. Eser, *Polycrystalline thin film solar cells: present status and future potential*, Annu. Rev. Mater. Sci. **27** (1997) 625-653

47. K. Durose, D. Boyle, A. Abken, C. J. Ottley, P. Nollet, S. Degrave, M. Burgelman, R. Wendt, J. Beier, and D. Bonnet, *Key aspects of CdTe/CdS solar cells*, Phys. Stat. Sol. B **229** (2002) 1055-1064

48. K. Durose, P. R. Edwards, and D. P. Halliday, *Materials aspects of CdTe/CdS solar cells,* Journal of Crystal Growth **197** (1999) 733-742

49. L. L. Kazmerski, Inst. Phys. Conf. Ser. **35** (1997) 217

50. R. R. Potter, C. Eberpacher, and L. B. Fabick, *Device analysis of CuInSe2/(Cd,Zn)S/ZnO solar cells,* IEEE (1985) 1659-1064

51. D. Lincot, M. Froment, and H. Cachet, *Advances in Electrochemical Science and Engineering Vol. 6, Wiley-VCH, Weinheim pp. 165–235.,* ed. R.C.A.a.D.M. Kolb (1999)

52. M. A. Contreras, B. Egaas, K. Ramanathan, J. Hiltner, A. Swartzlander, F. S. Hasoon, and R. Noufi, *Progress towards 20% efficiency in Cu(In,Ga)Se polycrystalline thin-film solar cell,* Progress in Photovoltaics: Research and Applications **7** (1999)

53. M. A. Contreras, M. J. Romero, B. To, F. Hasoon, R. Noufi, S. Ward, and K. Ramanathan, *Optimization of CBD CdS process in high-efficiency Cu(In,Ga)Se2-based solar cells,* Thin Solid Films **403-404** (2002) 204-211

54. J. Kessler, M. Ruckh, D. Hariskos, U. Ruhle, R. Menner, and H. W. Schock, *Interface engineering between CuInSe2 and ZnO,* IEEE (1993) 447-452

55. R. R. Gay, *Status and prospects for CIS-based photovoltaics,* Solar Energy Materials and Solar Cells **47** (1997) 19-26

# Chapter 3

# Experimental Techniques

## 3.1 Introduction

In this chapter the growth and characterisation techniques used in this work are described. The standard characterisation techniques of SEM and TEM used in this study are briefly outlined, whilst the experimental techniques specific to TEM-CL are discussed in greater detail. However, to begin with, the details of the growth techniques are outlined below.

## 3.2 Material Growth

In this work, single crystal and polycrystalline thin films of CdS were investigated. The Piper-Polich technique [1] was used to grow single crystal of CdS, whilst chemical bath deposition (CBD) and metal-organic chemical vapour deposition (MOCVD) were used to grow the CdS thin films.

## 3.2.1 The Piper-Polich Method

### 3.2.1.1    Principle

Most of the vapour techniques are in some sense a derivative of the Piper-Polich method. Although this was developed originally for the growth of CdS [1], the technique can be applied to the vapour growth of any compound which sublimes readily below the melting point temperature. The crystal is grown in a closed crucible that is moved through a steep temperature gradient such that the source material is always hotter than the growing surface and mass transport occurs from source to crystal, as shown in Figure 3.1. A feature of the original design was that growth could take place with a crucible either evacuated or with a slow flow of inert gas, such as argon [2]. The Piper-Polich method is used for growing doped single crystals of II–VI compounds a few $cm^3$ in size.
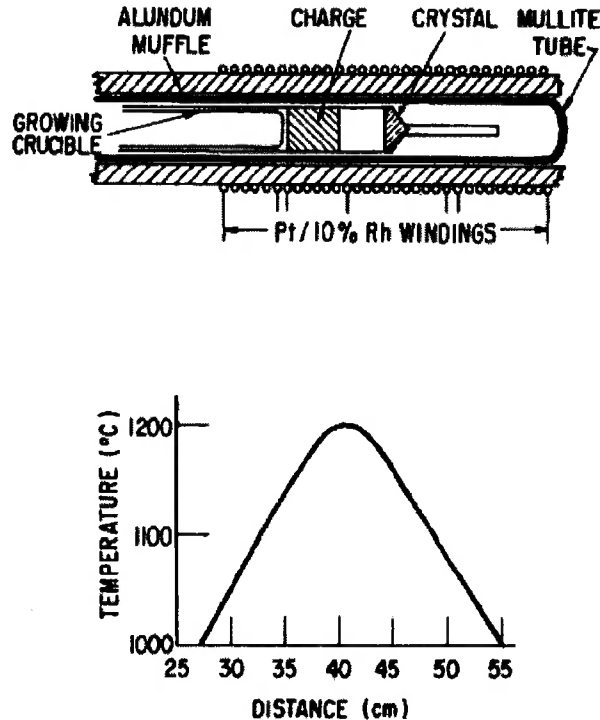


**Figure 3.1:    Furnace cross section and temperature profile used for growing CdS. The cross section is drawn to the same scale as the profile (reproduced from [1]).**

### 3.2.1.2    Growth Conditions of CdS Single Crystal

A CdS charge was sintered by packing CdS powder into a quartz tube open at two ends as shown in Figure 3.1. The charge was baked at 500°-700°C for approximately 1 hour, then fired in a stream of argon at 1 atm to purify the charge. The furnace temperature was increased to the operating temperature and the argon flow maintained throughout the run. The initial position of the crucible was such that the tip was near the point of maximum temperature. The crucible was mechanically pushed so that the tip moved into a cooler region at a constant velocity.

Some vapour escapes past the inner quartz tube and condenses and seals off the crucible thus confining the rest of the charge. An equilibrium vapour pressure of the compound being grown is then established. As the tube moves, the supersaturation at the tip increases until nucleation occurs. The growing surface temperature was approximately 30°C below the temperature of the charge. The diameter of the crystal was 15 mm. The CdS crystals grown had a yellow-green tint characteristic of their being grown under Cd-rich conditions.

## 3.2.2 Chemical Bath Deposition (CBD)

### 3.2.2.1    CBD Principle

The underlying principles of CBD form the basis of several reviews [3-6]. Typical CBD processes for metal chalcogenides involve controlled precipitation of material on a substrate, which is immersed into heated aqueous solutions. These solutions contain a metal salt, chalcogenide source and complexing agent for the metal. A diversity of metal salts can be used such as chlorides, nitrates, sulfates and acetates. The organic chalcogenide compound decomposes into ions in the solution. Sources of $S^{2-}$ ions include thioacetamide ($CH_3CSNH_2$), thiosulfate ($S_2O_3^{2-}$) or thiourea ($SC(NH_2)_2$) while those for $Se^{2-}$ ions are selenosulfate ($Se_2O_3^{2-}$) or selenourea ($SeC(NH_2)_2$). As a result of the aqueous reaction media, oxide and hydroxide materials may also be formed. The metal complexing agent controls the

hydrolysis of the metal ion. Basic amine ligands such as ammonia ($NH_3$), triethanolamine ($N(CH_2CH2OH)_3$) or ethylenediamine ($H_2N(CH_2)_2NH_2$), although citrate ($[HOC(COO)(CH_2COO)_2]^{3-}$) and cyanide ($CN^-$) are also employed as complexing agents [7].

In a CBD reaction, solid material is formed from baths that are supersaturated with respect to the particular solid phase. The two types of reactions that lead to formation of a solid phase are a) homogenous precipitation, within the bulk of the solution and b) heterogeneous precipitation, which occurs at an existing surface such as the substrate. The second process leads directly to film formation.

In general the CBD processes can be divided into several steps. i) The equilibrium between the complexing agent and water is obtained, ii) The ionic metal–ligand complexes are either formed or dissociated, iii) Chalcogenide source thermally decomposes, then iv) a solid phase is formed. Control over film growth process resides in the last three steps. If the four key steps of CBD process are considered, CdS desposition using a cadmium salt, aqueous ammonia and thiourea can be written as follows [7]:

1/ $NH_3$-$H_2O$ equilibrium:

$2NH_3+2H_2O \Leftrightarrow 2NH_4+ 2OH-$          Eq. 3.1

2/ Dissociation of the complex:

$Cd(NH_3)_4{}^{2+} \Leftrightarrow Cd^{2+} + 4NH_3$ (aq)          Eq. 3.2

3/ Hydrolysis of thiourea:

$S=C(NH_2)_2 + 2OH^- \rightarrow S^{2-}$ (aq) $+ H_2NC\equiv N + 2H_2O$      Eq. 3.3

4/ Formation of CdS:

$Cd^{2+}$ (aq) $+ S^{2-}$ (aq) $\rightarrow CdS$ (s)          Eq. 3.4

5/ Net reaction:

$Cd(NH_3)_4 + S=C(NH_2)_2 \rightarrow CdS$ (s) $+ H_2NC\equiv N + 2 NH_4+ + 2 NH_3$ (aq)     Eq. 3.5
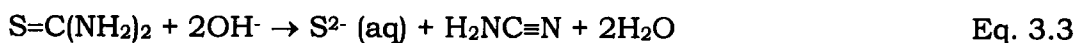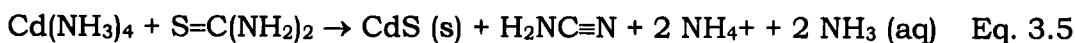
### 3.2.2.2    Growth Conditions for CdS grown by CBD

Samples were grown at the Department of Physics, University of Durham using a modified chemical bath deposition developed by Martin Archbold [8]. The substrate was a soda-lime glass substrate coated with a 100nm layer of indium tin oxide (ITO 20$\Omega$/$\square$ sheet resistance). The modified CBD technique differs from the commonly used method in two ways: firstly, ethylenediamine (EN) is used rather than ammonia as a complexing agent, and secondly the substrate rather than the reaction bath is heated. The advantages of EN are environmental and ease of employment. Figure 3.2 shows the actual CBD-kit. A temperature controlled circulating system was used to pump heated water through a cavity in a flat quartz glass plate; the substrate was held firmly to this plate to ensure a constant temperature over the surface. The chemical bath was a magnetically stirred aqueous solution of cadmium chloride ($CdCl_2$, 0.001 mol.dm$^{-3}$), EN ($NH_2CH_2CH_2NH_2$, 0.012 mol.dm$^{-3}$), sodium hydroxide (NaOH, 0.01 mol.dm$^{-3}$) and thiourea ($CS(NH_2)_2$, 0.01 mol.dm$^{-3}$). Solution pH of 12 was employed and the substrate temperature was held at a constant 65°C for deposition times of 90 minutes.

Three kinds of samples were produced: (A) as grown CdS, (B) films annealed in air at 400°C for 1 hour and (C) films with 150nm layer of evaporated $CdCl_2$ then annealed in air at 400°C for 1 hour. After annealing, C-type films were washed in methanol to remove any $CdCl_2$ residue left on this surface.
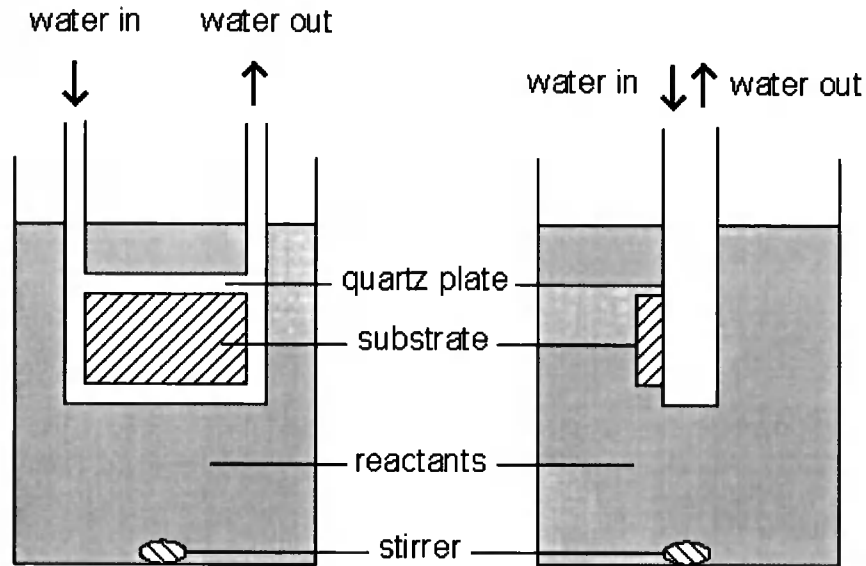
**Figure 3.2:** **Front and side view of the heated CBD holder apparatus**

## 3.2.3 Metal-Organic Chemical Vapour Deposition (MOCVD)

### 3.2.3.1 MOCVD Principle

Chemical vapour deposition of elements is a well-established technique for the growth of epitaxial or polycrystalline materials. Metal-organic vapour phase epitaxy (MOVPE) is defined as the growth on the surface of a crystal so that the layer grown has the same structure as the underlying substrate. CVD using metal-organic sources (MOCVD) is a cost efficient method for producing polycrystalline thin films. Its main advantages are the following:

- It can produce a wide range of thickness,
- Doping concentration and distribution in the films can be controlled,
- Multilayers can be obtained in a single deposition,

CVD is a technique operating at low temperature typically between 200° and 1600°C, from organic precursors in hydrogen carrier gas. The substrate supported on a graphite succeptor are heated radiatively or by coupling a RF generator. A typical growth rate for CdS is ~5 nm/min. The

**20**

CVD involves a series of gas phases and surfaces reactions [9]. The choice of organometallics has been a major issue in the development of CVD, to fulfil in lower decomposition temperature and higher purity. Low growth temperatures are desirable since they reduce solid-state inter-diffusion process, sharpening the interface, and decreasing the possibility of unwanted doping. Dimethylcadmium (DMCd) which decomposes at 150°C and ditertiarybutylsulphide which decomposes at 290°C were chosen to produce cadmium and sulphur respectively. The choice of growth conditions is an important part of the overall design. Independent parameters such as substrate temperature, II/VI ratio and total flow rate must be carefully chosen to give the desired material properties.

## 3.2.3.2    Growth Conditions for CdS grown by MOCVD

The CdS layers were grown by MOCVD at the University of Wales, Bangor. CdS thin films were grown onto ITO/glass substrate. The substrate was supplied by Merck Display Technology (MDT) and constituted of 0.7mm soda lime glass coated with a bilayer of $SiO_2$ (~20nm) and ITO (~100nm). The $SiO_2$ stops the diffusion of impurities from the glass, while the indium doped tin oxide provides the high conductivity required to provide a low sheet resistance. For the growth of MOCVD-CdS, the precursor vapours used were dimethylcadmium (DMCd) and ditertiarybutylsulphide (DTBS), which were provided by Epichem Ltd. The layers were deposited at atmospheric pressure in a Thomas Swan reactor with a graphite substrate holder. The holder was heated by a graphite resistance element, for which the maximum temperature achievable was 600°C. A gas concentration analyser Epison (Thomas Swan Ltd) was used to calibrate the concentration of organometallic by measuring sonic velocity in binary mixture. Film thickness was measured by laser reflectometry that measures the thin film interference between the growing film and the interface [10]. Details of the experimental procedure for the MOCVD growth of CdS have been also given elsewhere [11]. Figure 3.3 shows the actual design of the horizontal reactor used for MOCVD.

In this study, 150 nm thick CdS layers were deposited at 290°C, 300°C and 330°C at a growth rate of ~5 nm/min, for two different precursor ratios (II/VI) of 0.78 and 1.0. The growth rate of CdS varies a lot over this temperature range.
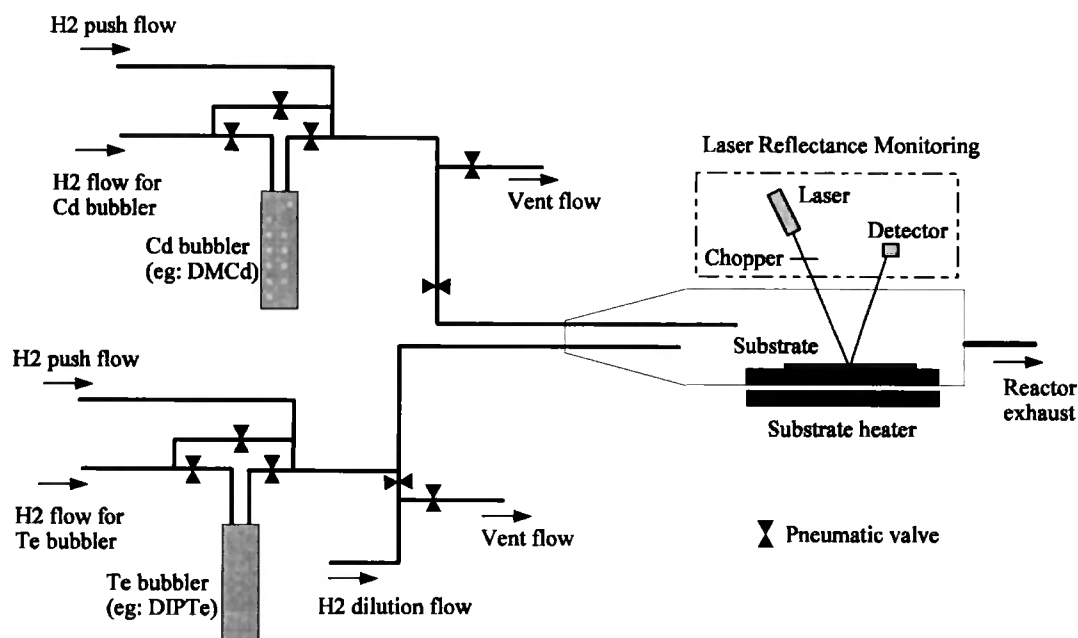


**Figure 3.3:** **Horizontal reactor with gas supply for MOCVD growth. The actual system contains six bubblers for Te, Cd, S, As, Cl and Zn organometallics.**

# 3.3 Specimen preparation for TEM foils

In this work, two techniques were used to prepare TEM foils, both of which involved some mechanical polishing. In the first technique applied to bulk CdS mechanical polishing was followed by ion beam milling to perforation, in the second method applied to thin film CdS grown by MOCVD and CBD, hydrofluoric acid (HF) was used to dissolve the glass substrate. Specimen preparation for TEM foils is reviewed by a number of authors [12-15]. The techniques used here are outlined in detail below.

## 3.3.1 Bulk CdS

Slices of single crystal CdS were mechanically polished from both sides using a Logitech PM2 with 17µm SiC powder to a thickness of ~1mm. 3.05mm discs from the 1mm thick slices were cut with a Testbourne Model 360 micro-drill with SiC and water to assist the drilling. The discs were then mounted onto the sample stub of the Gatan disc grinder. The emergent face was then polished with Buehler Metadi Supreme diamond suspension of decreasing roughness (15, 6 and 1 µm) and appropriate Struers polishing cloths. Figure 3.4 shows the actual arrangement. The main advantage of Gatan disc grinder is that the pressure applied on the sample is constant. By changing the screw thread position the amount of material to be polished can be varied. While the Gatan grinder may be used by hand on a polishing cloth, it was convenient to use it with a lapping machine. To make this practical, the polisher was tethered to a post. During active polishing edge friction pulls the grinder to a perimeter of rotating pad. The point at which the protruding part of the sample is polished off is indicated by the grinder moving to the centre of the pad. The Gatan disc moves inwards towards the centre of the pad, when the sample level corresponds to the bottom surface of the Gatan discs. It was ensured that all compounds were completely cleaned when changes of diamond suspension grade occurred.
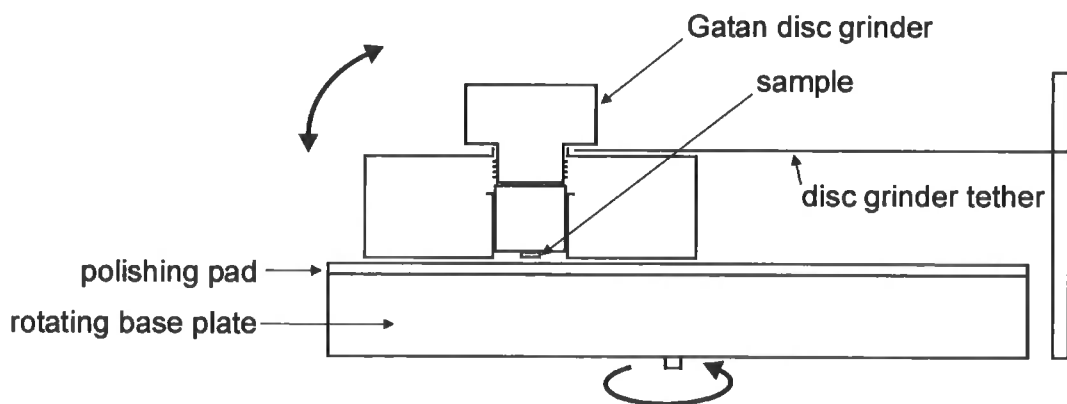


**Figure 3.4:** **Arrangement for the mounting of a Gatan disc grinder on a Logitech PM2 mechanical polisher.**

Once the polishing to 1 µm was finished on the exposed side, the sample was cleaned with isopropyl alcohol. A gold support ring was glued to the disc using room temperature setting epoxy. The sample was remounted on the Gatan grinder stub with the support ring facing the metal stub. It was then polished until its thickness was <50µm, by reducing the diamond suspension roughness from 15 µm to 1 µm. The sample was then removed and cleaned with trichloroethane.

Finally, the sample was thinned from both sides simultaneously using an Ion Tech 800 Series Ar⁺ miller at 4kV. It was cooled with a flow of liquid nitrogen and rotated during thinning to prevent contamination and surface damage. The rotation was performed by a PC controlled RS 4-Phase Unipolar Stepper Drive board 332-098. Initial thinning was started at 20-30° and reduced to 5° as perforation approached. Figure 3.5 shows the schematic diagram of an ion-beam thinning.
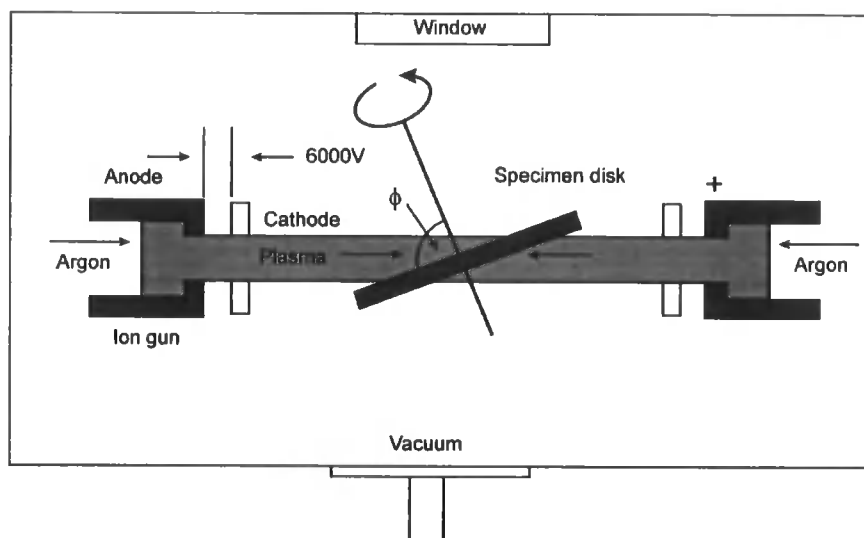


**Figure 3.5:** **Diagram description of the Argon ion thinner [14].**

The use of conventional argon ion milling for preparation of thin TEM samples can result in the generation of serious artefactual specimen structures, such as small crystallographic defects or dislocation loops [12]. It is known that thinning of CdS with I⁺ ions yield specimens with fewer loops that those prepared using Ar⁺. Hence, final iodine thinning was performed in an Ion Tech 800 Series I⁺ miller at 4kV for 2 min. However,

the iodine milling apparatus was not equipped with a cooling system and also has only one operating gun.

## 3.3.2 Thin Film CdS

3.05 mm disc were drilled from a 1 mm thick sample with the thin film facing downwards. A gold support ring was then glued to the layer of interest. Each sample was then mounted on the Gatan grinder stub with the glass substrate emergent. The sample was polished mechanically to a thickness of <50 μm, using the technique described previously. After removing and cleaning with trichloroethane, it was glued onto a 1 cm$^2$ microscope slide, with glycol phthalate. The glycol phthalate was made of 148 g of phthalic anhydride and 62 g ethylene glycol, which was heated at 200°C for 24 hours. The glass substrate was then turned to face upwards so that the thin film was then directly in contact with the glue. The edges of the sample were then protected with paraffin wax.

The samples were then dipped into 20% hydrofluoric acid for glass removal. The glass etching rate depends on the thickness of the sample and the HF concentration. Since there is no technique to control the remaining layer which has been attacked by the HF, every 15 minutes the HF treatment was interrupted to check the remainder of the layer. The samples were rinsed with distilled water, then residues were removed in an ultrasonic bath. They were then dipped in acetone to remove the glycol phthalate glue, and cleaned with trichloroethane. Therefore, the HF treatment was only performed until the glass substrate was perforated to avoid accidental etching of the CdS layer. Figure 3.6 shows a schematic description of the sample preparation.
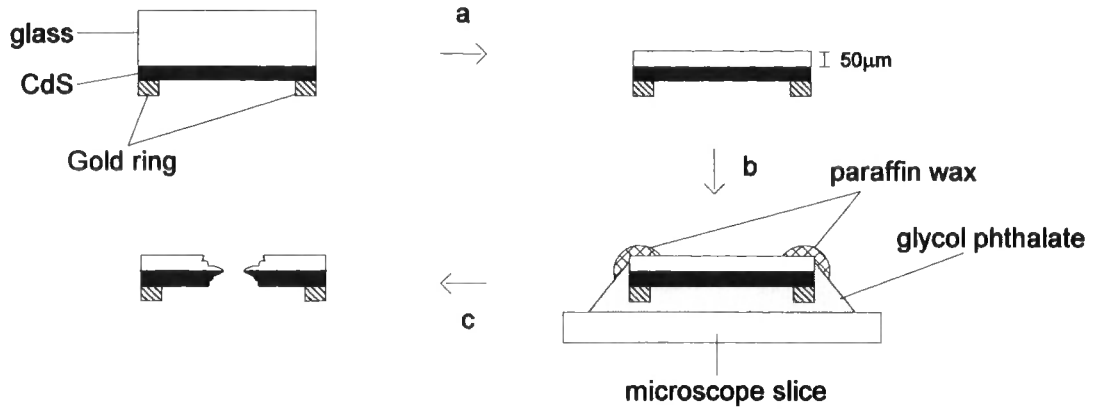
**Figure 3.6:** Schematic description of sample specimen preparation: a) mechanical thinning on Au ring, b) mounted for glass removal, and c) final sample (with accidental perforation).

Samples prepared in this way were electron transparent and no further ion thinning was essential. Occasionally there was accidental perforation as shown in Figure 3.6c.

# 3.4 Characterisation Methods

## 3.4.1 Optical Transmittance

Light moving through a medium will split up into three parts: some will be transmitted, some reflected and some will be absorbed. Absorption occurs when incident photons have energies greater than the energy bandgap of the material, the loss of the intensity of radiation transmitted as it passes through a medium can be given as:

$$T = (1 - R)\exp(-\alpha d)$$ Eq. 3.6

where $T$ is the transmittance, $R$ is the reflectance $\alpha$ is the absorption coefficient and $d$ is the thickness of the medium. In a simplified model we can assume that the reflectance is negligible therefore the absorption can rearranged to give:

$$\alpha = -\frac{1}{d}\ln(T)$$ Eq. 3.7

Calculating values of $\alpha$ it is possible to plot graphs of $(\alpha h v)^2$ *vs* $hv$, which can be extrapolated back to give the energy bandgap of the material (where $h$ is the Planck's constant and $v$ is the frequency. With transmission spectra it is common to observe interference fringes and it is possible from the data to estimate the materials refractive index $n$ if the thickness $d$ is know, the equation is given by:

$$n = \frac{1}{2d}\left[\frac{\lambda_1 \lambda_2}{\lambda_2 - \lambda_1}\right]$$ Eq. 3.8

where $\lambda$ is the wavelength, the indexes are referred to maxima and minima.

Optical transmittance measurements were performed in a Perkin Elmer Lambda 19 UV-VIS spectrophotometer.

## 3.4.2 Photoluminescence

### 3.4.2.1 Introduction

Photoluminescence (PL) spectroscopy is a non-destructive technique which is mainly used as a diagnostic tool for semiconductors, with its powerful and sensitive ability to find impurities and defects in semiconductors [16], which affect materials quality and device performance. A given impurity produces a set of characteristic spectral features. This fingerprint identifies the impurity type, and often several different impurities can be seen in a single PL spectrum. In another use, the linewidths of the PL peaks are an indication of sample quality and crystallinity, although such analysis has not yet become quantitative [17]. Finally, PL is very sensitive to stress, and can measure its magnitude and direction [18].

### 3.4.2.2 Principle

Figure 3.7 gives an overview of the main processes that occur when light is emitted from a solid. The photon is emitted when an electron, in an excited state drops, down into an empty state in a lower state band. For this to be possible, electrons must be first injected, then relax to the state from where the emission occurs. This could be the bottom of the conduction band, but it might also be a discrete level. The photon cannot be emitted unless the lower level for the transition is empty, because the Pauli principle does not permit us to put two electrons at the same level. The empty lower level is produced by injecting holes into the ground band in an entirely analogous way to the injection of the electrons into the excited state. The radiative recombination is determined by the radiative recombination lifetime $\tau_R$. Radiative emission has to compete with non-radiative recombination, which has lifetime $\tau_{NR}$.

Radiative recombination in a semiconductor can be divided two classes, (i) *intrinsic* and (ii) *extrinsic*.

In the presence of defect states in the band gap $Eg$, intrinsic recombination is dominated by forming free excitons via Coulomb attraction. The subsequent radiative emission can be expressed as $h\nu = E_g - E_x$ where $h\nu$ and $E_x$ are the energy and the exciton ionisation energy respectively [19].

inject electrons

relaxation

EXCITED
STATE

$\tau_{NR}$   $\tau_R$   $h\upsilon$

GROUND
STATE

inject holes
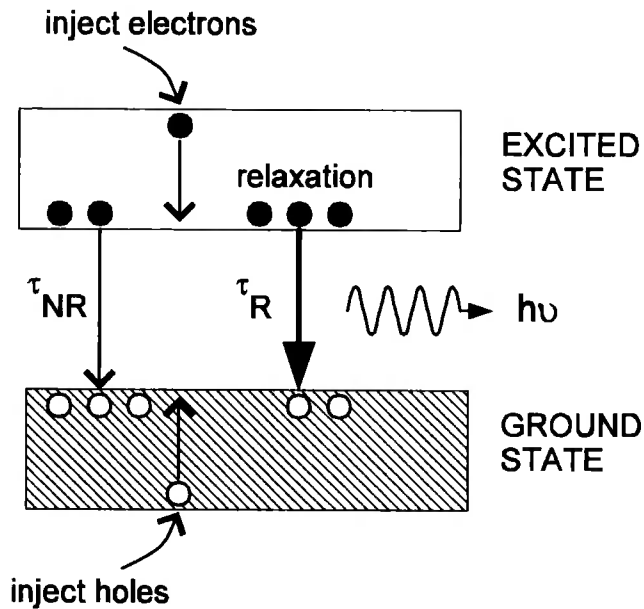
**Figure 3.7:** **General schematic of luminescence in a solid [20].**

Extrinsic recombination mechanism is a result of states associated with donors, acceptors, and native defects. Extrinsic states are classified as shallow or deep, where the shallow impurities produce relatively small perturbations that lead to the formation of bound states in the forbidden gap very close to the boundaries of the conduction and valences bands. While deep impurities states usually produce stronger perturbations, lie deeper in the gap and are more localised. The information about these deep centres is crucial in the analysis of luminescent materials, since they usually act as efficient recombination centres or traps and control the carrier lifetime.

In the presence of impurities, bound excitons can be formed with recombination characterised by narrow emission lines of energy $h\nu = E_g - E_x - E_b$

where $E_b$ is the binding energy of the exciton to the impurity atom. In addition, an exciton can be bound to crystal lattice via electron-phonon interaction. Spectral peaks can be observed with energy $h\nu=E_g-E_x-E_b-mE_{ph}$ where $E_{ph}$ is the energy of emitted phonons and $m$ is the number of phonons emitted [19]. A schematic diagram of the emission mechanism is shown in Figure 3.8. At low temperature free exciton recombination is much more likely than band to band.

$E_C$ _____

$E_g$

$E_D$   $E_D$   $E_X$

$E_A$   $E_A$   $E_A$

$E_V$ _____

a    b    c    d    e
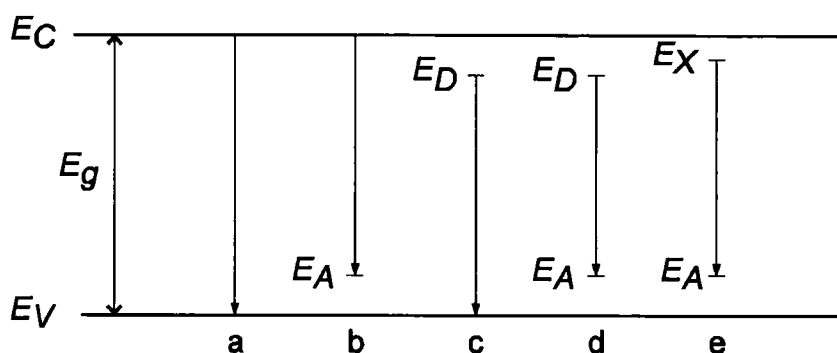
**Figure 3.8:** **Five major possible radiative recombination processes: a) direct conduction band-valence, b) conduction-acceptor , c) donor valence band, d) donor-acceptor transition, e) bound exciton recombination [21].**

## 3.4.2.3    Experimental Aspects

Photoluminescence spectra were recorded with the experimental arrangement shown schematically in Figure 3.9. The sample was mounted in a temperature cryostat and is illuminated with an argon ion laser, from which the 458 nm line was selected using a band-pass interference filter. The sample was mounted in an optical closed-cycle helium cryostat, resulting in a nominal temperature of 4K. The luminescence is emitted at lower frequencies and in all directions. A portion is collected with a lens and focussed onto a slit of a spectrometer and measured at each wavelength with a photodiode array interfaced to a computer. Reflected laser light was blocked from the detection system by the use of a colour glass edge filter. The cryostat was mounted on a manual XYZ stage to allow moving the sample with respect to the laser spot.

A  Argon ion laser
B  Band-pass filter
C  Spatial filter
D  Lens
E  Optical cryostat
F  Pipes to compressor
G  Sample
H  XYZ stage
I  Edge filter
J  Monochromator
K  Photodiode array
L  Computer
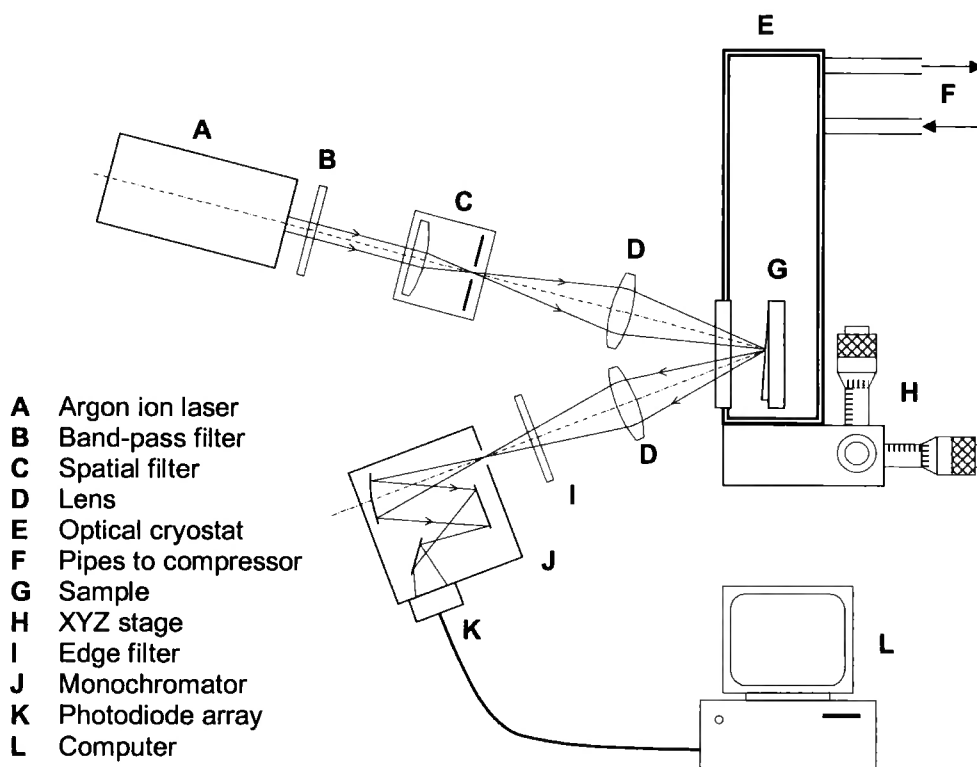
**Figure 3.9:   Experimental arrangement used for the observation of photoluminescence spectra [22].**

## 3.4.3 Scanning Electron Microscopy

Scanning electron microscopy (SEM) is non-destructive technique for investigating the surface morphology of materials.   SEM consists of a focused electron beam (with an accelerating voltage between 1-40kV) which is scanned across an area of the sample.  SEM images can be built up from different operation modes:   backscattered or secondary electrons.   In this study, SEM was performed on a JEOL JSM-IC848 operating in secondary electron mode with a 20kV accelerating voltage.  Details of the construction and mode of operation are reported [13, 14, 23-28].   However, a brief description of backscattered and secondary electron mode is described below.

**Backscattered electron mode**   Backscattered electrons are primary electrons which have been elastically scattered by Coulombic interactions with atomic nuclei within the sample. After single or multiple elastic collisions, they may be scattered through a large angle so that they re-emerge form the incident surface as backscattered electrons.

The probability that an electron will be scattered by the nucleus is affected by the beam energy, the angle of scattering and the atomic number. Backscattered electrons can provide some compositional information.

**Secondary electron mode**   The most common imaging mode monitors low energy (<50 eV) secondary electrons. Due to their low energy, these electrons must originate within a few tenths of a nanometer from the surface. They are generated through the interaction of the primary beam with loosely bound conduction electrons. The secondary electron mode is commonly used for surface topography analysis.

## 3.4.4 Glancing Incident X-Ray Diffraction

X-Ray diffraction (XRD) is a non-destructive method for investigating the structural properties of a material – properties such as the crystalline phase in thin films and thin film structure. XRD methods are based on the scattering of X-rays by the atoms in a lattice.

X-rays have a wavelength comparable to the interatomic distances in crystals. Thus, when atoms scatter X-rays, constructive interferences take place at given angles of incidence beam for given X-ray wavelength $\lambda$. Constructive interference occurs when the path length for rays scattered from the neighbouring planes of atoms is an integral number of wavelength, $n\lambda$, where n is an integer. Under this Bragg condition (Eq. 3.9) the diffracted intensity is strong. The equation describing this condition is:

$$n\lambda = 2d_{hkl}\sin\theta_B \hspace{4cm} \text{Eq. 3.9}$$

where λ is the wavelength of the X-rays, $n$ is an integer, $d_{hkl}$ is the spacing of adjacent parallel planes <hkl> of atoms, and $\theta_B$ is the Bragg angle for diffraction. '$n$' therefore represents the order number of the diffraction from planes of atoms of separation $d_{hkl}$.
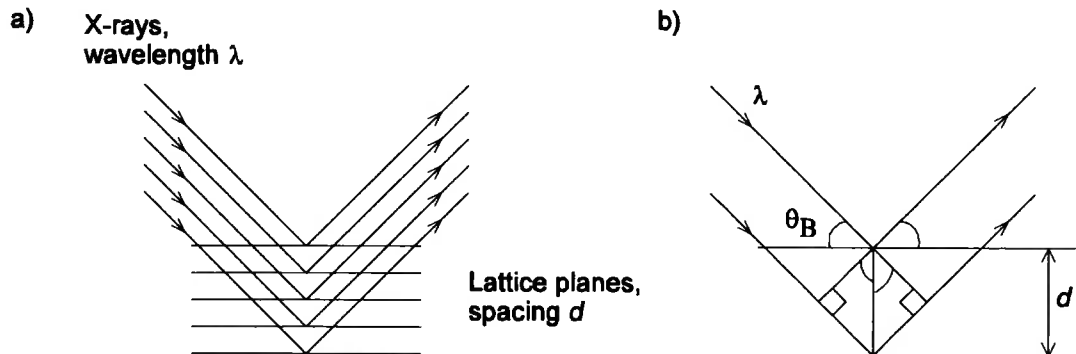


**Figure 3.10: Bragg diffraction from planes of atoms in a crystals; (b) shows part of (a) in detail. All angles marked with arcs are equivalent to the Bragg angle $\theta_B$.**

Two configurations are commonly applied for thin-film XRD analysis: *symmetric* Bragg-Brentano [29] geometry and asymmetric geometry (Figure 3.11). In both configurations the x-ray source intensity and angular dispersion are fixed by the take-off angle from the x-ray source to the entrance slit of the detector. The angular distribution, $h(2\theta_d)$ obtained on the detector arc represents the convolution of the optical transformation, $g(2\theta)$, with the specimen lattice distortion function $f(2\theta)$ [30].

$$h(2\theta) = \int_{-\infty}^{+\infty} g(2\theta)f(2\theta - \delta)d\delta$$

Eq. 3.10
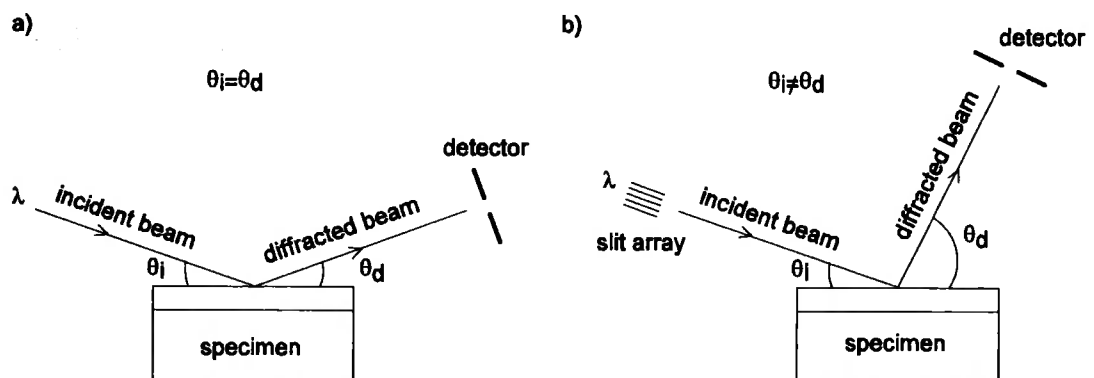


**Figure 3.11: Symmetric (a) and asymmetric (b) thin-film x-ray diffraction measurement configurations [31].**

The symmetric condition, $\theta_i=\theta_d$ , constrains the measurement to the lattice planes parallel to the specimen plane. The asymmetric condition, with $\theta_i\neq\theta_d$ and using a fixed incident beam angle, constrains the measurement to populations of lattice planes that are tilted with respect to the specimen plane (Figure 3.12). The angle of the diffracting plane to the substrate surface is $(\theta_d-\theta_i)$ limits therefore the detection of the (hkl) planes. This makes it more difficult to get preferred orientation from GIXRD than from $\theta$-$2\theta$ XRD.
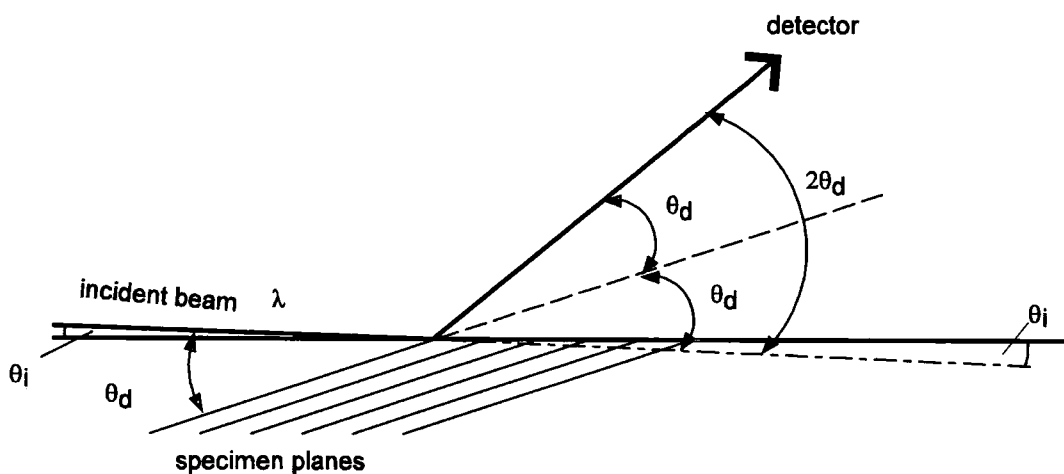


**Figure 3.12: Geometrical relationship for asymmetric GIXRD measurements, showing fixed-incident x-ray beam and lattice planes satisfied diffraction condition.**

Asymmetric measurements made with low beam angles are referred to as glancing incidence X-ray diffraction (GIXRD). As the incident x-rays are at grazing angle, this technique is inherently depth sensitive. The detector and the sample are scanned in the plane of the film with the diffraction planes perpendicular to the sample plane, measurements are therefore sensitive to in-plane crystalline structure and layer quality to depth of the order of 30-50Å from the surface layer.

Hence, glancing incidence X-ray diffraction measurements were performed with a Bede D1 System diffractometer.

### 3.4.4.1    Grain size and deformation strain

Information on grain size and strain is obtained from the shape and position of the diffraction peaks respectively. The strain within a crystal affects the $d$ spacing and therefore the position of the diffraction peaks and the grain size has an effect of broadening the peaks.

The effect of grain size on the width of the diffraction peak is given by the Scherrer's equation:

$$\Delta_{size}(2\theta) = \frac{\kappa\lambda}{D\cos\theta}$$    Eq. 3.11

where $\Delta_{size}(2\theta)$ is the width of the peak in radians, $\lambda$ the wavelength, $D$ the grain size, $\theta$ the Bragg angle and $\kappa$ a constant approximately equal to unity depending both on the line shape profile of the peaks and the crystallite shape.

The peak can also be broadened by micro-strains, $\varepsilon$, within the crystal or powder. These strains cause variations in the $d$ spacing, $\Delta d$ and consequently cause a broadening of the diffraction peak. Differentiating Bragg's law yields:

$$\Delta_{strain}(2\theta) = 2\varepsilon\tan\theta$$    Eq. 3.12

where $\Delta_{strain}(2\theta)$ is the width of the peak in radians.

If both strain and size effects occur within the sample, the width of the diffraction peak is the sum of Equations 3.11 and 3.12 and by rearranging the equation:

$$\Delta_{total}(2\theta)\cos\theta = \frac{\kappa\lambda}{D} + 2\varepsilon\sin\theta$$    Eq. 3.13

A plot of the width multiplied by cosine of the Bragg angle against the sine of the Bragg angle allows the two broadening terms to be separated and measured and is referred to as the Williamson-Hall plot [32].

### 3.4.4.2    Crystallographic orientation

Data have been analysed for preferential orientation using [33]

$$
C_{hkl} = \frac{\dfrac{I_{hkl}}{I_{r,hkl}}}{\dfrac{1}{n}\sum \dfrac{I_{hkl}}{I_{r,hkl}}}
\qquad\qquad\text{Eq. 3.14}
$$

where $C_{hkl}$ is the texture coefficient, $I_{hkl}$ is the intensity of the hkl reflection and $I_{r,\,hkl}$ the intensity of the hkl reflection for a random sample and $n$ is the number of reflections.   The texture coefficient gives a measure of the orientation of each reflection compared to a completely randomly oriented sample.  A value of 1 represents random orientation, while a value of above 1 means preferential orientation in that direction.  In this study, reflections from the hexagonal structure of CdS were considered.

To analyse the preferential orientation of each sample as a whole, the standard deviation σ of all $C_{hkl}$ values as compared to randomly oriented sample was used.

$$
\sigma = \sqrt{\frac{\sum_{i=1}^{n}(C_{hkl}-1)^2}{n}}
\qquad\qquad\text{Eq. 3.15}
$$

Values of σ can be used to compare the degree of orientation between sample.  A value of 0 indicates a completely random sample [34].

## 3.4.5 Transmission Electron Microscopy

Transmission Electron Microscopy is a well-established technique for the study of defects in semiconductor materials.  The reader is referred to relevant textbooks and review articles [13, 14, 35].  In this study, TEM was performed on a JEOL 200CX (with a scanning unit) operating at 80 to 200kV.   TEM was used in four basic modes of operation: bright and dark field microscopy, selected area diffraction and scanning transmission electron microscopy (STEM).  These are described briefly below.

### Selected Area Diffraction (SAD)

The great advantage of this technique is to select a specific area of the specimen to contribute to a diffraction pattern and to reduce the intensity of the pattern falling on the screen, by inserting an aperture into into the image plane of the objective lens.

### Bright Field (BF) Microscopy

A bright field image is formed if the direct (undeviated) beam is used by inserting the objective aperture into the back focal plane of the objective lens.

### Dark Field (DF) Microscopy

Dark field image is formed by selecting some scattered electrons of any form with the objective aperture. This may be achieved either by displacing the objective aperture off-axis or by adjusting the incident beam tilt and centering the objective aperture: this operation is so the called centered dark-field (CDF) imaging.

### Scanning Transmission Electron Microscopy (STEM)

The electron beam is focused to a small probe (10nm) when operating in the STEM and this probe is scanned across the specimen. With a thin specimen, transmitted electron beam can be collected by a transmission detector and the intensity of these electrons used to modulate the intensity of a synchronously scanned CRT to form an image.

Diffraction contrast in STEM images always show lower contrast than images in TEM and noisier images. This observation can be demonstrated by the reciprocity principle. This condition is shown in Figure 3.13, where $\alpha_T$ is the TEM convergence semi-angle, $\beta_T$ is the semi-angle of the objective aperture collection. The equivalent angles in STEM mode are $\alpha_S$ and $\beta_S$ defined as the convergent beam and detection collection

angles respectively. Therefore STEM and TEM will be operating identically if only:

$$\alpha_s = \beta_T \qquad\qquad \text{Eq. 3.16}$$

$$\alpha_T = \beta_s \qquad\qquad \text{Eq. 3.17}$$
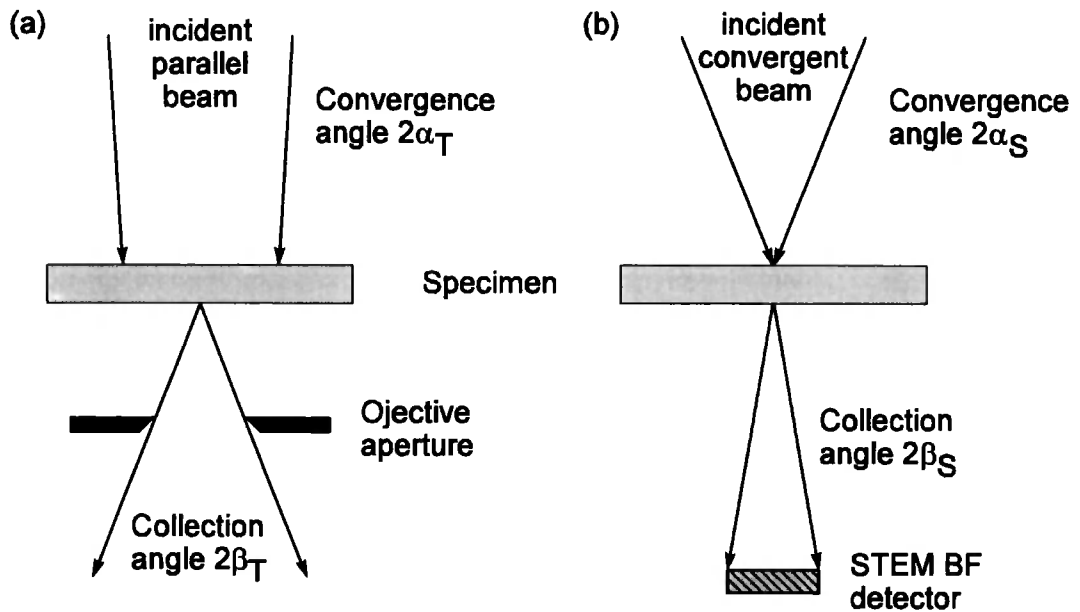
**Figure 3.13: Comparison of the important beam-convergence and divergence angles (a) in TEM and (b) in STEM [24].**

The first condition is then easily satisfied since the objective aperture is about equivalent to the convergence angle in STEM. However, to satisfy the second condition, STEM collection semi-angle $\beta_s$ should be reduced, which can't be done by simply increasing $\alpha_T$, because strong contrast is better when $\alpha_T$ is smaller.

### Calibration

A standard *Agar* gold sample was used to calibrate the magnification and the camera length in TEM and STEM, whereas image rotation was calibrated using a [001] direction of molybdenum oxide crystals.

# 3.5 TEM-CL Principle

A Jeol 200CX TEM was adapted to allow the simultaneous collection of CL and transmitted electrons using Oxford Instruments (Oxford, UK) MonoCL2 for TEM. The systems consists of a CL collection mirror, 0.3 m spectrometer, a Peltier cooled Burle C31034 phtomultiplier tube, PA3 photoamplifier supply and stepper driver and ISIS 300 control system. A description of TEM-CL apparatus and techniques used for recording CL spectra and forming panchromatic and monochromatic images is given below. The reader is referred to relevant textbooks and review articles describing in detail the TEM-CL.

**(a)**

**(b)**



collection mirror

to spectrometer

$LN_2$ stage
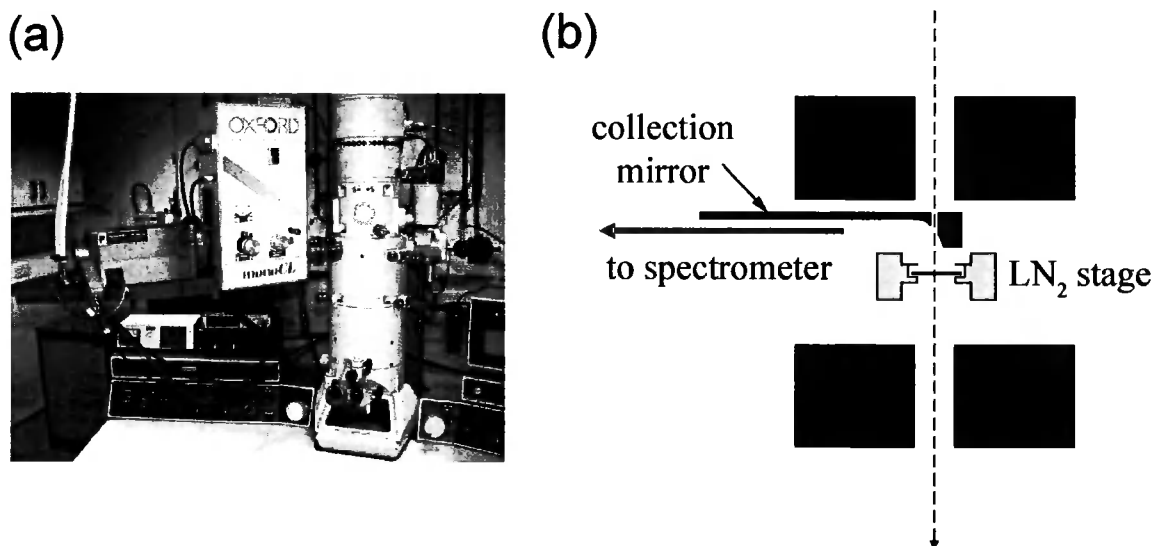
**Figure 3.14: (a) Photograph of JEOL 200CX with TEM-CL attachment, (b) diagram showing TEM-CL mirror in the collection above the specimen holder**

## 3.5.1.1   CL Collection Mirror

CL from the TEM foil is collecting using Oxford CL302 collection system which is composed of a retractable parabolloidal aluminium mirror collecting and guiding the CL either to the slits of the monochromator or directly to the photomulplier tube for panchromatic imaging. The mirror has a hole directly above the focal point of the mirror for the electron beam. When the specimen is at the focal point, CL generated by the specimen is collected in very efficient manner and collimated along one axis of the mirror, at right angles to the incident electron beam. To obtain optimum

CL collection emission from unexposed thin film section of the specimen was used to position the mirror above the sample holder 0.5-1.0 mm, as the focus of the mirror is 1.0 mm. Optimization of the CL emission was achieved by varying the three positioning screws for X, Y and Z directions. Care was taken not to collide the mirror with the sample holder.

### 3.5.1.2    TEM-CL LN$_2$ Specimen Holder

Due to the restricted space in the microscope pole piece and the required separation distance of 1 mm between the mirror and the specimen, an Oxford Instruments CT3500TR Tilt-Rotate Cryo-Transfer holder was used. The sample was maintained in a cradle using a screwed ring to perform a good thermal contact. The cradle is cooled by a short braid and conduction rod from a nitrogen dewar. Rotation of sample is controlled by Oxford Instruments Digital Tilt Indicator. After insertion of the mirror, the sample tilting is not possible due to the proximity of the mirror.

Once the specimen holder was inserted inside the TEM, the dewar can be filled with liquid nitrogen approximately 15 minutes after the contamination trap on the TEM was cooled. The temperature is controlled and monitored by an Oxford Instruments ITC502 Temperature controller. The lowest temperature achievable is 90K. After stabilisation no need to refill the dewar is required, and specimen tilt drift is insignificant.

### 3.5.1.3    Monochromatic and Panchromatic Modes

In panchromatic mode, all the light is directed at the detector. This allows the combined intensity of all CL wavelengths within the response of the detector to be imaged.

In monochromatic mode, all the light is coupled into a 0.3 m monochromator. The spectrometer was fitted with two 150 lines/mm gratings blazed for a maximum transmission at 300 and 500 nm. The spectral dispersion was 21.6 nm/mm. The monochromator entrance and

exit were set between 0.5 and 1.0 which yields a dispersion of 10.8 to 21.6 nm.

## 3.5.1.4    Spectral acquisition

Spectra were recorded from the LINK ISIS 300 control system using the PA3 photoamplifier supply and stepper driver with integration times varying from 1 ms to 10 s.

## 3.5.1.5    CL Imaging and Line-Scans

Using LINK ISIS 300control system, panchromatic and monochromatic CL imaging was performed.   Images can be recorded with different resolution of 128×100, 256×200, 512×400 and 1024×800 pixels.   Dwell times between 100 and 12800 μs resulted a range of 1.5 s to ~3 hours for image acquisition.  Line-scans were also recordable with an integration time varying from 1 ms to 10 s with 1 to 10000 data points.

# 3.6 References

1. W. W. Piper and S. J. Polich, *Vapor-Phase Growth of Single Crystals of II–VI Compounds*, J. Appl. Phys. **32** (1961) 1278

2. K. Durose, A. Turnbull, and P. D. Brown, Mat. Sci. Eng. B **16** (1993) 96

3. C. D. Lokhande, *Chemical deposition of metal chalcogenide thin films*, Materials Chemistry and Physics **27** (1991) 1-43

4. P. K. Nair, *Semiconductor thin films by CBD for solar energy related applications*, Solar Energy Materials **52** (1998)

5. O. Savadogo, *Chemically and electrochemically deposited thin films for solar energy materials*, Solar Cells Materials **52** (1998) 361-388

6. I. Grozdanov, *A simple and low-cost technique rf electroless depostion of chalcogenide thin films*, Semicond. Sci. Technol. **9** (1994) 1234-1241

7. K. Govender, *Solution deposition and applications of compound semiconductor thin films*, (2003), University of Manchester

8. M. D. Archbold, D. P. Halliday, K. Durose, T. P. A. Hase, D. Smyth-Boyle, and K. Govender, *Characterisation of thin film cadmium sulfide grown using a modified chemical bath deposition bath deposition process*, 31st IEEE Photovoltaic Specicalists Conf., Lake Buena Vista, Florida, U.S.A. (2005)

9. A. C. Jones and P. O'Brien, *CVD of Compound Semicondcutors - Precursor Synthesis, Development and Applications.* (1997) VCH

10. S. J. C. Irvine, A. Hartley, and A. Stafford, *In situ monitoring of the MOCVD growth of CdS/CdTe*, Journal of Crystal Growth **221** (2000) 117-123

11. R. A. Berrigan, N. Maung, S. J. C. Irvine, D. J. Cole-Hamilton, and D. Ellis, *Thin films of CdTe/CdS grown by MOCVD for photovoltaics*, Journal of Crystal Growth **195** (1998) 718-724

12. J. Bravman, R. M. Anderson, and M. M.L., *Speciment preparation for transmission electron microscopy of materials.*, Material Research Society Symposium Proceedings, Boston Massachusetts, USA (1987)

13. P. B. Hirsch, A. Howie, R. B. Nicholson, D. W. Pashley, and M. J. Whelan, *Electron Microscopy of Thin Crystals.* (1965) Spottiswoode, Ballantyne & Co. Ltd.

14. D. B. Williams and C. B. Carter, *Transmission Electron Microscopy - Basics.* (1996) Plenum Press

15. P. J. Goodhew and F. J. Humphreys, *Electron microscopy and analysis.* 2nd edition (1988) Taylor & Francis

16. D. K. Schroder, *Semiconductor material and device characterization / Dieter K. Schroder.* (1990) Wiley.

17. M. Cárdenas, J. G. Mendoza-Alvarez, F. Sánchez-Sinencio, O. Zelaya, and C. Menezes, *Photoluminescent properties of films of CdTe on glass grown by a hot-wall-close space vapor transport method*, Journal of Applied Physics **56** (1984) pp. 2977-2980

18.  S. Perkowitz, *Optical characterization of semiconductors : infrared, raman, and photoluminescence spectroscopy / Sidney Perkowitz.* (1993) Academic Press,

19.  V. I. Petrov, *Cathodoluminescence microscopy*, Physics - Uspekhi **39** (1996) 807-818

20.  A. M. Fox, *Optical properties of solids.* (2001) Oxford University Press

21.  D. B. Holt and D. C. Joy, *SEM microcharacterization of semiconductors.* (1989) Academic P.

22.  P. R. Edwards, *Beam-induced current studies of CdTe/CdS solar cells.* (1998)

23.  P. B. Hirsch, *Topics in electron diffraction and microscopy of materials.* (1999) Institute of Physics Publishing

24.  D. B. Williams and C. B. Carter, *Transmission Electron Microscopy - Imaging.* (1996) Plenum Press

25.  D. B. Williams and C. B. Carter, *Transmission Electron Microscopy - Diffraction.* (1996) Plenum Press

26.  S. S. Amelinckx, R. Gevers, and J. V. Landuyt, *Diffraction and imaging techniques in material science.* , 2nd revised ed. (1978) North-Holland Publishing Co.

27.  L. Reimer, *Transmission Electron Microscopy, Physics of Image Formation and Microanalysis.* (1984) Springer-Verlag

28.  D. Chescoe and P. J. Goodhew, *The operation of transmission and scanning electron microscopes.* (1990) OUP

29.  J. C. M. Brentano, *Parafocusing Properties of Microcrystalline Powder Layers in X-Ray Diffraction Applied to the Design of X-Ray Goniometers*, Journal of Applied Physics **17** (1946) 420-434

30.  H. P. Klug and L. E. Alexander, *X-ray diffraction procedures for polycrystalline and amorphous materials.* 2d ed. (1974) Wiley

31.  K. Durose, *Physical charactrisation of thin-film solar cells*, Progress in photovoltaics: Research and Applications **V12** (2004) 117-217

32.  G. K. Williamson and W. H. Hall, *X-ray line Broadening from filed aluminium and wolfram*, Acta Metall. **1** (1953) 22-31

33.  C. S. Barrett and T. B. Massalski, *Structure of metals : crystallographic methods, principles, and data.* 3rd ed. (1966) McGraw-Hill

34.  H. Moutinho, R. G. Dhere, M. M. Al-Jassim, D. H. Levi, and L. L. Kazmerski, *Investigation of induced recrystallisation and stress in close-spaced sublimated and radio-frequency magnetron sputtered CdTe thin films*, J. Vac. Sci. Technol. A **17** (1999) 1793-1798

35.  L. Reimer, *Transmission electron microscopy : physics of image formation and microanalysis / Ludwig Reimer.* (1984) Springer,

# The TEM-CL signal

## 4.1 Introduction

In the first part of this chapter the principles of cathodoluminescence (CL) and X-ray generation are outlined. In the second part, a convolution method is described for estimating the spatial resolution of CL microscopy images. Finally, an experimental study of the TEM-CL signal quality, which can be expressed by the signal-to-noise ratio $S/N$, is reported.

## 4.2 Formation of CL radiation

The three fundamental processes that result in CL emission are the generation, motion and recombination of excess electrons and holes. These processes will be considered individually.

### 4.2.1 Generation of nonequilibrium charge carriers

Primary (fast) electrons striking the object undergo energy losses due to interaction with the solid, and then stop. In order to evaluate the

electron range the Bethe expression [1] for the mean rate of energy loss per segment of distance S travelled in the solid is given as

$$\frac{dE}{dS} = -2\pi e^4 N_A \frac{\rho Z}{EA} \ln\left(\frac{1.166E}{J}\right)$$

Eq. 4.1

where $e$ is the electronic charge, $N_A$ is Avogadro's number, $\rho$ is the density, $A$ is the atomic weight, $Z$ is atomic number, $E$ is the mean electron energy and $J$ is the mean ionisation potential. The electron range is found by integration.

The secondary processes caused by electron bombardment proceed in the energy dissipation area, the so called generation volume. Its dimensions are close to the value of penetration depth $R_e$ which , according to Kanaya and Okayama [2], is

$$R_e = \frac{0.0276A}{\rho Z^{0.889}} E_0^{1.67} \quad (\mu m)$$

Eq. 4.2

where $A$ is in g.mol$^{-1}$, $\rho$ is in g.cm$^{-3}$, and $E_o$ is the electron probe energy in keV.

It is also important to emphasise the difference in excitation volumes of the thin target and the bulk samples (see Figure 4.1).
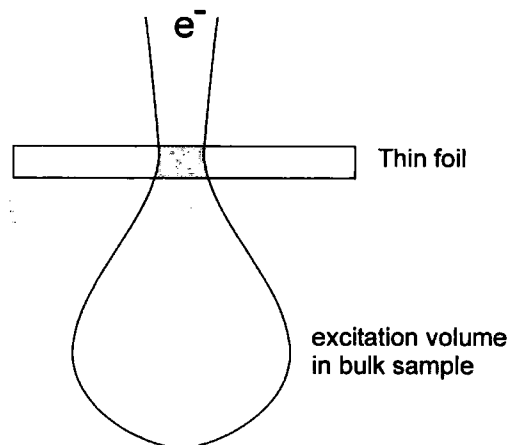


**Figure 4.1:    Excitation volume in a thin specimen and a bulk sample.**

The generation factor $G$ (i.e., the number of electron-hole pairs generated per incident beam electron) is given by

$$G = \frac{E_b(1-\gamma)}{E_i}$$

Eq. 4.3

where $E_b$ is the electron beam energy, $E_i$ is the ionisation energy (i.e. the energy required for the formation of electron-hole pairs), and $\gamma$ represents the fractional electron beam energy loss due to backscattered electrons.

## 4.2.2 Nonequilibrium carrier motion and recombination

Nonequilibrium charge carriers generated in a semiconductor material acquire directional motion by diffusion (due to concentration gradient) and drift (due to electric field) processes, prior to recombination. Depending on the mechanism, three modes of recombination can be recognised: interband recombination, recombination via localised states in the gap and surface recombination. Recombination may be radiative with photon emission as well as nonradiative with phonon emission, or to another electron which changes to a higher-energy state in the conduction band (Auger effect).

For continuous irradiation and the electron beam at a fixed position on the object, the action of all these processes results in the formation of stationary excess-minority carrier distribution which is governed by the three-dimensional differential equation of continuity. In the simplest case for electrons in a p-type semiconductor it can be written as

$$D\nabla^2 \Delta n(r) - \frac{\Delta n(r)}{\tau} + G(r) = 0$$

Eq. 4.4

with a boundary condition at the object surface

$$D\frac{\Delta n(r)}{\delta z}\bigg|_{z=0} = \upsilon_s \Delta n(r)\big|_{z=0}$$

Eq. 4.5

where $\Delta n(r)$ is the excess-carrier density per unit volume, $D$ is the diffusion coefficient, $\tau$ is the minority carrier lifetime, $\upsilon_s$ is the surface recombination velocity, $G(r)$ is the generation function of electron-hole pairs defined by the electron beam parameters and the energy loss density distribution in the object, and finally the $z$ is the coordinate from the surface into the object [3].

The intensity $I_{CL}$ of the CL emission which is usually accepted as being proportional to $\Delta n(r)$, can be written as [4]

$$I_{CL} = \int_V AB\eta(r)\Delta n(r)dV \qquad \text{Eq. 4.6}$$

where $A$ and $B$ are constants and defined as the correction factors for CL absorption losses inside the object, while the light is passing through the object material, and the CL reflection losses at the object-vacuum boundary, respectively, and $\eta(r)$ is the internal quantum efficiency defined as the ratio of the radiative recombination rate to the total recombination rate. The internal quantum efficiency is usually expressed in terms of carrier lifetimes – radiative $\tau_{rr}$, and nonradiative $\tau_{nr}$ as

$$\eta = \left(1 + \frac{\tau_{rr}}{\tau_{nr}}\right)^{-1} \qquad \text{Eq. 4.7}$$

Besides intensity, the CL radiation is also characterised by its spectrum. The photon energies and, therefore, CL radiation spectrum contain information about characteristic energy levels. Radiative transitions can be divided in two classes: (i) intrinsic and (ii) extrinsic. Details of radiative transitions are also presented in section 3.4.2.

# 4.3 Spatial resolution of CL Scanning Microscopy

By definition, the spatial resolution is the minimum distance between two object details which is possible to distinguish using the CL-signal. The spatial resolution $d$ of the CL mode of SEM is affected by the probe size $d_p$, the size of the generation volume $d_g$, which it is related to the beam penetration in the material, and the minority carrier diffusion length $L_d$. The relation between these parameters is given by [5] as

$$d = \sqrt{(d_p^2 + d_g^2 + L_d^2)} \qquad \text{Eq. 4.8}$$

In a bulk semiconductor, the carrier diffusion length $L_d$ is commonly defined as [4]:

$$L_d = \sqrt{D\tau}$$  Eq. 4.9

where, $D$ is a diffusion coefficient, and $\tau$ is the carrier lifetime.

However, in a thin foil the influence of surface recombination increases and no recombination occurs in the bulk [4], i.e. the minority lifetime is only defined by the presence of surfaces and the corresponding diffusion length will take the form

$$L_d = \frac{t}{\pi}$$  Eq. 4.10

where, $t$ is the thin foil thickness.

The divergence $b$ of the primary beam, for a small object thickness $t$, small beam size, and only elastic interactions with the object [4], is given by

$$b \approx \frac{Z}{E_o} \left( \frac{\rho}{A} \right)^{1/2} t^{3/2}$$  Eq. 4.11

Additional factors such as a low signal-to-noise ratio, vibrations, and electromagnetic interference may degrade the resolution in practice.

## 4.4 Monte Carlo Simulation

Monte Carlo (MC) simulation of electron trajectories for multi- layered samples geometries are used for studying the depth and lateral resolution under various experimental conditions, usually found in microscopy [1, 6]. In a simulation a trajectory is calculated for each electron as it undergoes elastic and inelastic scattering.

Monte Carlo simulations were performed using the commercially available MC-SET software [7] and are shown in Figure 4.2. In Figure 4.2(a-d) are the simulations of electron trajectories for various accelerating voltages varying from 80 keV to 200 keV on CdS layers of thickness 200 nm. The beam size was 10 nm. The beam broadening seen in these

simulations is in line with that given by Eq. 5.11. From the figure it can be seen that from these conditions alone, resolution of a 100 nm thick CdS layer should be possible in cross-section in STEM-CL. However, since the beam interaction causes both X-ray and CL emission, the signal recorded may have wider spatial origins than Figure 4.2 would suggest: X-ray luminescence may be excited from other parts of the sample remote the beam itself. This is explored in the following sections.

# 4.5 X-ray Generation and Absorption

When a beam of electron strikes a target or specimen, most electron interactions with atoms result in energy losses as heat generated in the material. The two ways in which the electron may lose energy to X-ray generation are presented below:

i)    A small fraction, 1 part in $10^3$ or less, of the electron interactions, ionise the atoms and may result in the emission of characteristic X-ray photons.

ii)   Some of the incident electrons (the order of 1 part in $10^3$) undergo interactions in which they lose hundreds of thousands of electron volts of energy by decelerating but do not ionise the atoms. The photons emitted in these instances form a spectral continuum; this is often called Bremsstrahlung and appears as an interfering background.

## 4.5.1 Terms related to X-ray measurements

Characteristic X-rays from the different elements are distinguished either by their wavelength, $\lambda$, or by their energy, $E$ depending on the type of measuring equipment employed. Two important parameters control the characteristic X-ray intensity emitted in a specimen: the photon emission yield (fluorescence yield) and the linear attenuation coefficient.
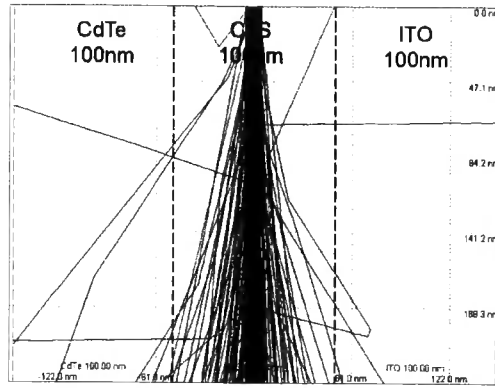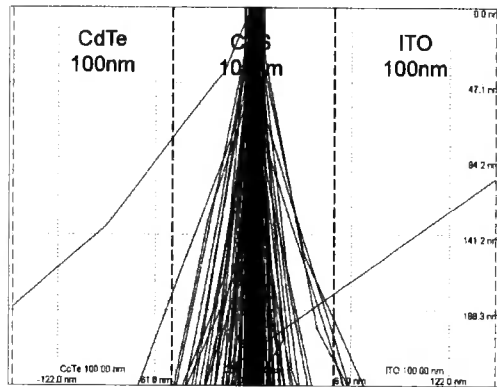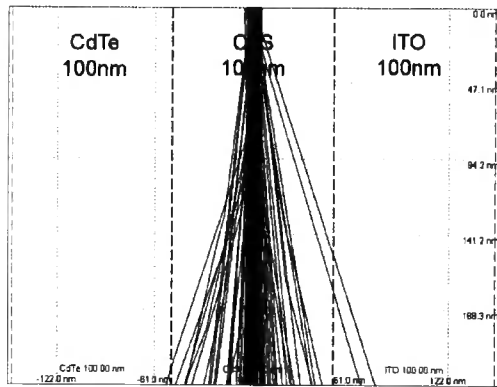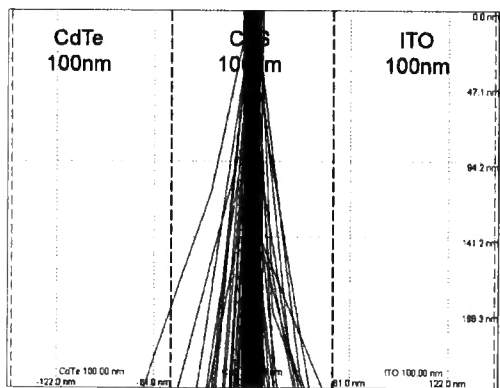
**Figure 4.2:** Monte Carlo simulations for a) 80keV, b) 120keV, c) 160keV, d) 200keV, electron incident on a cross-section of CdTe/CdS/ITO layered structure Each layer is 100 nm while the TEM foil is 200 nm thick.

## 4.5.1.1    Linear attenuation coefficient, μ

When a parallel narrow beam of strictly monochromatic X-rays, with an incident intensity $I_o$, passes through a plane-parallel layer of homogeneous, isotropic material of thickness $x$, with surfaces normal to the beam direction, the emergent intensity $I$ is given by

$$I(x) = I_o \times \exp[-\mu x]$$    Eq. 4.12

where $\mu$ is the linear attenuation coefficient.

## 4.5.1.2    Mass Attenuation Coefficient, μ/ρ

When treating the X-ray transmission in multiple component samples, it is customary to the use mass attenuation coefficient, $\dfrac{\mu}{\rho}$ rather than the linear attenuation coefficient $\mu$ where $\rho$ is the density. The value of the mass attenuation coefficient of mixtures and compound is obtained using the equation

$$\mu_m = \frac{\mu}{\rho} = \sum_i w_i \left( \frac{\mu}{\rho} \right)_i$$    Eq. 4.13

where, $w_i$ is the fraction by weight of $i^{th}$ atomic constituent, $\left( \dfrac{\mu}{\rho} \right)_i$ is the measured value of mass attenuation coefficient of single elements.

For each layer which constitutes a CdS/CdTe solar cell device, the mass attenuation coefficient was calculated from Eq. 4.13 using the X-ray interaction coefficients determined using [8], as shown in Figure 4.3. Hence for the glass, it was assumed that it is mainly composed of silica (i.e. 60-80% $SiO_2$).
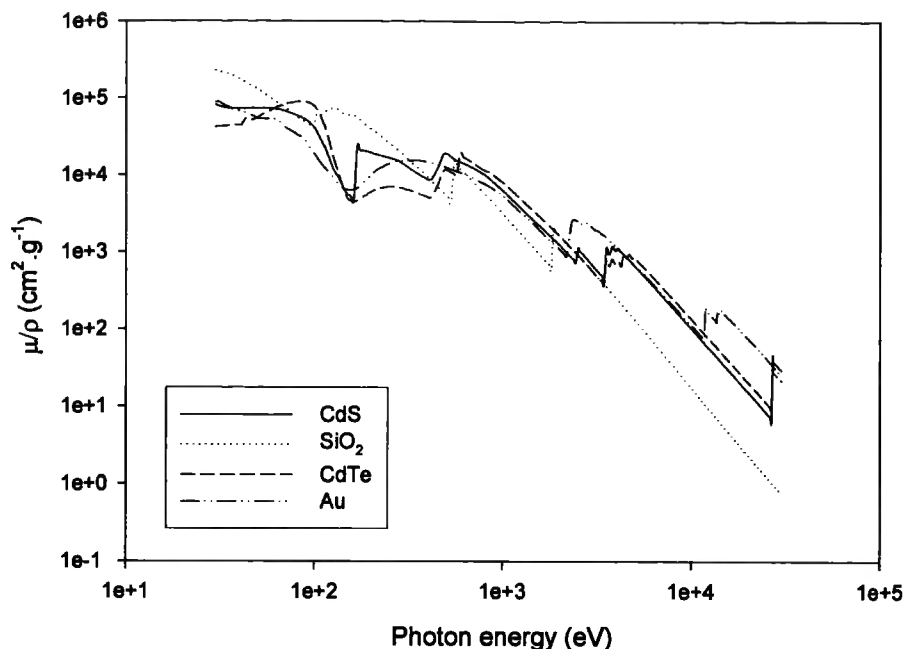
**Figure 4.3:** **Mass absorption coefficient vs. energy for ITO, SiO₂, CdTe and CdS. Data calculated using [8].**

The absorption edges are due to the variation of the true absorption coefficient $\tau$ with wavelength of the absorbed radiation, showing the K, L, M absorption edges [9].

# 4.6 Simulation of Image Width

## 4.6.1 Boyall's Image Width

Boyall [10] has investigated inhomogeneties in GaN epilayers and in $In_xGa_{1-x}N$ quantum wells, combining TEM and CL. A single $In_xGa_{1-x}N$ quantum well on a GaN buffer on a (0001) sapphire substrate was imaged with STEM-CL.

The 10 nm diameter electron beam was focused on the 2.5 nm thick quantum well. Two striking features of the image have been observed:

(a) The quantum well image was 150 nm broad,

(b) The quantum well image had discontinuities on the scale <1 µm, with visible features as small as 0.1 µm.

It was assumed that this breadth (a) might be due to carrier diffusion or secondary luminescence caused by X-rays.

When imaging and mapping with X-rays, the spatial resolution is strongly influenced by the voltage of the electron beam. This is due to the generation volume within which the photons are produced. The spatial resolution of X-ray map is determined by two factors, the size of the incident beam and the spreading the of the electron beam. In this study, as might be expected, we must determine how much light and X-rays are generated either by an electron beam and X-ray emission that results from it.

## 4.6.2 Rechid's Model

Rechid et al. [11] reported a numerical method for the deconvolution of junction electron beam induced current (JEBIC) data from a cross section of a ITO/In$_2$Se$_2$/CIS/Au solar cell. To reveal the diffusion length $L$ and the width of the space region, JEBIC data have to be deconvoluted with the lateral shape of the electron beam excitation.

As long as the electron bulb stays within one material the JEBIC signal is simply defined as the convolution of the local collection probability $D(x)$ and the lateral shape of excitation $g(x)$.

$$JEBIC(x) = \int_{-\infty}^{+\infty} D(x') \times g(x - x') \, dx'$$

Eq. 4.14

with

$$\int_{-\infty}^{+\infty} g(x) = \frac{E_B I_B}{3 E_g e}$$

Eq. 4.15

where $E_B$ is the beam energy, $I_B$ is the beam current, $E_g$ is the energy bandgap and $e$ the elementary charge.

However, when the electron beam is close to the junction, the e-bulb distribution becomes asymmetric over two different materials with different density $\rho_i$ and energy bandgap $Eg_i$.

Basically, to reveal $D(x)$:

- The data are transformed to $\rho x$-space, by changing the density of data by normalising with the relative density $\rho_i/\rho_2$.

- The data can be deconvoluted with $g_2(\varepsilon)$ where $\varepsilon$ is new coordinate in the $\rho x$-space.

- Correct the deconvoluted data amplitude according to the relative area. Finally, transform the data back to real space, by applying $\rho_2/\rho_i$ to the density of data points.

The reader is referred to the convolution method developed by Rechid et al. [11] for more details. This convolution method inspired the simple modelling presented in the following section.

## 4.6.3 Convolution Method

### 4.6.3.1    Principles of the Model

Since there is no unified theory of quantitative CL analysis at present, a model needs to be developed to predict the expected CL intensity and X-ray emission from semiconductor layers generated by either electron or X-ray beam sources. The aim of this modelling is to quantify the CL radiation when the electron beam is moved along a cross-section of a CdS/CdTe solar cell. As mentioned in section 4.2 and 4.5, CL radiation can originate from electron and X-ray sources and CL quantification is very complex. Therefore, simple assumptions have been made and arbitrary values have been used. Hence, a preliminary study of CL quantification is

presented and a simple convolution is described that allows the CL image width resulting from the electron beam and its excited X-rays that go on to induce X-ray luminescence.

As long as the excitation bulb stays within one material the signal is simply the following convolution:

$$D \otimes g(x) = \int_{-\infty}^{+\infty} D(x') \times g(x'-x) dx'$$
Eq. 4.16

where *D(x)* is the radiative emission probability of electron-hole pair recombination and *g(x)* is generation of electron-hole per unit volume. The function *g(x)* can derive from electron (i) and X-ray (ii) sources.

For electron beam excitation, it was assumed that:

$$g(x) = \frac{1}{\sigma\sqrt{2\pi}} \exp\left[-\frac{(x-u)^2}{2\sigma^2}\right] \quad \text{(i)}$$
Eq. 4.17

where $\sigma$ is the standard deviation equal to $\sigma = \dfrac{FWHM}{2\sqrt{2\ln 2}}$ and $u$ the mean.

For X-ray excitation of CL (resulting from the electron beam)

$$g(x) = g_o \times \exp[-\mu_m \times \rho x] \quad \text{(ii)}$$
Eq. 4.18

where $\mu_m$ is the mass attenuation coefficient, $g_o$ is the incident intensity (generated by the electron beam) and $\rho$ the density of the target material.

The case of electron excitation in a thick sample is instructive: in the vicinity of the junction the electron bulb will be asymmetrically distributed over two different materials with different radiative emission probabilities *D$_i$(x)*, product of mass attenuation coefficient *($\mu_m\rho$)$_i$* and electron-hole pair generation rate *g$_i$(x)*. (The index *i* stand for *i$^{th}$* layer). Figure 4.4 shows the excitation bulb of two different materials.
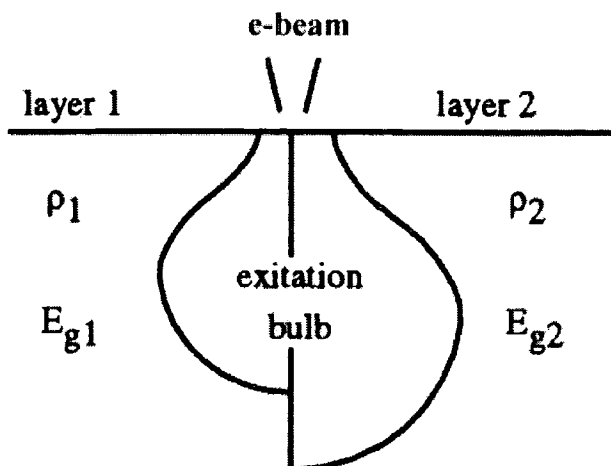
**Figure 4.4:** **Excitation bulb at the interface of materials of two different densities** $\rho_i$ **and bandgap energies** $Eg_i$ ($i=1, 2$)**.**

Instead of strict application of Rechid's method, a direct convolution for a multi-layered system was developed using FORTRAN. A simple program was written to calculate the standard product of convolution of two functions $D_i(x)$ and $g_i(x)$ (see appendices part A).

## 4.6.3.2    Convolution results

### A) The generation of electron-hole pair by X-rays.

It was assumed that the product of the mass attenuation coefficient by the density were identical for the three layers (i.e. $(\mu_m \times \rho)_i$ = constant) and that the X-ray luminescence radiative emission probability was of unity in layer 2 and zero in the others, as shown in Figure 4.5(a-b). The X-rays are considered to be generated within the sample, and to propagate perpendicularly to the interfaces according to the simple exponential law in Eq. 4.12. Figure 4.5(c) shows the convolution of $D(x)\otimes g(x)$. All the luminescence is coming from the layer 2 - this result was expected since the radiative emission probability of layers 1 and 3 were assumed to be zero. It was seen that the broadening of the convolved peak depends highly on

—

$(\mu_m{\times}\rho)_i$ . Other simulations not presented here, show that the convolution peak becomes narrower as the $(\mu_m{\times}\rho)_i$ values increased.

The FORTRAN program developed in this work allowed simulation of any $g_i(x)$ function for any incident emission position. As we can see on the plot, the function $g_i(x)$ is continuous along the $x$ direction and is a function of $(\mu_m\rho)_i$ of each layer. Therefore a "direct" convolution can be straightforwardly applied for cathodoluminescence generated by X-rays. However, a better knowledge of the incident intensity $g_0$, the product $(\mu_m{\times}\rho)_i$ and the radiative emission probability of electron-hole pairs $D_i(x)$ values are required to implement this convolution for a real configuration. For example the real mass absorption contrasts for the compounds of interest would have to be used (Figure 4.3) in conjunction with the spectrum of X-rays generated from each layer by electron beam. This was not attempted in the present work.
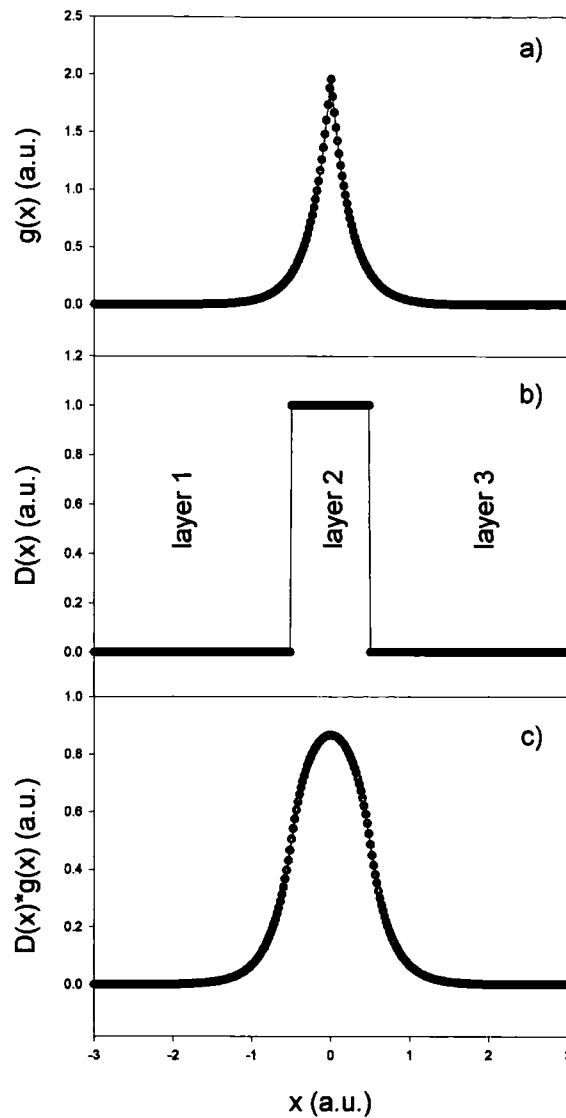
**Figure 4.5:** Convolution of D(x)⊗g(x), when an X-ray source moved over a three layer sample. Penetration of the X-rays perpendicular to the interface is considered. Layer 2 is considered to emit luminescence of a wavelength to which the detector is sensitive.

## B) The generation of electron-hole pairs by an electron beam

The simple convolution can not be directly applied to the generation electron-hole pairs by the electron source since the generation volume depends on the nature of the material (see section 4.2.1) and varies along the $x$ axis. Hence, to ease the calculations, it was assumed that the generation function was a Gaussian, defined by its amplitude and FWHM,

at all $x$ values. Figure 4.6 shows the convolution of $D(x) \otimes g(x)$ when the electron beam is moved over the layer 2. It is clear that all the luminescence is coming from this layer. It can be mentioned that the broadening of the convolution peak highly depends on the standard deviation and increases with the FWHM of $g_b(x)$.
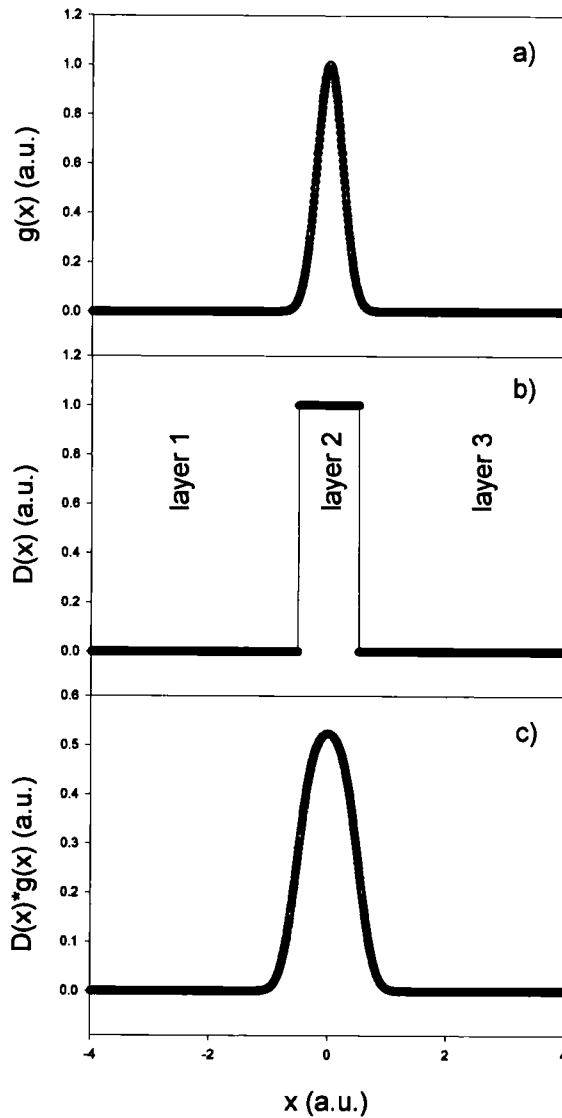


**Figure 4.6:** **Convolution of** $D(x) \otimes g(x)$**, when the incident beam is injected into the centre of layer 2.**

However, as it was explained in section 4.2, the simple convolution can be only applied if the generation function is known for all positions of the electron beam across the multi-layered system. Hence in this work it

was assumed that the function *g(x)* is a Gaussian function which is the same in all layers. This is unrealistic. Therefore, further work based on the methods developed by Rechid et al. [11] are necessary to quantify the widths of CL signals in layered systems.

### 4.6.4 Conclusions of image width simulations

In this section, the use of convolution methods in describing the contribution to the width of STEM-CL images from a) the electron beam width and b) secondary luminescence caused by X-rays which are themselves generated by the electron beam, have been described.

Boyall et al. [10] have also reported CL image width of a 2.5 nm quantum well and found broader image with discontinuities with 0.1 μm visible features.

In the next section, it will be shown that noise was a serious concern and that full calculations of image width became less of priority once this was recognised.

## 4.7 Image contrast

### 4.7.1 Experiment

As part of the system calibration process it was necessary to measure the image quality of the cathodoluminescence images. Hence, to investigate the signal quality, which can be expressed by the signal-to-noise ratio $S/N$, a simple experiment was performed in which the CL intensity from a specimen (i.e. the signal) and the hole count (i.e. the noise) were measured as shown Figure 4.7. CL signals were recorded for magnifications varying from 300 to 300,000 with different test specimens including a CdS sample grown by MOCVD and a gold ring. CL signal records are shown in Figures 4.8 and 4.9. On each record, the maxima correspond to the signal

originating from the specimen or the Au ring, whereas the minima correspond to the hole count.
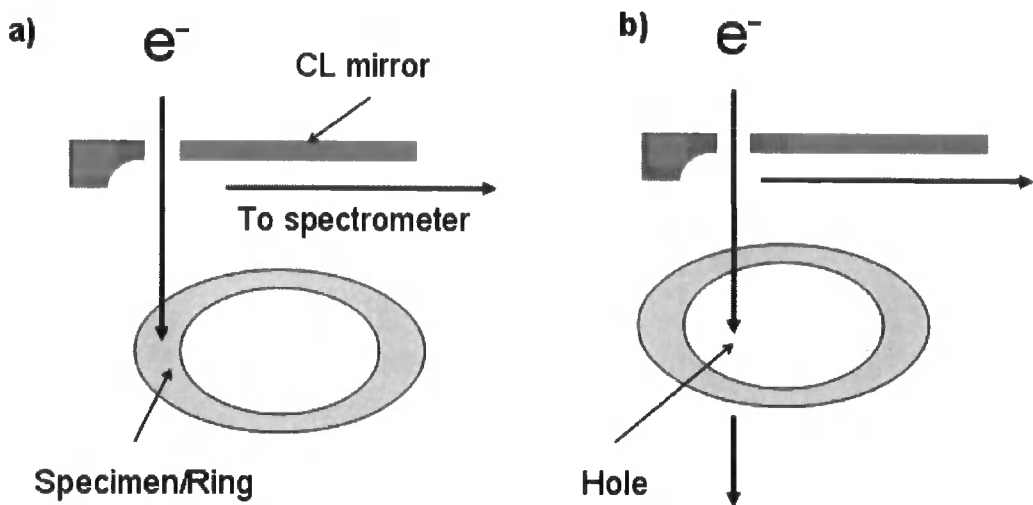


**Figure 4.7:** a) CdS Specimen or Au ring surface directly below the electron beam, (b) beam passes through a small hole in the specimen.
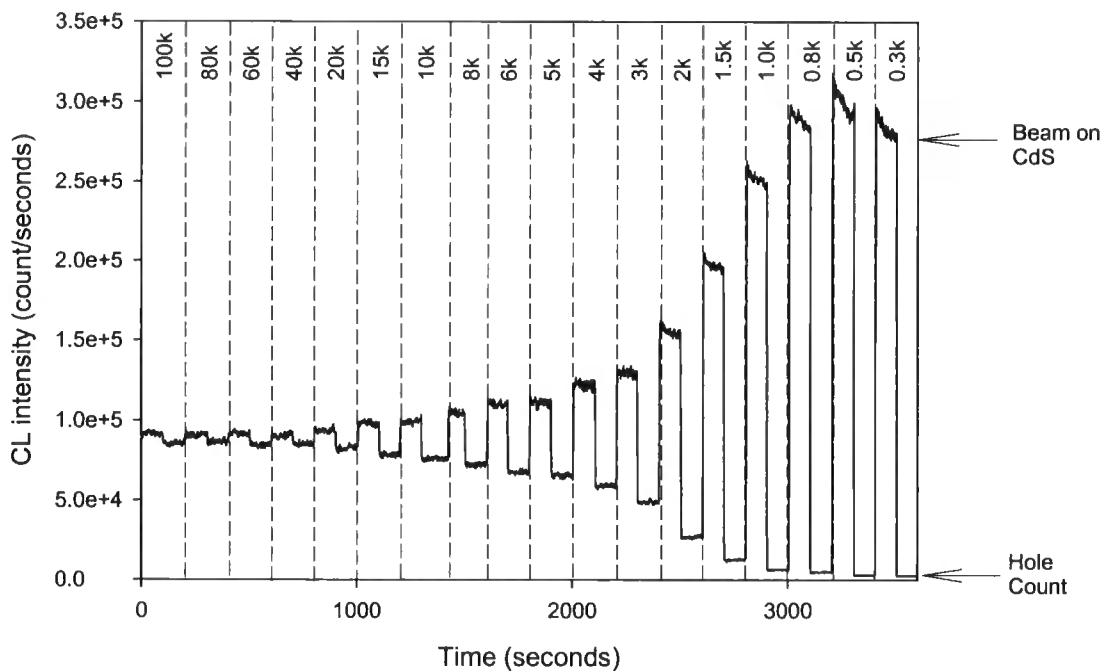


**Figure 4.8:** CL intensity vs time taken at room temperature at 120keV. The upper and lower branches correspond to the beam being positioned on the specimen and hole respectively. The labels indicate the magnification at which the CL data was taken.
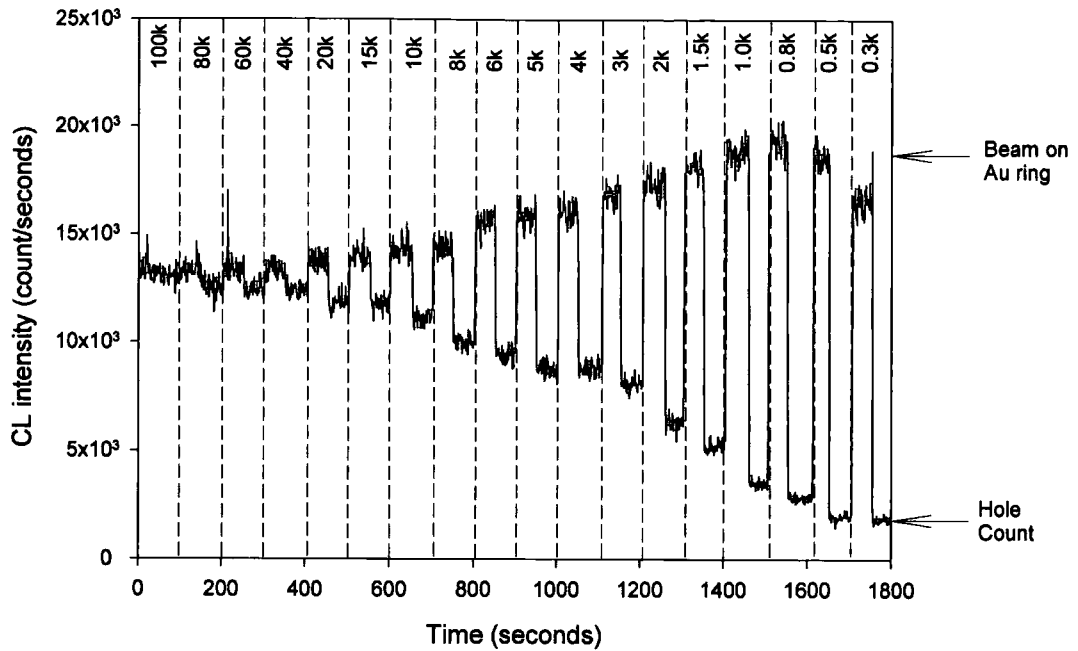
**Figure 4.9:** CL intensity vs. time taken at room temperature at 120keV. The upper and lower branches correspond to the beam being on the gold ring and hole respectively. The labels indicate the magnification at which the CL data was taken.

## 4.7.2 Discussion

In general, as the magnification decreases the CL signal from the specimen increases whereas the noise decreases. It is therefore clear that the signal-to-noise ratio $S/N$ increases with a decrease in magnification as shown in Figure 4.10. It is also noticeable that the $S/N$ depends strongly upon the nature of the specimen, especially at low magnification. As expected the CL signal generated by the CdS film is more luminescent than that from the gold ring. However, for magnifications of higher than 3000 the S/N remained lower than 5 and tended to a value of 1.0 at higher magnifications.
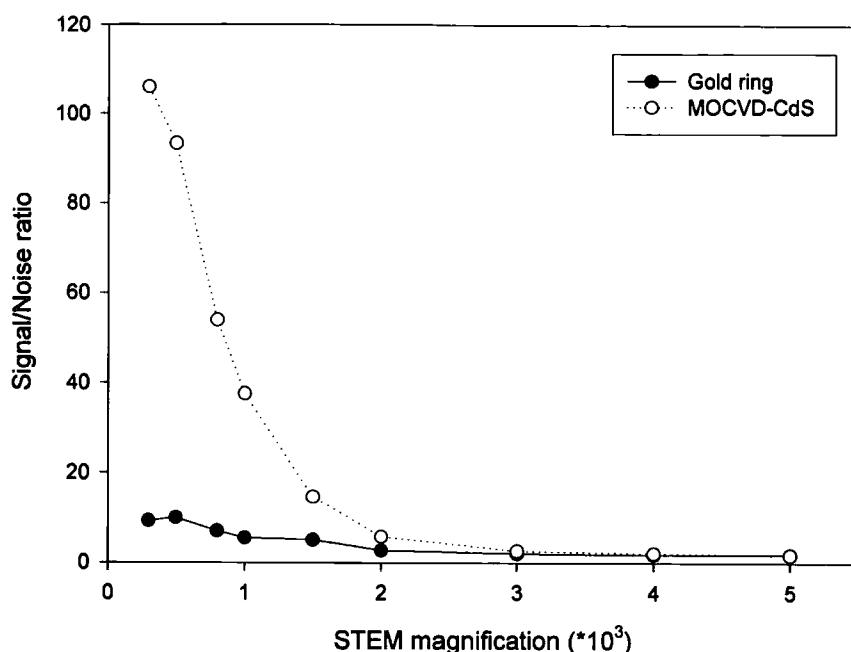
**Figure 4.10: Signal/noise ratio vs. STEM magnification for two different materials.**

From Figure 4.8, it was observed that the CL originating from the CdS decreases with increasing magnification. This can be explained due to the fact that the CL intensity is proportional to the area of scan. At larger magnifications, the area scanned is smaller and so there is less signal (i.e. The small excitation area in TEM-CL results in a small CL signal).

Similarities were found when the beam was on the gold as shown in Figure 4.9. However, the origin of this luminescence could be due to the high reflection index of the gold (since gold has no intrinsic CL emission) and/or to the X-rays from the gold exciting luminescence from the window in the CL optics.

For both spectra, the hole count increased with increasing magnification. This could be ascribed to the proximity of electron beam and CdS specimen/gold ring edge when scanning the hole at high magnification as shown in Figure 4.11a. At high magnification the electrons may strike the specimen or ring edge, then undergo energy losses due to interaction with the solid and generate luminescence. While at low magnification, the

area of the hole is much larger than at high magnification and allow the electron beam to pass whilst leaving no reflective surface area directly below the hole in the CL collection mirror, as shown in the Figure 4.11b. A simple experiment could be done to check this assumption, by measuring the hole count when the electron beam is positioned at the centre of the hole (i.e. the furthest from the specimen/ring edge). This was not attempted in the present work. This increase of noise with magnification could be also due to the instrument's electro-optical performance and the contrast produced by the specimen/detector system.
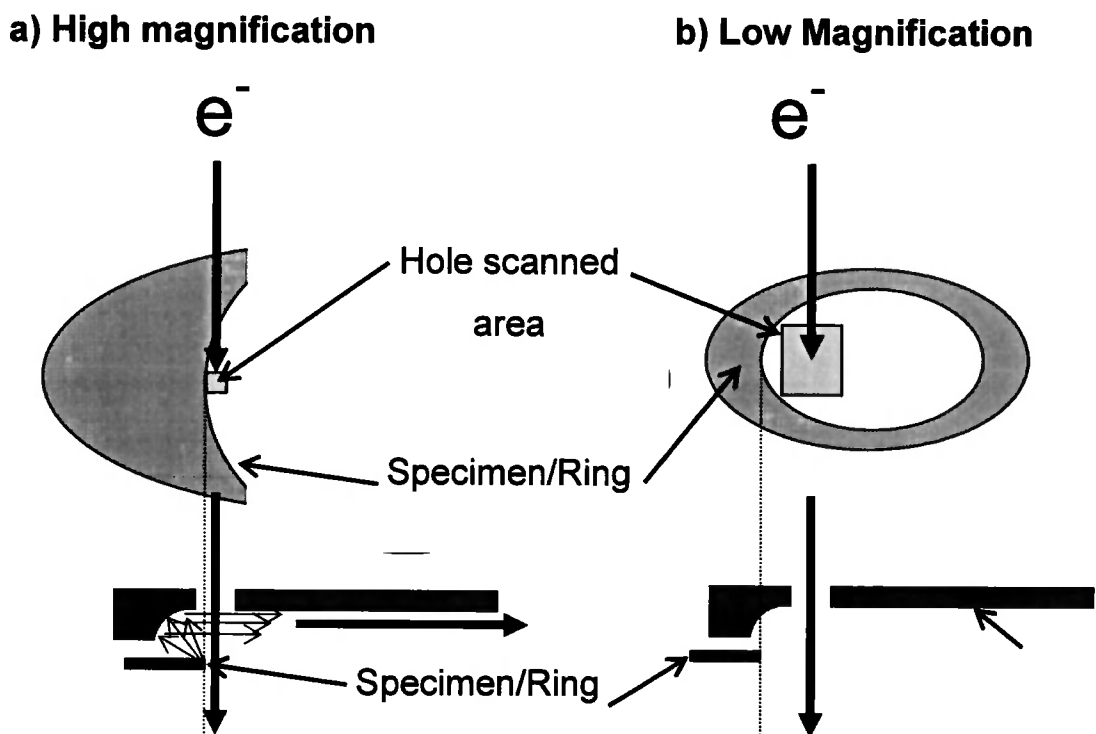


**Figure 4.11: Relative position of the electron beam to the CdS Specimen or Au ring surface when STEM-CL operates at high (a) and at low (b) magnification.**

The practical implication of this instrumental limitation is that it could limit the investigation of CL of microstructural defects such as dislocations for example. These require both working at high magnification and to obey the Rose visibility criterion [12, 13]. For the average observer to discern the difference between two points, the change in the signal due to the contrast, $\Delta S$, had to exceed the noise $N$, by a factor of 5:

$\Delta S > 5N$         (Rose criterion)          Eq. 4.19

Here the Rose criterion for image contrast visibility in a scanning microscope was used: it states that for an image feature to be visible, the signal difference between a bright and a dark feature ($S_{max} - S$) should exceed five times the noise. The noise itself is the root of the number of counts i.e. $(S_{max})^{1/2}$. Both signal and noise are therefore dependent upon the beam current ($I$), the pixel dwell time ($t$), and $q$, the efficiency of the emission process (photons per incident electron) combined with that of the spectrometry/detection apparatus. The minimum (i.e. critical) beam current ($I_c$) required to image a feature with a given contrast $C = \dfrac{S_{max} - S}{S_{max}}$ (Eq. 4.20), may be expressed [13] as:

$$I_c \approx \frac{5e}{Ctq} \, , \qquad\qquad\qquad \text{Eq. 4.21}$$

where $e$ is the electronic charge.

It can be seen from this equation that for a given detection system, there is a minimum beam current required to observe a particular contrast level, and that this current increases as the frame scan time decreases.

Further investigations are required to define the exact origin of noise especially when STEM is operating at high magnification. By either increasing the electron beam current or decreasing the frame scan time, it should be possible to enhance the image contrast, but with the present experimental arrangement STEM-CL imaging at magnifications greater than 3000 will be significantly limited by noise.

# 4.8 Conclusions of Image Contrast

The image contrast has been investigated by measuring the signal-to-noise ratio, it was found to be too low when STEM was operating at high magnifications. It also showed some limitations for acquiring CL images since the Rose criterion for image contrast visibility was not respected at high magnifications. The increase of noise with magnification has been determined by: - the proximity of electron beam positioned on a hole and the specimen, the instrument's electro-optical performance and the luminescence generated by X-rays. The origin of the noise is still unclear however studies based on the Rose visibility criterion should be carried out in the future.

# 4.9 References

1. B. G. Yacobi and D. B. Holt, *Cathodoluminescence Microscopy of Inorganic Solids.* (1990) Plenum Press
2. K. Kanaya and S. Okayama, *Penetration and energy loss-theory of electrons in solid targets,* J. Phys. D: Apllied Phys. **5** (1972)
3. B. G. Yacobi and D. B. Holt, *Cathodoluminescence scanning electron microscopy of semiconductors,* J. Appl. Phys. **59** (1986) R1-R24
4. V. I. Petrov, *Cathodoluminescence microscopy,* Physics - Uspekhi **39** (1996) 807-818
5. S. J. Pennycook, *Studies of Cathodoluminescence on a Scanning Transmission Electron Microscope,* (1978), University of Cambridge
6. D. C. Joy, *Monte Carlo Modeling for Electron Microscopy and Microanalysis.* (1995) Oxford Univeristy Press, Inc.
7. E. Napchan, *MC-SET,* (2003) DLM Enterprises
8. *http://www-cxro.lbl.gov/optical_constants/atten2.html,*
9. *International tables for X-ray crystallography.* (1952) published for the International Union of Crystallography by the Kynoch Press,
10. N. M. Boyall, *Combined TEM-Cathodoluminescence study of nitride semiconductor structures,* (2003), University of Durham
11. J. Rechid, A. Kampmann, and R. Reineke-Koch, *Characterising superstrate CIS solar cells with electron beam induced current,* Thin Solid Films **361-362** (2000) 198-202
12. J. I. Goldstein, D. E. Newbury, P. Echlin, D. C. Joy, C. Fiori, and E. Lifshin, *Scanning electron microscopy and X-ray microanalysis.* (1981) Plenum,
13. P. J. Goodhew and F. J. Humphreys, *Electron microscopy and analysis.* 2nd edition (1988) Taylor & Francis

# Chapter 5

# Single Crystal CdS

## 5.1 Introduction

In this chapter, a preliminary study of CdS using a combined transmission electron microscope (TEM) and cathodoluminescence (CL) apparatus is described. This method [1, 2] offers the possibility to investigate spectra and CL images from electron transparent semiconductor samples. Diffraction contrast and CL imaging of the same area might therefore allow correlation of spectral features with particular microstructural defects [3]. The influence of ion beam milling (used in the preparation of thin foils for TEM) on the photoluminescence and CL spectral features of CdS are described. Conditions for the electron beam imaging of CdS with minimum beam degradation of the CL emission were established. CL images of thin CdS samples containing dislocations are reported. The reader is referred to section 3.2.1 to view the details of the CdS crystal growth, which was done by Dr A. Szczerbakow at the Polish Academy of Sciences using the Piper-Polich method [4].

# 5.2 TEM-CL Calibration

## 5.2.1 Calibration of the Spectrometer

The TEM-CL apparatus is described in the section 3.5. The spectrometer wavelength calibration was performed using a cadmium spectral lamp. This was performed in-situ by bringing the microscope column up to air, positioning the lamp close to a removable part in the column and inserting the CL mirror with no specimen holder present. The spectrometer calibration was obtained by fitting the spectrum for the two separated 150 lines/mm gratings blazed for maximum reflectance at 300 nm and at 500 nm: it was decided to use a custom monochromator calibration rather than the manufacturer's nominal calibration to calibrate the wavelength. Figure 5.1 shows the spectrometer calibration data for a 150 lines/mm grating blazed at 300 nm.
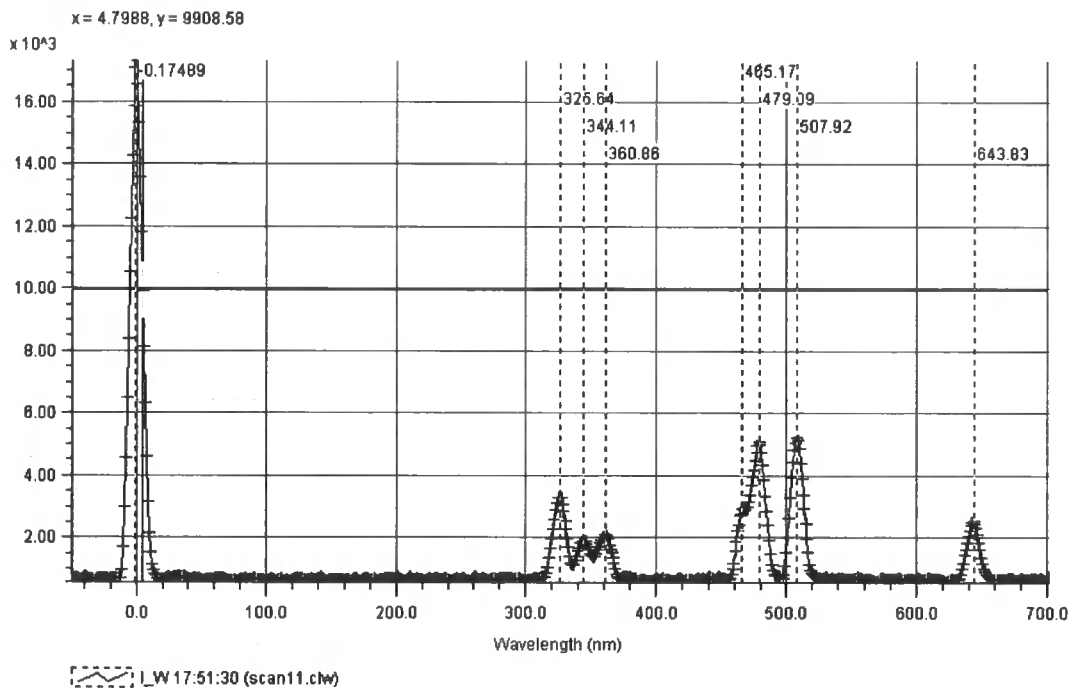


**Figure 5.1:** **Cadmium spectral emissions lines for 150 lines/mm grating blazed at 300nm.**

Furthermore, it was worth checking the calibration by detecting the zero order reflection prior to cathodoluminescence spectral measurements.

To do this, the zero order reflection could be detected without any external source, by exciting luminescence from an unused section of the specimen. If any displacement of the zero order occurred, then it was necessary to change the calibration settings defined previously in the custom calibration.

## 5.2.2 Image Calibration

CL Imaging and Line-Scans in panchromatic and monochromatic mode were described previously in section 3.5.1.2. To optimise the image contrast there are two options: a) expand the output range and/or b) alter the dynamic range of the Oxford Instruments Autobeam signal inputs settings (such as the gain and the offset). By altering these parameters it was possible to obtain a reasonably representative image on screen. The enhancement of the image was possible by varying the gain and the offset in STEM images and CL images.

In order to correlate CTEM and STEM images it was necessary to define the relationship between these two images. Hence CTEM and STEM were performed on a sample of molybdenum oxide crystals to investigate the correlation between these two. By superimposing the negative and the STEM image obtained from the *LINK ISIS* control system, it was found that both images can be only correlated if the CTEM image is rotated by ~29° (anticlockwise) and that the aspect ratio of the STEM image is changed (72.2 % in height and 51.1 % in width). Figure 5.2 shows the comparison between CTEM and STEM images.
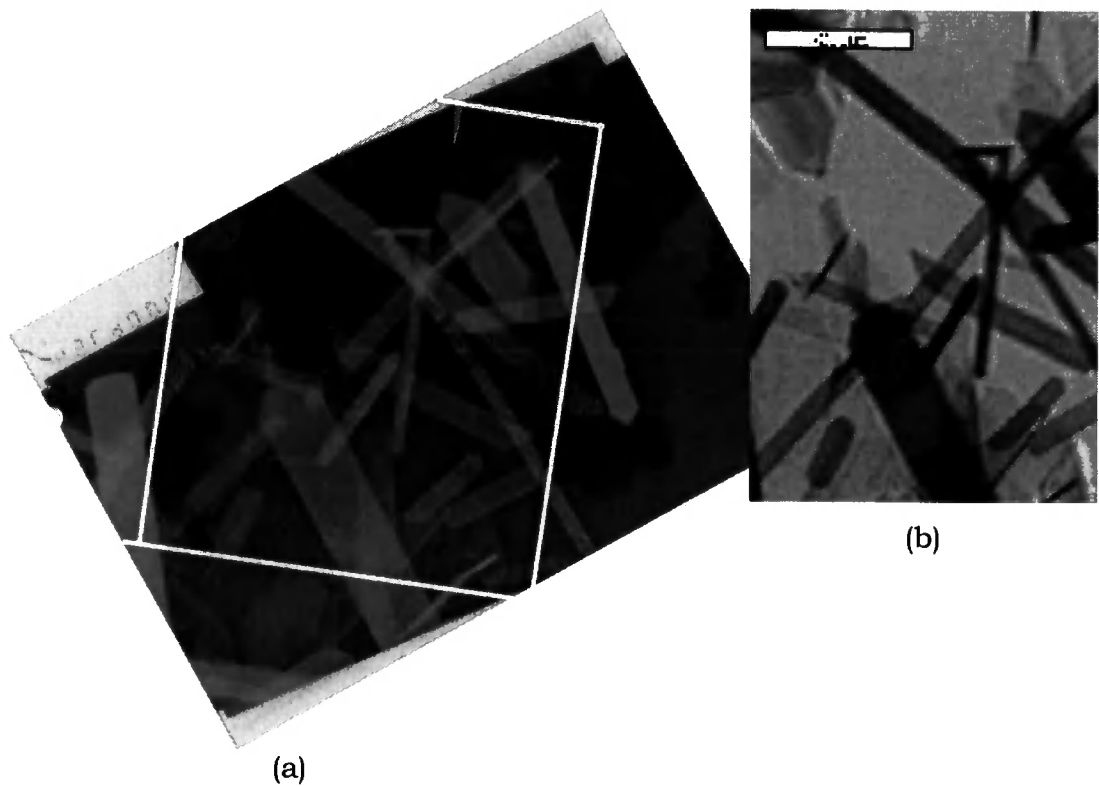
**Figure 5.2:** CTEM (a) and STEM (b) images of molybdenum oxide crystals. In CTEM the rectangular section represents the area comparable with STEM image. The STEM aspect ratio has been modified to match CTEM image.

The image rotation angle will be a function of CTEM magnification: hence the magnification used was of 100,000.

# 5.3 Luminescence Spectroscopy

The CdS crystals had a yellow-green tint characteristic of their being grown under Cd-rich conditions. Figure 5.3 shows PL spectra recorded from samples that were a) in their as-sawn state, b) $Ar^+$ thinned and c) thinned with $Ar^+$ and then finished with $I^+$ ion milling. While there are many reports of the origin of the PL from CdS, here we use the notation reported by Agata [5]. There are two green bands 'G1' (2.54eV, 488nm) and 'G2' (2.37eV, 522nm), the former being considered to be due to near band edge processes. The broader yellow 'Y' (2.08eV, 594nm) and the red 'R' (1.69eV, 734nm) bands are usually attributed to Cd interstitials and S vacancies respectively [5, 6].

The spectrum of the sawn sample (Figure 5.3) shows a weak but distinct G1 peak that is absent from the spectra of the ion milled samples. This absence is purely an instrumental effect, the former spectrum being taken with a 495 nm long pass filter: CL spectra (Figure 5.4) confirm that near band edge emission (G1) occurs in the ion beam milled samples. The most striking difference between PL spectra from the ion milled samples and that of the sawn surface, is the enhancement of the Y band with ion milling. Since the Y band is ascribed to Cd interstitials (and sometimes to Cd vacancies), the enhancement of this band by ion milling might be seen as tentative evidence for Cd displacement. The reduction of the intensity of the red band (R) upon $I^+$ ion beam finishing may be due to either to the elimination of stacking fault loops (present from $Ar^+$ damage) and/or $I^+$ ion implantation.
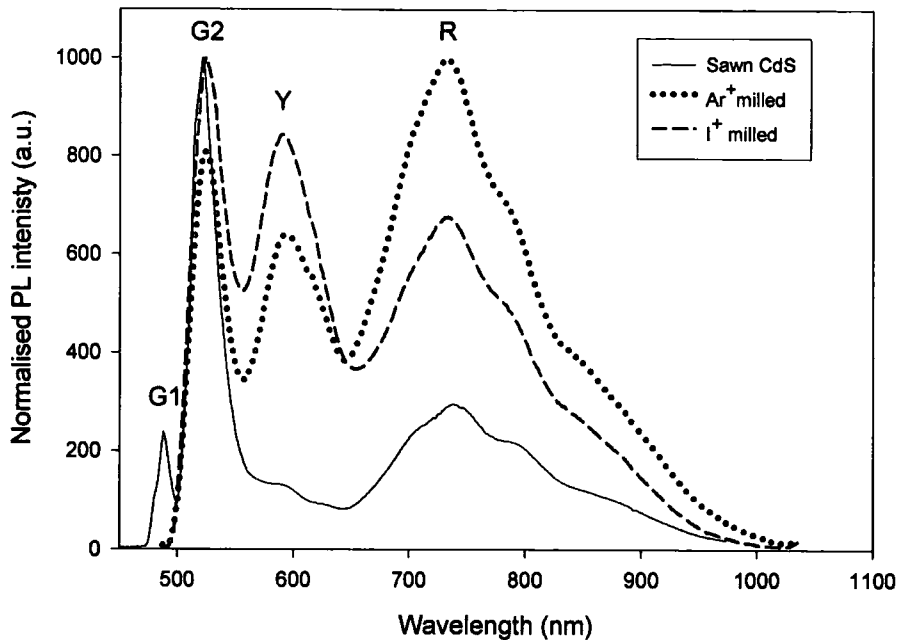
**Figure 5.3:** **4K PL spectra of CdS a) from a sawn surface (solid line), b) Ar⁺ ion milled surface (dotted line) and c) I⁺ ion milled surface (dashed line). The bands are described in the text. For spectra b) and c) the near band edge line G1 was attenuated by a long pass filter ($\lambda$=495 nm) used to remove the laser line. A notch filter was used for a) and so the G1 line is present.**

Figure 5.4 shows 100K CL spectra (200kV) from both Ar⁺ and I⁺ finished CdS discs in the TEM. The most notable difference from the PL spectra is that for both CL spectra the red band (R) is absent. This cannot be attributed to the instrument response since the PMT and spectrometer are known to have a good detectivity and transmission between 650 and 800nm. However, it is possible that the difference in the excitation density between PL and CL influences the spectra. For the PL, the beam power at the sample was 10mW focused to a 1 mm spot, whereas in the CL experiment at 200kV a beam current of $4\times10^{-8}$ A was focused to a 2 μm spot. The areal excitation density in this CL experiment was approximately 7 orders of magnitude greater than in the PL. Schmidt et al. [7] reports models accounting for the variation of luminescence with laser excitation density for PL over 3-4 orders of magnitude. The models are based on the kinetic response of different luminescence mechanisms, with some mechanisms (lines) being favoured over others. Given the extreme difference in excitation density between PL and CL, it may be the case that

the deep red luminescence is quenched. Also the sample temperature difference, and the fact that the samples used for TEM-CL were thin, may play a role.
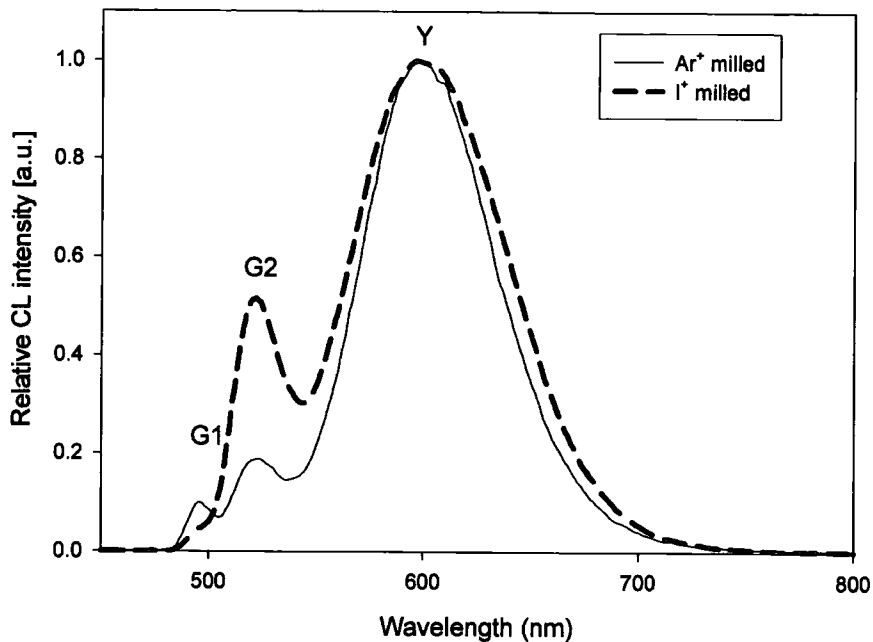


**Figure 5.4:** 200kV CL spectra of CdS recorded in the TEM at 100K, a) Ar+ ion milled (solid line), b) I+ ion milled (dotted line). Differences between these and the PL spectra shown in Fig. 5.3 are discussed in the text.

# 5.4 Electron Beam Degradation

A fraction of the electron beam energy deposited in a semiconductor will be converted into cathodoluminescence through the radiative recombination of electron-hole pairs. It has been shown that the injected density of electron-hole pairs in a semiconductor can influence luminescent properties [6, 7]. To investigate the free carrier generation rate in TEM-CL experiments, beam current and beam degradation measurements have been analysed in the following sections.

## 5.4.1 Beam Current Measurements

Beam current measurements for the *JEOL 200CX* TEM taken with a Faraday cup in STEM and CTEM modes are shown in Table 5.1. In each instance the filament current was set to saturation before inserting the Faraday cup. Beam current values vary with the position of the tip of the tungsten filament in relation to the top of the Wehnelt cylinder so beam current measurements were repeated as needed. The electron flux density is calculated based upon a STEM beam diameter of 10nm and a CTEM beam diameter which was measured directly from the screen graticule.

From Table 5.1, the electron flux density in CTEM mode is approximately three orders of magnitude higher than in STEM mode.

| Accelerating Voltage | Condenser Aperture | STEM mode | | | CTEM mode | | |
|---|---|---|---|---|---|---|---|
| | | $I_{beam}$ (A) | Area$_{beam}$ (m$^2$) | e$^-$.cm$^{-2}$.s$^{-1}$ | $I_{beam}$ (A) | Area$_{beam}$ (m$^2$) | e$^-$.cm$^{-2}$.s$^{-1}$ |
| 40kV | 4 | – | 7.9E-15 | – | 1.7E-11 | – | – |
| | 3 | 3.0E-12 | 7.9E-15 | 2.4E+17 | 3.8E-10 | – | – |
| | 1 | 2.1E-11 | 7.9E-15 | 1.7E+18 | 3.6E-09 | – | – |
| 80kV | 4 | – | 7.9E-15 | – | 2.9E-11 | 7.1E-16 | 2.6E+19 |
| | 3 | 5.0E-12 | 7.9E-15 | 4.0E+17 | 6.8E-10 | 1.8E-16 | 2.4E+21 |
| | 1 | 4.7E-11 | 7.9E-15 | 3.7E+18 | 6.2E-09 | 4.9E-16 | 7.8E+21 |
| 100kV | 4 | – | 7.9E-15 | – | 9.6E-11 | 1.4E-15 | 4.2E+19 |
| | 3 | 1.3E-11 | 7.9E-15 | 1.0E+18 | 2.2E-09 | 4.9E-16 | 2.9E+21 |
| | 1 | 1.1E-10 | 7.9E-15 | 8.8E+18 | 2.1E-08 | 9.6E-16 | 1.3E+22 |
| 120kV | 4 | – | 7.9E-15 | – | 1.2E-10 | 2.6E-15 | 3.0E+19 |
| | 3 | 1.7E-11 | 7.9E-15 | 1.4E+18 | 2.9E-09 | 8.3E-16 | 2.2E+21 |
| | 1 | 1.5E-10 | 7.9E-15 | 1.2E+19 | 2.6E-08 | 2.0E-15 | 8.4E+21 |
| 160kV | 4 | – | 7.9E-15 | – | 3.7E-10 | 4.1E-15 | 5.6E+19 |
| | 3 | 3.9E-11 | 7.9E-15 | 3.1E+18 | 8.7E-09 | 1.6E-15 | 3.4E+21 |
| | 1 | 3.4E-10 | 7.9E-15 | 2.7E+19 | 7.9E-08 | 2.8E-15 | 1.7E+22 |
| 200kV | 4 | – | 7.9E-15 | – | 4.7E-10 | 6.4E-15 | 4.6E+19 |
| | 3 | 5.2E-11 | 7.9E-15 | 4.2E+18 | 1.1E-08 | 3.1E-15 | 2.2E+21 |
| | 1 | 4.7E-10 | 7.9E-15 | 3.7E+19 | 1.0E-07 | 4.4E-15 | 1.4E+22 |

**Table 5.1:** **STEM and CTEM beam currents for different beam accelerating voltages and condenser apertures in the *JEOL 200CX*. The electron flux density is calculated based upon a CTEM beam diameter of 1µm and STEM beam diameter of 10nm.**

## 5.4.2 Electron Beam Degradation

Electron beam induced degradation of CL has been observed in a number of different III-V and II-VI semiconductors during TEM-CL studies [8-15]. The observed degradation has been attributed to either the creation of non-radiative centres such as point defects, or to the destruction of luminescence centres [10]. Through a simple recombination centre model Ohno et al. [12] described the degradation and calculated a threshold electron energy for the displacement of atoms from the crystal lattice by displacement or knock-on damage [16]. In the following sections electron beam degradation data are analysed for the panchromatic CL emission from single crystal CdS.

Figure 5.5 illustrates the evolution of panchromatic CL intensity at 100K under 200kV electron beam irradiation. Illumination with both conventional TEM ($I_{beam}$ = 4×10$^{-8}$ A, focused to 2 µm diameter, giving a current density of 1.3x10$^4$ A.m$^{-2}$) and STEM (moving beam, magnification=

$2\times10^4$, $I_{beam}$ = $2\times10^{-10}$ A, giving a current density of 1.5 A.m$^{-2}$) were investigated. While there was little change in the CL response under STEM illumination over a period of 600s, significant degradation took place under CTEM illumination in the same time. Curves were recorded under CTEM illumination for 80, 100, 120,160 and 200kV. Ohno et al. [13] fitted similar TEM-CL degradation curves for (Ga,In)P to the function:

$$I(t) = \frac{1}{1 + \theta D}$$

Eq. 5.1

where $D$ is the dose in electrons per cm$^2$. The model invoked a constant number of radiative centres $N_{rr}$ having cross section $\sigma_{rr}$, and $i$ types of non-radiative centres of cross section $\sigma_{nr(i)}$ which increased in number with electron dose at a rate $\varepsilon_{nr(i)}$. $\theta$ is therefore defined as:

$$\theta = \frac{\sum_i \sigma_{nr}(i)\varepsilon_i}{N_{rr}\sigma_{rr}} \quad (cm^2)$$

Eq. 5.2

Fitting of the CTEM degradation curves to Ohno's function gave values of $\theta$ in the range $1.4\times10^{-22}$ to $5.4\times10^{-23}$ cm$^2$. These values are 2-3 orders of magnitude lower than those reported for GaN ($1.3\times10^{-20}$ to $2.6\times10^{-21}$ cm$^2$) [8] and for (In,Ga)P ($5\times10^{-20}$ to $4.5\times10^{-19}$ cm$^2$) [13]. Since the value of $\theta$ is specific to the material, this may indicate that CdS is more resistant to beam damage than these other materials. Beam damage is considered to be a threshold effect and so examination of the variation of $\theta$ with accelerating voltage may be expected to reveal the energy for the onset of significant damage processes. However, for the present data the $\theta$ values did not follow a regular series, and no threshold was observed. This may be due to experimental effects including: a) the stability of the electron beam, and b) variation in CL degradation rate with position on the sample: it was observed qualitatively that thinner areas of the TEM foil degraded more quickly under CTEM illumination than did thicker areas. The role of the surfaces in electron beam degradation is a topic for further investigation.
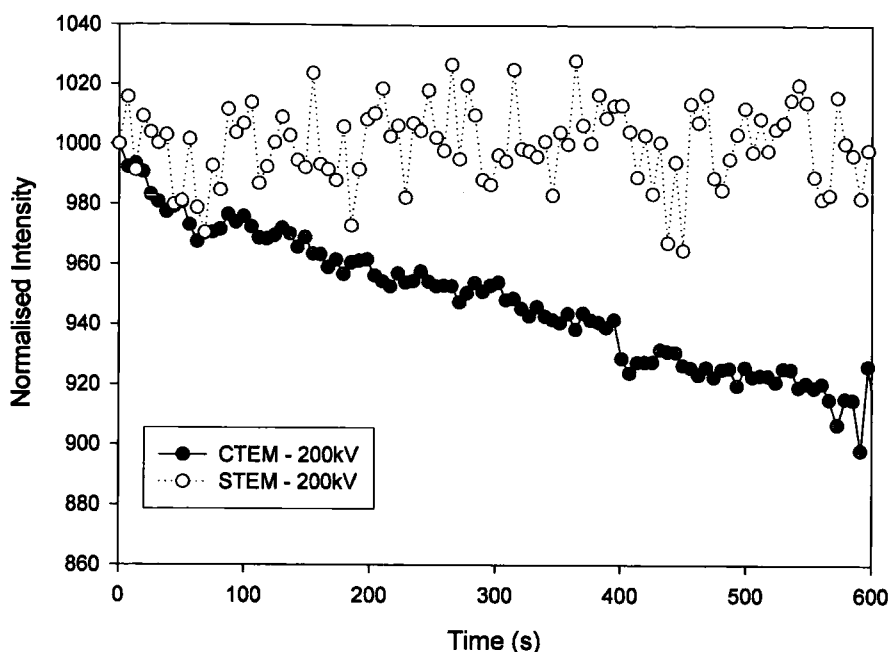
**Figure 5.5:** **Evolution of the panchromatic CL under 200kV beam irradiation excited from I⁺ ion thinned CdS with time at 100K, a) conventional TEM illumination and b) STEM illumination.**

For the beam excitations used in this work it was demonstrated that the degradation rate of CL from CdS was significantly greater under CTEM illumination than under STEM illumination. This can be directly attributed to the higher current density used in CTEM, it being 3 orders of magnitude greater than in STEM in this case (see above). Generally it was found that meaningful CL signals could only be extracted from relatively thick regions of the specimen. However, CTEM diffraction contrast imaging of these areas often required a highly focussed condenser lens (small illumination area) that has been demonstrated to accelerate beam damage (as shown in Figure 5.5). The practical procedure to acquire information from a sample whilst incurring minimal beam damage was therefore to firstly record CL maps in STEM mode, and thereafter to record CL spectra, diffraction contrast images in CTEM mode, and to undertake any prolonged STEM imaging.

# 5.5 CL imaging

Figure 5.6 (a, b and c) compares CTEM, STEM and STEM-CL images of an Ar⁺/I⁺ thinned CdS specimen obtained at 160kV at a temperature of 100K. Area '1' is the vacuum, while areas '2' and '3' are electron transparent and thick regions respectively (the sample is not uniformly thick). The TEM image in Fig 5.6a and 5.7 show a number of dislocations. While the sample is relatively thick (necessary for STEM-CL imaging), a dislocation may be seen running from just below '3' to a node above and to the left of '2'. From the node, dislocations run above and below '2'. The dislocations lie approximately in the (0001) plane, but since the sample was thick, two-beam analysis of the dislocations was not performed. The CTEM image in Figure 5.6a has been rotated and scaled for ease of comparison with the STEM and STEM-CL images of Figures 5.6b and c (see section 5.2.2). Nevertheless, since Figures 5.6b and c were recorded with zero tilt (because the CL mirror was in place) and the CTEM image in Figure 5.6a was tilted to give a diffraction vector of $g = [\bar{2}110]$, there is therefore some slight distortion of the CTEM compared to the other two images. The coarse contrast features in the STEM and CL images (Figure 5.6b and c) are thickness related, with, for example, the thin area '2' being bright in STEM and dark in CL, and the converse being true of area '3' (the apparent position of the sample edge is a function of the gain and contrast settings for the images). As is normal for STEM images, the dislocation contrast is relatively weak compared to that in CTEM for which a two-beam case has been selected. The forking dislocation structure running from '3' and either side of '2' is therefore represented by contrast in Figure 5.6b, albeit weak. Weak and diffuse dark contrast can also be seen at the same positions in the CL image (Figure 5.6c). It is this correspondence of contrast features that indicates that the TEM-CL method is capable of resolving individual dislocations in CdS. As the contrast features are dark in CL, the contrast mechanism is recombinative. It should be pointed out that both the STEM and the STEM-CL image contrast was weak, and was difficult to reproduce graphically even after image enhancement was applied. The limits of image contrast for the STEM-CL method are now explored.
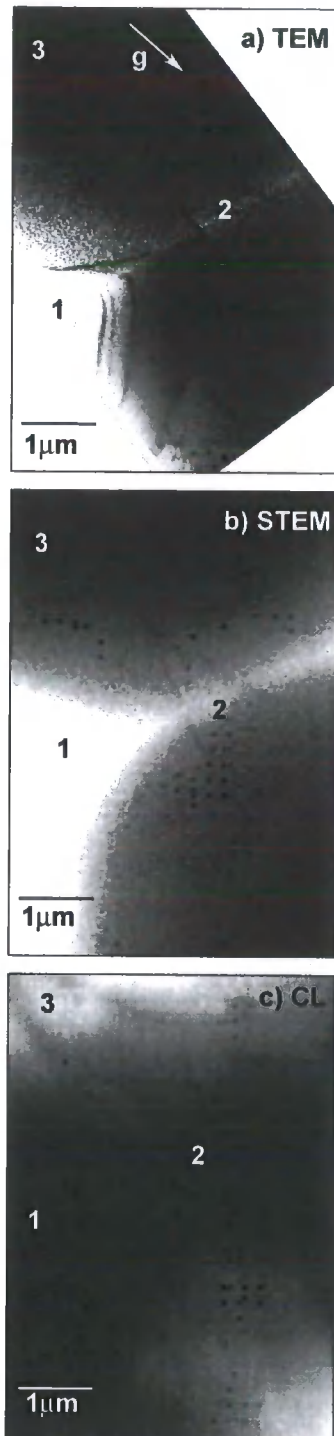
**Figure 5.6:** 160kV imaging at 100 K of Ar⁺/I⁺ thinned CdS, a) TEM image, g = [$\bar{2}$110], B = [0001], b) STEM image, and c) panchromatic CL image. Area (1) is the vacuum. In area (2) the sample is electron transparent while in the area (3) it is thick. Contrast from dislocations runs from just below '3' and forks either side of '2' in each of the images.

A quantitative assessment of the visibility of features seen in STEM-CL images was made - and their relationship to the signal and noise levels together with the efficiency of the luminescence process evaluated. Here the Rose criterion [17, 18] for image contrast visibility in a scanning microscope was used (see section 4.7.2). For STEM in the system used, a dwell time of $t = 0.0128$ s and a beam current of $10^{-10}$ A were typical, giving a photon count rate of $3 \times 10^4$ s$^{-1}$. The emission/collection efficiency was therefore given by $q = 3 \times 10^4 \times \dfrac{e}{10^{-10}} = 4.8 \times 10^{-5}$ photons per electron. These values yield $I_c \approx 3 \times 10^{-11}$A as the lower limit of beam current necessary to give 5% contrast (i.e. $C = 0.05$). Therefore the imaging conditions available with this apparatus are close to the limit necessary for feature visibility in STEM-CL imaging. Nevertheless, dislocation images can be recorded in STEM-CL, not only in these CdS samples, but in for example GaN [3, 8]. It is therefore possible that optimisation of the imaging conditions shall yield improved results. Factors to be adjusted include beam current, sample temperature, collection efficiency and the pixel dwell time.

# 5.6 Analysis defect images in TEM

By enhancing the contrast and the brightness of Figure 5.6a, Figure 5.7 was obtained and revealed clearly the presence of both isolated dislocations and of dislocation networks.
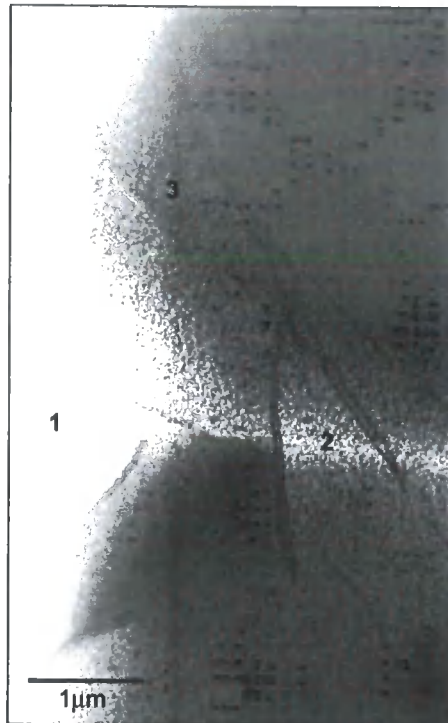
**Figure 5.7:** **TEM of the same area as Figure 5.6a, but the brightness and contrast of image have been enhanced to see clearly the node of dislocations.**

Two-beam condition studies could not have been applied on this area due to the fact the limited rotation and tilting of the sample because of its proximity with the CL mirror. Two-beam condition is usually used to define the nature and the Burgers vectors of the dislocation. However, other works have reported some results concerning dislocation structure and mechanism of motion in CdS [19, 20]. Maeda et al. [20] has reported the presence of edge, screw and mixed dislocations in CdS crystals.

# 5.7 Conclusion

A preliminary study of the viability of combined TEM-CL apparatus in the study of CdS for solar cell application has been presented.

Comparison of PL and CL spectra revealed that:
a) $Ar^+$ and $I^+$ ion beam thinning used in thin foil TEM specimen preparation changed the emission spectrum of the CdS: there was an increase of the yellow (Y) emission (594nm),
b) CL spectra recorded from CdS did not contain the red band (734nm) that was easily detected in PL spectra of the same samples. Its absence was tentatively attributed to the excitation density in CL, since this was 7 orders of magnitude higher than in PL.

Significant electron beam degradation of CdS during imaging could be avoided by using the STEM imaging mode to acquire CL maps prior to extensive work with higher beam current densities (e.g. CTEM imaging with a highly focussed condenser lens) being undertaken.

Linear image contrast features in STEM-CL images of CdS were correlated directly to dislocation images obtained in CTEM and STEM mode. However, the image contrast was weak in STEM-CL. Assessment of the imaging conditions using the Rose criterion [18] indicated that this CL work was done under conditions close to the limits of visibility for 5% contrast, and this accounted for the weakness of the contrast obtained. In further work, enhancement of the images contrast by optimisation of the signal excitation and handling should be undertaken. Even so, the limits to S/N described in the section 4.7 may present some serious impediments to high magnification studies that may limit the usefulness of this technique for this particular instrument combination.

# 5.8 References

1.  S. J. Pennycook, A. J. Craven, and L. M. Brown, *Cathodoluminescence on a scanning transmission electron microscope*, Inst. Phys. Conf. Ser. **36** (1977) 69-73

2.  V. I. Petrov, *Cathodoluminescence microscopy*, Physics - Uspekhi **39** (1996) 807-818

3.  M. Albrecht, H. P. Strunk, J. L. Weyher, I. Grzegory, S. Porowski, and T. Wosinski, *Carrier recombination at single dislocations in GaN measured by cathodoluminescence in a transmission electron microscope*, J. Appl. Phys. **92** (2002) 2000-2005

4.  W. W. Piper and S. J. Polich, *Vapor-Phase Growth of Single Crystals of II–VI Compounds*, J. Appl. Phys. **32** (1961) 1278

5.  M. Agata, H. Kurase, S. Hayashi, and K. Yamamoto, *Photoluminescence spectra of gas-evaporated CdS microcrystals*, Solid State Communications **76** (1990) 1061-1065

6.  M. A. Hernandez-Fenollosa, D. P. Halliday, K. Durose, M. D. Campo, and J. Beier, *Photoluminescence studies of CdS/CdTe solar cells treated with oxygen*, Thin Solid Films **431-432** (2003) 176-180

7.  T. Schmidt, K. Lischka, and W. Zulehner, *Excitation-power dependence of the near-band-edge photoluminescence of semiconductors*, Phys. Rev. B **45** (1992) 8989–8994

8.  N. M. Boyall, *Combined TEM-Cathodoluminescence Study of Nitride Semiconductor Structures*, PhD, (2003), University of Durham

9.  N. Yamamoto, *Characterization of Crystal Defects by Cathodoluminescence Detection System Combined with TEM*, Materials Transactions, JIM **31** (1990) 659-665

10. T. Mitsui, N. Yamamoto, K. Takemoto, and O. Nittono, *Cathodoluminescence and Electron Beam Irradiation Effect of Porous Silicon Studied by Transmission Electron Microscopy*, Japanese Journal of Applied Physics **33** (1994) L342-L344

11. T. Mitsui and N. Yamamoto, *Deep Level Emission in ZnS Caused by Elecron Beam Irradiation Studied by Cathodoluminescence Measurement System*, Japanese Journal of Applied Physics **37** (1998) L1390-L1392

12. Y. Ohno, Y. Kawai, and S. Takeda, *Vacancy-migration-mediated disordering in CuPt-ordered (Ga,In)P studied by in situ optical spectroscopy in a transmission electron microscope*, Physical Review B **59** (1999) 2694-2699

13. Y. Ohno and S. Takeda, *Study of Electron-Irradiation-Induced Defects in GaP by In-situ Optical Spectroscopy in a Transmission Electron Microscope.*, J. Electron Microsc **45** (1996) 73-78

14. Y. Ohno and S. Takeda, *Optical properties of anti-phase boundaries and Frenkel-type defects in CuPt-ordered GaInP studied by optical spectroscopy in a transmission electron microscope*, Inst. Phys. Conf. Ser. **164** (1999) 175-178

15. S. Achour, A. Harabi, and N. Tabet, *Catholuminescence dependence upon irradiance time*, Materials Science and Egineering **B42** (1996) 289-292

16. D. B. Williams and C. B. Carter, *Transmission Electron Microscopy - Basics.* (1996) Plenum Press

17.  J. I. Goldstein, D. E. Newbury, P. Echlin, D. C. Joy, C. Fiori, and E. Lifshin, *Scanning electron microscopy and x-ray microanalysis.* (1981) Plenum,

18.  P. J. Goodhew and F. J. Humphreys, *Electron Microscopy and Analysis.* 2nd Edition (1988) Taylor and Francis

19.  O. Vyvenko, A. Zozime, and W. Schroter, *Cathodoluminescence imaging of dislocations in CdS: a new defocused-mirror technique,* Materials Science and Engineering B **24** (1994) 105-111

20.  K. Maeda, K. Nakagawa, and S. Takeuchi, *Cathodoluminescence studies of dislocation motion in IIb-VIb compounds deformed in SEM,* Journal of materials science **16** (1981) 927-934

# CdS Thin Films

## 6.1 Introduction

The aims of this chapter are: to investigate the optical and structural properties of CdS thin films grown by chemical bath deposition and metalorganic chemical vapour deposition; to investigate the post-treatment influence of air annealing and $CdCl_2$ treatment on the CBD CdS; to investigate the effects of growth parameters in MOCVD CdS layers; and to investigate their influences on the grain size distribution.

Details of the growth of these CdS thin films are shown in section 4.2.2. Characterisation techniques used to study them including optical transmittance, photoluminescence, GIXRD and TEM are described in Chapter 3.

# 6.2 Optical Transmittance Analysis

In this section, the optical transmission of both CBD and MOCVD grown films is investigated using the methods described in section 3.2.1.

## 6.2.1 Cadmium Sulphide Grown by CBD

Transmittance measurements of three samples of CBD CdS films is given in Figure 6.1.
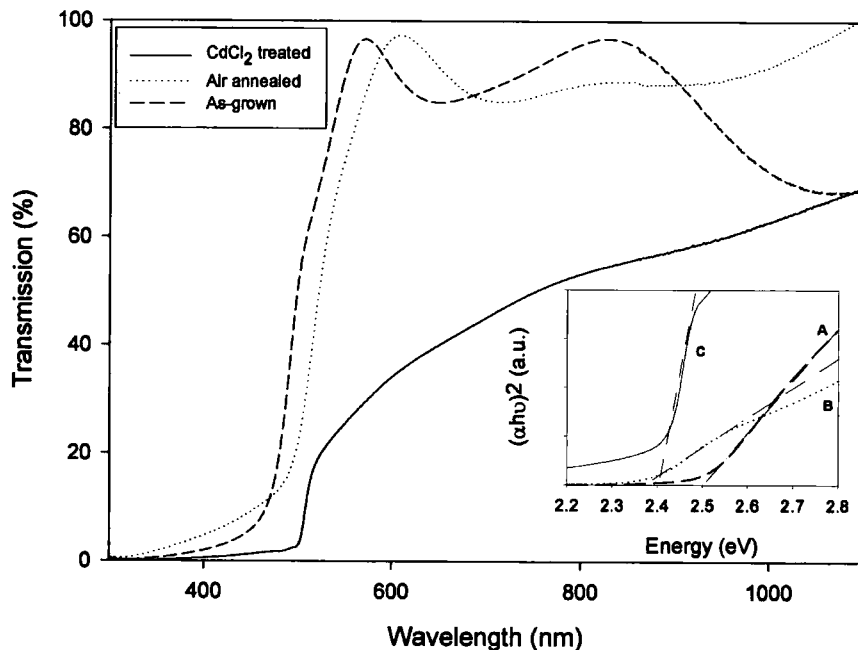


**Figure 6.1:** **Transmittance for CBD-samples; a) As-grown, b) Annealed in air at 400°C for 1 hour and c) CdCl₂ treated and annealed at 400°C for 1 hour. The inset shows (αhv)² vs energy.**

The main feature in the spectra is a shift in absorption edge towards a longer wavelength associated with both air annealing and CdCl₂ treatment. The CdCl₂ treated sample also exhibits a much lower transmission than the as-grown sample. For purposes comparison with the other films the bandgap of all three films were estimated using $(\alpha h v)^2$ vs $hv$ as described in section 3.2.1. The thin film thickness of 150 nm was measured with a TENCOR Alpha Step 200. The plots are shown in the inset

in Figure 6.1. The energy bandgaps were measured to be 2.51, 2.38 and 2.44 eV for the as-deposited, annealed and $CdCl_2$ treated samples respectively.

It is a significant result that the energy bandgap of CdS decreases with annealing in air from 2.51 to 2.38 eV. Other authors reported this effect as well [1, 2]. Annealing in different atmospheres such as $H_2$, Ar, air and sulfur is known to reduce the bandgap of CdS films [3, 4]. Some authors attribute this to the phase change from cubic to hexagonal [4, 5], although the difference of bandgap in the two phases is only 30 meV (2.48 eV for hexagonal and 2.45 eV for cubic) [6]. The phase changes therefore are unlikely to account for all of the bandgap changes observed.

Rakhshani et al. [7] has reported that annealing in air lowers the energy bandgap due to the development of grain-related states. Annealing also relaxes the lattice strain and improves the mobility-lifetime product for the photogenerated carriers.

It is also noticeable that $CdCl_2$ treated films possess a sharper onset of absorption at the bandgap, suggesting fewer defect levels manifest near the bandgap edges compared to the as-deposited and annealed samples. Similar results have been reported by [8, 9] which showed the beneficial effect of $CdCl_2$ treatment. However, in our experiment a decrease in transmittance from 80% to 50% was found and this was ascribed to absorption and reflection by residues from the $CdCl_2$ treatment.

## 6.2.2 Cadmium Sulphide Grown by MOCVD

The optical transmittance of CdS grown by MOCVD using different II/VI ratios and growth temperatures is shown in Figure 6.2.
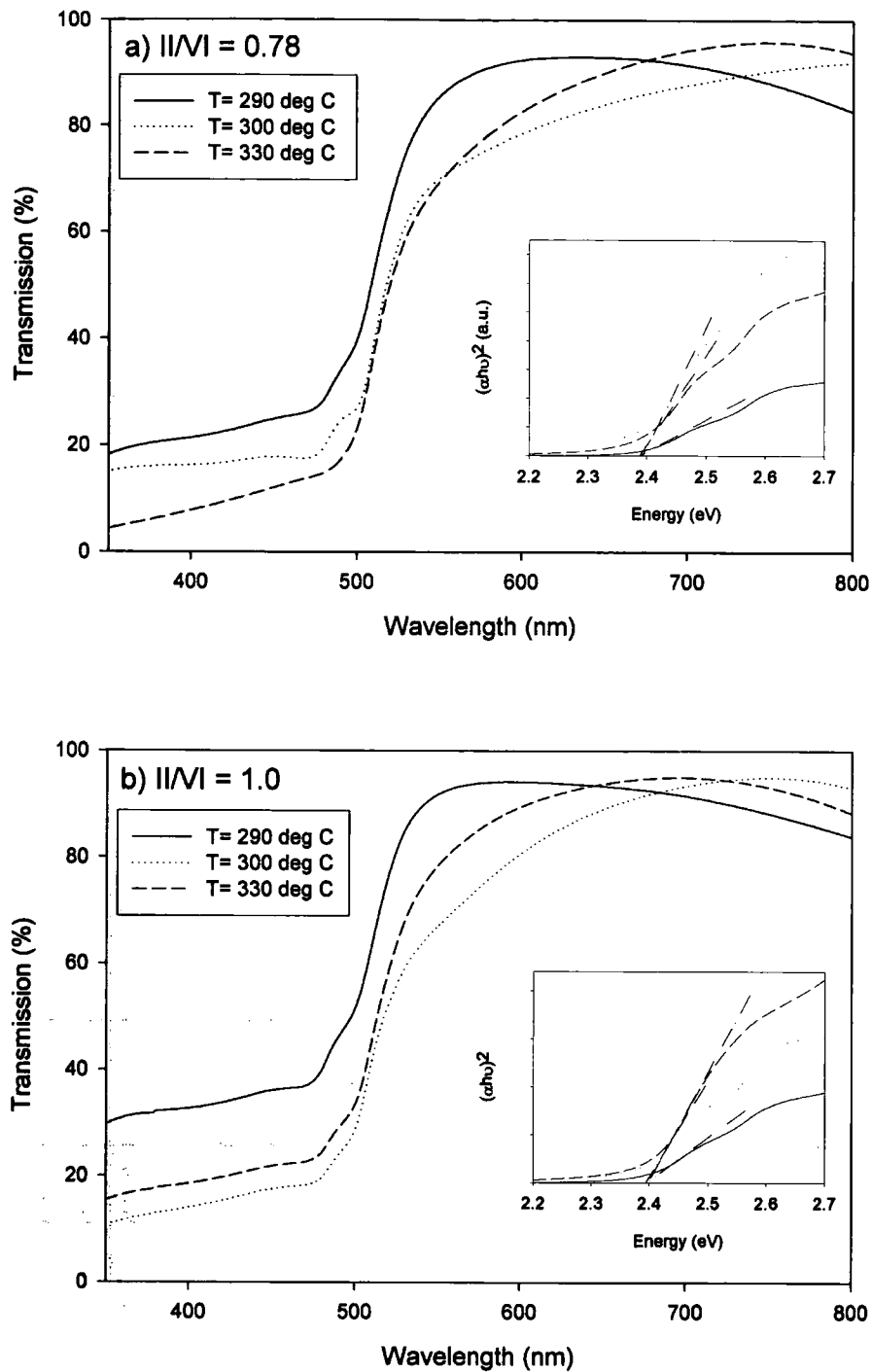
**Figure 6.2:** **Transmittance spectra of MOCVD samples deposited at temperatures of 290, 300 and 330°C for a) II/VI = 0.78 and b) II/VI = 1.0. Inset shows $(\alpha h\upsilon)^2$ versus energy.**

The absorption edges, corresponding to the CdS bandgap (approximately 520 nm), were shifted towards a lower energy upon increasing the growth temperature from 290 to 330°C. All the films

exhibited a transmittance of the order of 80% at the longer wavelength region (above the absorption edge), which may be adequate for use as window layers. The bandgaps were determined as before. It was found that the bandgap reduced from 2.41 eV for growth at 290°C to 2.40 eV for growth at 300°C, irrespective of the II/VI ratio used. Hence, it can be concluded that within the range of growth temperature and the II/VI ratio used in this study no significant changes in transmittance were observed.

# 6.3 Photoluminescence Spectroscopy Analysis

The reader is referred to section 3.2.2 for a description of photoluminescence (PL) spectroscopy.

## 6.3.1 Cadmium Sulphide Grown by CBD

Photoluminescence spectra for all three of the samples are shown in Figure 6.3. The as-deposited sample has a broad luminescence band located at 1.2-2.0 eV. This is typical for CBD grown CdS, and is referred to as the Red Band (RB). The RB is commonly ascribed to either sulfur vacancy states [10] or surface states [11]. Air annealed films exhibit a similar RB peak with slightly modified intensities for the sub-peaks, which themselves have slightly lower energies. Air annealed samples also have very weak features in the 2.1-2.3 eV region known as the Yellow Band (YB). YB features have been associated with transitions arising from donor levels due to interstitial cadmium ($I_{Cd}$) sites [10-12].

In the $CdCl_2$ treated film there is also a feature around the 2.35-2.55 eV region. This region can be decomposed into two peaks: the first one centred at 2.44 eV referred to the Green Band (GB) which is due to interstitial sulfur [11], i.e. some sulfur atoms are in excess in these films and the second one centred at 2.53 eV, near band edge of CdS at 10K (2.58 eV), has been attributed to the bound exciton peak [10]. The presence of the bound exciton indicates a better crystalline quality for $CdCl_2$ treated samples than as-grown and air annealed samples. The lower energy band also change its intensity and slightly to lower energies after annealing. , and has been ascribed to interstitial sulfur ($I_S$) sites [10].
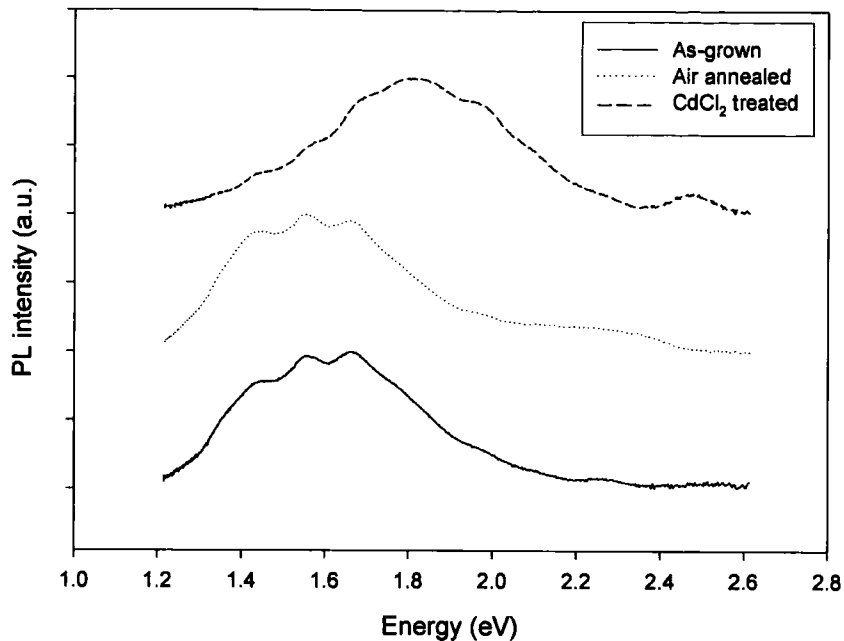
**Figure 6.3:** PL spectra taken at 4K for CBD-samples; i) As-grown, ii) Air annealed at 400°C for 1 hour and iii) CdCl₂ treated and air annealed at 400°C for 1 hour.

From this PL work alone, no evidence of cubic-hexagonal phase change upon air annealing can be seen: such a phase change might be expected to be associated with a decrease in transition energies tied to the bandgap, but this was not observed. However, major changes in the spectra were observed upon CdCl₂ treatment. This could be attributed to a phase transition and/or better crystallinity and also to the influence of the Cl doping [13].

## 6.3.2 Cadmium Sulphide Grown by MOCVD

Photoluminescence spectra for MOCVD CdS films deposited at different temperatures and II/VI ratios are shown in Figure 6.4. All the samples show a broad band centered at 2.0 eV. This transition has been previously associated with radiative transitions from donor levels arising from Cd atoms in interstitial sites ($I_{Cd}$) to conduction band [14] . Both temperature and II/VI ratio influence the shape and position of this band's features.

Compared to that for low II/VI ratio, growth at II/VI ratio of 1.0 caused the peak at 2.0 eV to shift a lower. It also became much broader when the growth temperature was increased. An additional weak band around 2.3-2.6 eV region, appears in films grown at the highest temperature used (330°C) with low II/VI ratio (0.78). This weak is the superposition of two bands: i) the green band region centred at 2.44 eV, that is associated with sulfur interstitial [10]. The green band is itself consistent with there excess sulfur precursor present during the growth. ii) the bound exciton centered around 2.55 eV.

Photoluminescence depends strongly on the growth temperature and II/VI ratio. Hence, sample sgen 24 grown at 330°C with a II/VI ratio of 0.78 reveals higher crystallinity due the presence of the excitonic bound [10].
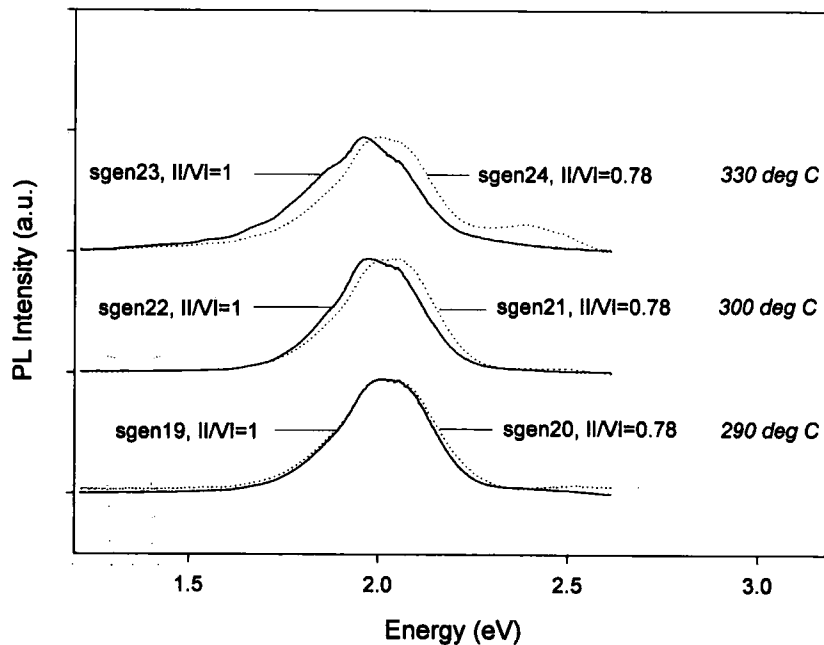


**Figure 6.4:** **PL spectra taken at 4K for MOCVD-samples deposited from 290 to 330°C and for two different II/VI ratios of 0.78 and 1.0**

The literature contains some examples of the influence of II/VI ration on the properties of epitaxial and thin film II/VI compounds. For example, Yodo et al. [15] reported that the crystallographic structure of MOCVD CdS epilayers grown on (100)-orientated GaAs substrate are largely related to

the II/VI source gas mole ratio, and changes from hexagonal into cubic (100) structure with increasing II/VI ratio. Chu et al. [16] has also demonstrated for the first time the intrinsic doping of MOCVD CdTe by varying the DMCd/DIPTe molar ratio in the reaction mixture. The intrinsic doping has a pronounced effect on the photoluminescence of CdTe films. Chou et al. [17] also performed PL measurements to investigate the defects in CdTe films grown in different ambients: Cd- or Te-rich growth ambient. The peak associated with the Te vacancies or its complex was present in Cd-rich but absent in Te-rich growth ambient.

# 6.4 Scanning Electron Microscopy

The reader is referred to section 3.2.3 for a description of scanning electron microscopy (SEM). SEM is a well-established technique for investigating the morphology of films.

## 6.4.1 Cadmium Sulphide Grown by CBD

Figure 6.5 shows scanning electron micrographs of the as-deposited CdS, the 400°C air-annealed and the $CdCl_2$ treated samples. As can be seen from the figure, the as-deposited film has small particles on its surface. These particles are likely to originate from the precipitation of CdS onto the surface. After annealing the layers revealed a network of fractures on the layer: this is most likely to occur during cooling. In heterojunction applications, these film fractures may cause pinholes that may affect the electronic characteristics of the solar cell by shorting the device. After being $CdCl_2$ treated and annealed at 400°C for 1 hour, CdS films exhibited the same network of fractures. However, larger particles were present on the films and were concentrated along the fracture lines. The particles were not analysed but may be $CdCl_2$ or CdS. In a related study, Lee et al. [18] have also reported that sintering CdS with 9% $CdCl_2$ at 700°C showed a segregation of $CdCl_2$ along the grain boundaries.

According to Kaur, Pandya, and Chopra the structure of CBD CdS is determined by the deposition mechanism [19]. When the CdS crystal lattice is constructed on the substrate with ions migrating in the solution, the crystal structure is hexagonal. When the CdS particles are formed in the solution and then precipitate on the substrate the CdS is zinc blende cubic. A study of the film structure of the CBD CdS will be presented in section 6.5 and 6.6.

(a)
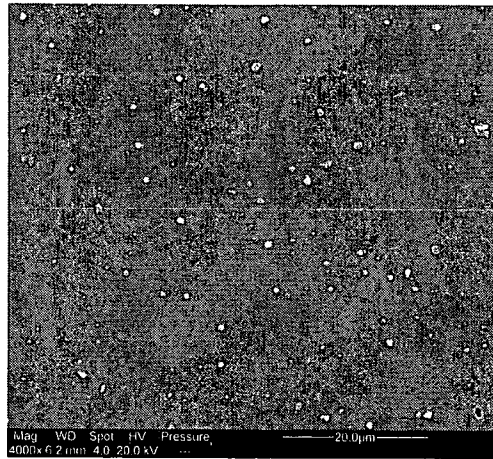


(b)
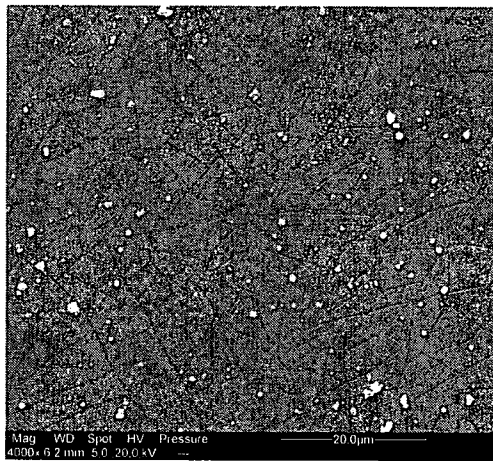


(c)
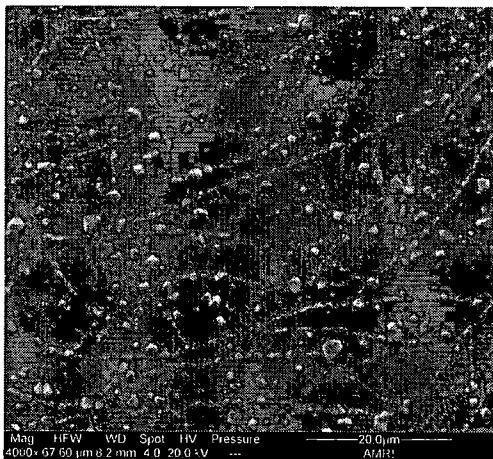


**Figure 6.5:** **Scanning electron micrographs of CBD-grown CdS films (a) as-deposited, (b) 400°C annealed in air and (c) CdCl$_2$ treated.**

## 6.4.2 Cadmium Sulphide Grown by MOCVD

The MOCVD CdS films were 1.5 cm² in area and were used specifically for transmission electron microscopy. Therefore in this section, only one sample among the six samples provided by the University of Bangor, was investigated by scanning electron microscopy, as samples coated with gold can not be used for TEM analysis. Figure 6.6 shows a micrograph of MOCVD CdS grown at 290°C for a II/VI ratio of 0.78. It can be seen from the figure that, the films are very dense.
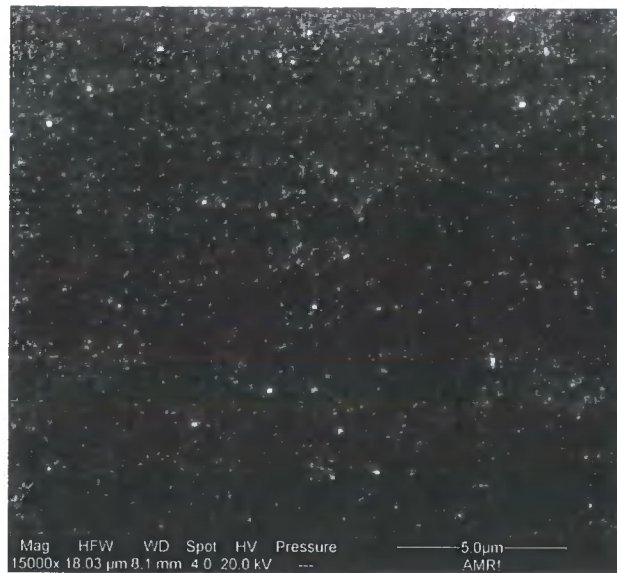


**Figure 6.6:** **Scanning electron micrograph of MOCVD grown at 290°C for a II/VI ratio of 0.78.**

# 6.5 GIXRD Analysis

Because the CdS films are so thin, normal $\theta$-$2\theta$ XRD analysis provided only limited information on the film structure. Therefore, grazing-angle incidence was used – this uses an incident X-ray beam at very small angle with respect to the film surface. While larger incidence angles probe deeper inside the film, small angles probe regions close to the surface. In the case of observation of the CdS films, the best results were obtained with an angle of 0.7°. Grazing incidence XRD is described more fully in the section 3.3.4.

## 6.5.1 Cadmium Sulphide Grown by CBD

GIXRD of the CBD films is presented in Figure 6.7. For a small grazing incidence angle (0.7°), CdS peaks appear clearly. In the untreated sample there is one dominant peak centred at 26.91° and a much smaller peak at around 48.9°. The main peak is related to both (002) hexagonal-CdS and (111) cubic-CdS structure, showing in general a strong selection of the (002) plane. The latter is attributed to the (103) hexagonal-CdS. As mentioned in the section 3.3.4, GIXRD characterisation method constrains the measurement to populations of lattice planes that are tilted with respect to the specimen plane. Thereby, it seems to be inadequate and inappropriate to refer to any "preferential orientation". However, in the following when the term of "preferential orientation" will be quoted, it will refer to a strong selected orientation.

In the annealed sample, the same two peaks remain, however the main peak shifted towards a lower value of $2\theta$. This may also be due to the reduction of strain within the sample, as a result of some degree of recrystallisation. However, the nature of the strain could not be determined with only two diffraction peak. In both post-processed samples, the reflections from the (111), (200), (220) and (311) planes of cadmium oxide appear as shown in Figure 6.7. The presence of the CdO phase might be due to the oxidation of the CdS [1, 20]. Kylner et al. [21] has shown that

heating in air eliminates water from $Cd(OH)_2$ to give CdO. The presence of this phase can be explained by a transformation of the cubic CdS (unstable compared to the hexagonal CdS) to give the CdO [22, 23].

After the $CdCl_2$ treatment, the (103) hexagonal CdS peak was better defined, and this demonstrated a clear evidence of a greater degree of hexagonal modification in thin films. It also revealed the presence of some other hexagonal-CdS reflections, namely (210) and (213) were also present.
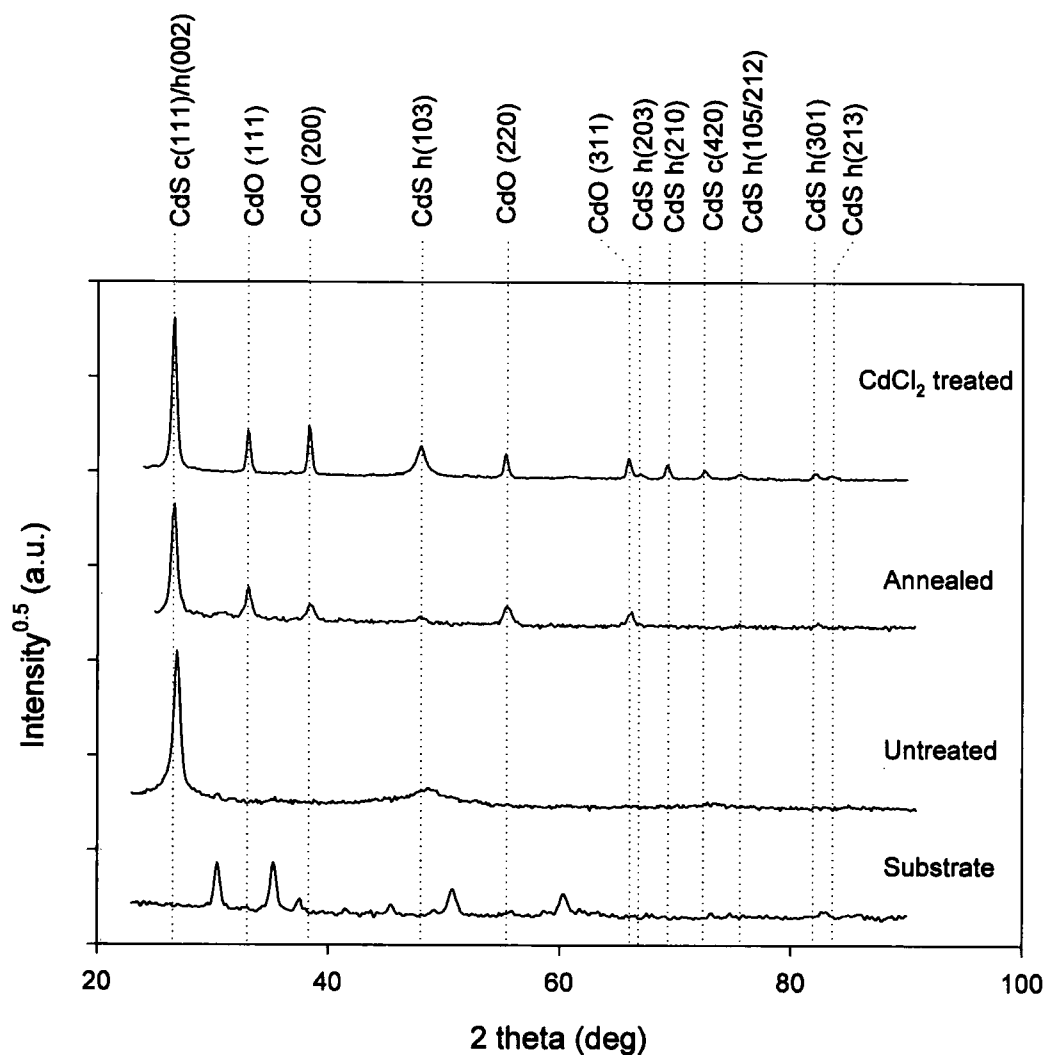


**Figure 6.7:** **GIXRD spectra at incidence angle of 0.7° spectra for CdS grown by CBD.**

From Table 6.1, it is clear that grain growth occurs after both annealing and $CdCl_2$ treatment. The sizes of the crystallites are determined from X-ray diffraction data using Scherrer's formula (see section 3.3.4.1). The FWHM values are seen to decrease with the annealing. The (002) reflection exhibited the largest crystallite sizes compared to the (103), (210) and (213) reflections. The crystallite size for as-grown samples were found to be 20.3 nm, and increased to 21.3 nm for the films annealed in air at 400°C. Metin et al. [1] have reported similar observations after annealing in a nitrogen atmosphere.

There is a major change after the $CdCl_2$ treatment. The $CdCl_2$ treated films have sharper peaks. The decrease in peak width is associated with an increase in grain size (see TEM results) and a decrease in the stress within the film. Unfortunately, these two effects could not be fully separated in the diffraction pattern. Moutinho et al. [24] reported that after $CdCl_2$ treatment, cubic untreated CBD CdS films recrystallised to the hexagonal phase, resulting in better crystallinity and lower density of planar defects.

| Sample condition | (002) | | | (103) | | | (210) | | | (213) | | |
| --- | --- | --- | --- | --- | --- | --- | --- | --- | --- | --- | --- | --- |
| | Position (°) | FWHM (°) | Crystalline size (nm) | Position (°) | FWHM (°) | Crystalline size (nm) | Position (°) | FWHM (°) | Crystalline size (nm) | Position (°) | FWHM (°) | Crystalline size (nm) |
| As-deposited | 26.9 | 0.448 | 20.3 | 48.6 | 3.055 | 3.2 | - | - | - | - | - | - |
| Annealed in air at 400°C for 1 hour | 26.6 | 0.426 | 21.3 | 47.9 | 0.641 | 15.1 | - | - | - | - | - | - |
| $CdCl_2$ treated | 26.6 | 0.340 | 26.7 | 47.9 | 0.635 | 15.2 | 69.3 | 0.299 | 36 | 83.4 | 0.425 | 27.9 |

**Table 6.1:** **The crystalline size of the hexagonal reflections present in CBD CdS thin films.**

Results of texture and degree analysis [25] are presented in the Table 6.2, in which $C_{hkl}$ and $\sigma$ values for treated and untreated samples are compared.

| Sample condition | $C_{khl}$ | | | | $\sigma$ |
|---|---|---|---|---|---|
| | (002) | (103) | (210) | (213) | |
| **As-deposited** | 3.94 | 0.06 | 0 | 0 | 1.7 |
| **Annealed in air at 400°C for 1 hour** | 3.96 | 0.04 | 0 | 0 | 1.7 |
| **CdCl₂ treated** | 3.69 | 0.18 | 0.09 | 0.03 | 1.6 |

**Table 6.2:** **Values of texture coefficient C and degree of preferential orientation (σ) for CBD CdS samples before and after being treated**

As seen from Table 6.2 and Figure 6.7, all samples showed strong selection of the (002) direction. Post-growth treatment, such as air annealing and $CdCl_2$ treatment had little effect on the orientation of the samples, as can be inferred from the values of $C_{hkl}$ and $\sigma$. While $CdCl_2$ treatment induced a slight amount of film randomisation, the overall trend in all samples was for the (002/111) peak to be dominant.

## 6.5.2 Cadmium Sulphide Grown by MOCVD

Similar X-ray diffraction analysis applied to MOCVD CdS is presented here. Figure 6.8 shows X-ray diffraction curves of MOCVD CdS films deposited at different temperature and for two different II/VI ratios. CdS films deposited by MOCVD show a predominant peak at $2\theta = 26.6°$ which can be assigned to the (002) plane of hexagonal or the (111) plane of cubic CdS.
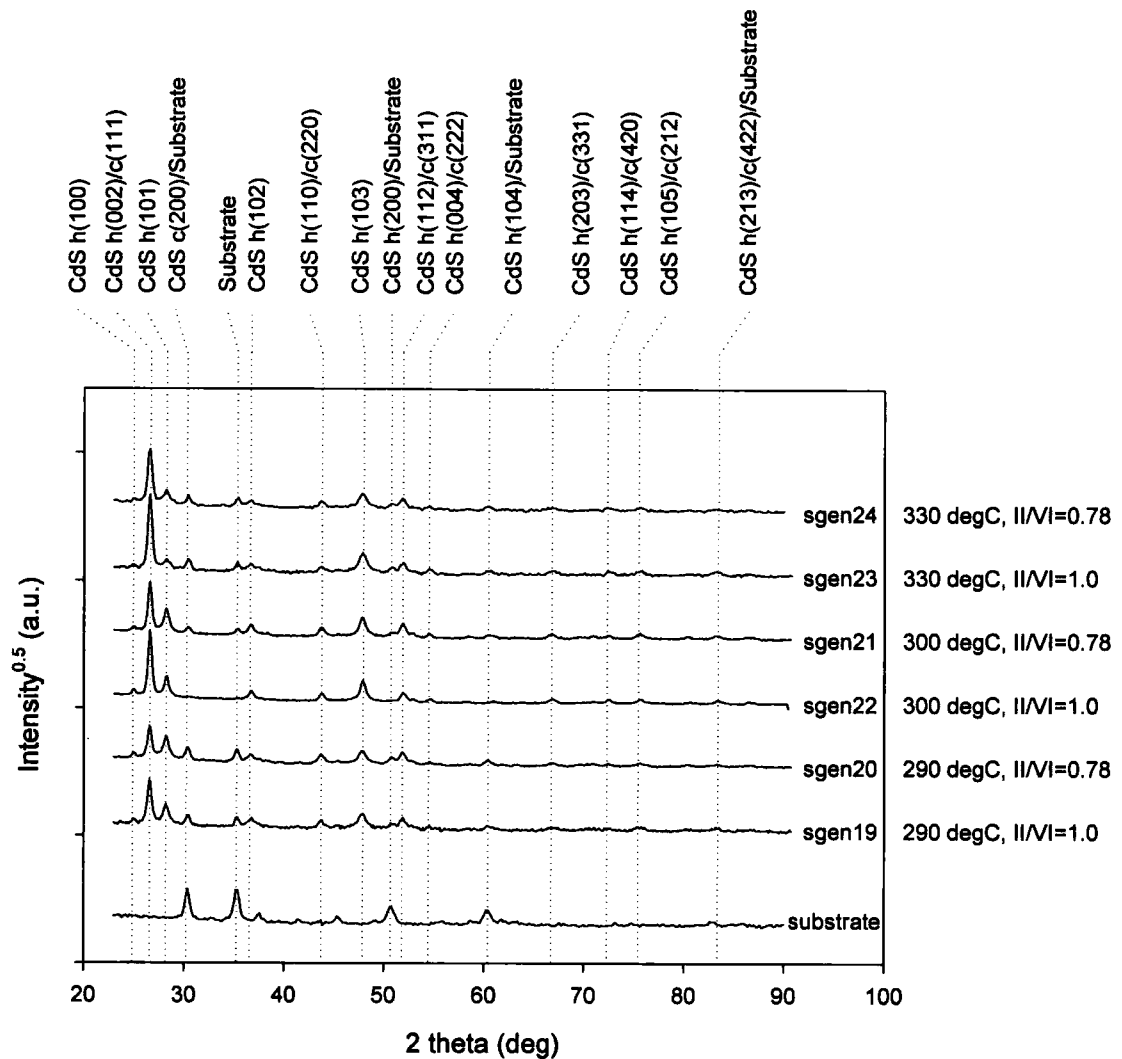
**Figure 6.8:** XRD spectra at incidence angle of 0.7° for CdS grown by MOCVD deposited under different conditions and for an ITO substrate

Minor contributions to the spectrum are also present from hexagonal phase material of different orientations and tentatively assigned to cubic phase CdS as indicated in Figure 6.8. However, in this study XRD produced no definitive presence for cubic CdS in any films, and the following discussion assumes that they contain only the hexagonal phase CdS formed under most film growth conditions [26]. The triplet of peaks centred at 24.9°, 26.7° and 28.3° can be assigned to the CdS (101), (002) and (101) reflections, which are representative of hexagonal structure. These diffraction patterns invariably show weak (102) and (103) reflections, which do not coincide with any cubic powder pattern peaks.
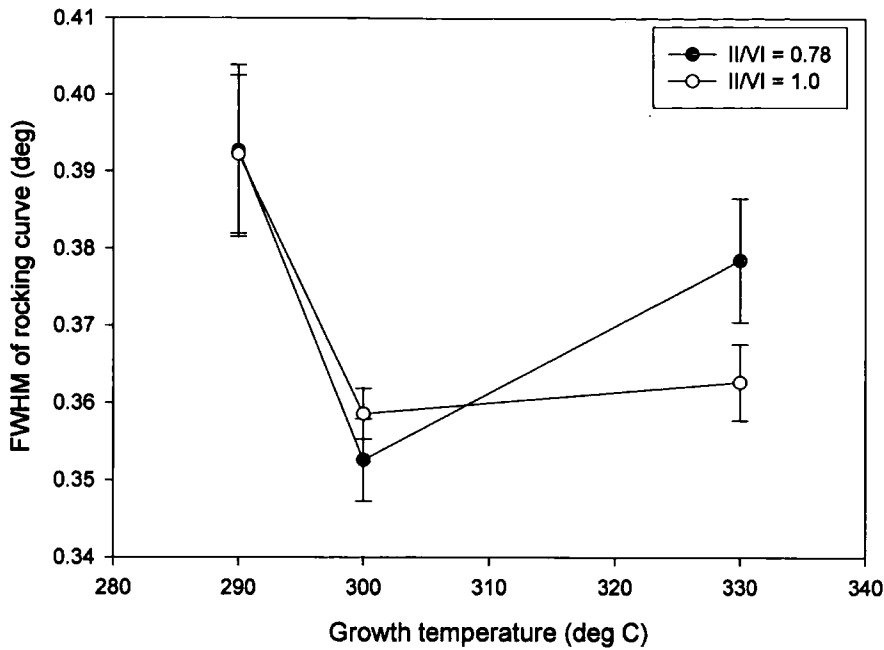
**Figure 6.9:** **FWHM of hexagonal (002) CdS diffraction peak grown at two different ratios for various temperatures.**

This probably indicates that hexagonal type crystallographic structure is formed more easily in MOCVD. Figure 6.9 shows the FWHM of the hexagonal (002) CdS diffraction peak grown at two different ratios for various temperatures. It shows that the crystalline quality of the thin films is apparently best at the optimum growth temperature of 300°C and for a II/VI ratio of 0.78.

The crystallite sizes calculated using Scherrer's equation for each reflection of hexagonal type CdS are presented in Table 6.3.

| Sample | II/VI ratio | Temperature (°C) | Crystallite size (nm) | | | | | | | | | |
|--------|-------------|------------------|-------|-------|-------|-------|-------|-------|-------|-------|-------|-------|
| | | | (100) | (002) | (101) | (102) | (110) | (103) | (112) | (203) | (105) | (300) |
| sgen24 | 0.78 | 330 | 21.3 | 24 | 17.4 | 11.2 | 18.4 | 14.1 | 17.9 | 9.4 | 14.4 | × |
| sgen21 | 0.78 | 300 | 11 | 25.8 | 18.9 | 16.2 | 17.6 | 18.2 | 17.1 | 15.5 | 14.4 | 13.4 |
| sgen20 | 0.78 | 290 | 21.6 | 23.1 | 18 | 10 | 16 | 14.4 | 15.5 | 15.7 | 12.3 | 17.9 |
| sgen23 | 1 | 330 | 23 | 25 | 14.1 | 8.6 | 14.6 | 14.1 | 16.3 | 13.1 | 16 | × |
| sgen22 | 1 | 300 | 0.9 | 25.3 | 21.3 | 17.4 | 19.3 | 20.9 | 17.5 | 15.8 | 18.3 | × |
| sgen19 | 1 | 290 | 26.2 | 23.1 | 17.4 | 10.7 | 21.5 | 14.8 | 16.4 | 11.1 | 13 | 10.7 |

**Table 6.3:** **The crystallite size of the hexagonal reflections present in MOCVD CdS thin films. The 'x' label indicates that the peak did not appear in the XRD spectrum.**

From Table 6.3 and Figure 6.8, the influence of both temperature and II/VI ratio on the diffraction patterns and Scherrer grain sizes can be seen.

In general the crystallite size or grain size diameter varies from 10 to 26.0nm. The largest grains were obtained for the (002) reflections, of which the mean value is 24.4 nm for all the films. The (002) reflection is the dominant peak in the XRD spectrum and so the grain size deduced from it are discussed first. Samples grown at 290°C promote smaller grains compared to those grown at a higher temperature. It seems that samples deposited at 300°C generate the largest grains; this can be noticeable for the (002) reflection. For samples grown at 330°C, the crystallite size decreases slightly compared to those at grown a 300°C. However, this latter trend is not general and can not be applied to all reflections. In the optimum case, where the largest grains were obtained, i.e. CdS thin film deposited at 300°C, it was noticed that the grain size increased slightly with an increase of the II/VI ratio. Grain sizes of 25.3 and 25.8nm were calculated for II/VI ratio of 0.78 and 1.0 respectively. The influence of growth conditions on the grain size is further investigated by real space (TEM) grain size and analysis in section 6.6.

To study preferential orientation in CdS films, 10 peaks were used in the calculation, which gave a maximum value of σ equal to 2.3, corresponding to an almost completely oriented sample.

| Sample | II/VI ratio | T (°C) | $C_{hkl}$ (100) | (002) | (101) | (102) | (110) | (103) | (112) | (203) | (105) | (300) | σ |
|---|---|---|---|---|---|---|---|---|---|---|---|---|---|
| sgen24 | 0.78 | 330 | 0.1 | 7 | 0.4 | 0.4 | 0.3 | 0.7 | 0.6 | 0.2 | 0.4 | 0 | 2 |
| sgen21 | 0.78 | 300 | 0.1 | 5.2 | 0.7 | 0.7 | 0.3 | 1 | 0.7 | 0.3 | 0.5 | 0.4 | 1.4 |
| sgen20 | 0.78 | 290 | 0.2 | 4.4 | 1.1 | 0.7 | 0.5 | 0.8 | 1 | 0.3 | 0.4 | 0.4 | 1.2 |
| sgen23 | 1 | 330 | 0.1 | 7.8 | 0.1 | 0.3 | 0.1 | 0.7 | 0.3 | 0.2 | 0.3 | 0 | 2.3 |
| sgen22 | 1 | 300 | 0.1 | 7.1 | 0.4 | 0.5 | 0.2 | 0.8 | 0.3 | 0.2 | 0.3 | 0 | 2 |
| sgen19 | 1 | 290 | 0.2 | 5.8 | 0.7 | 0.7 | 0.4 | 0.8 | 0.6 | 0.2 | 0.4 | 0.3 | 1.6 |

**Table 6.4:** **Values of texture coefficient C and degree of preferential orientation (σ) for MOCVD CdS samples grown in different conditions**

From Table 6.4 and Figure 6.8, we notice that all the MOCVD films were orientated such GIXRD selects the (002) reflections more strongly than any other. Although the sample deposited at 290°C for a II/VI ratio of 0.78 showed stronger orientation in the (101), (112) and (103) planes, as the growth temperature increased, the sample become strongly (002) orientated. We attributed this to the substrate, which provides sites of low energy and also provided a reference plane during growth of CdS. For both II/VI ratios, the texture increased with an increase in growth temperature, evidenced by higher values of $C_{hkl}$ and σ for a growth temperature of 330°C. By comparing the $C_{hkl}$ and σ values, for the different II/VI ratios, it was found that the higher II/VI ratio of 1.0 exhibited a higher degree of orientation.

In order to confirm the exact structure of the films, the structural analysis is detected with TEM. This will be presented in section 6.6.

# 6.6 Transmission Electron Microscopy Analysis

In this section, the structure of CdS thin films grown by CBD and MOCVD has been investigated using transmission electron microscopy (section 3.2.5). In order to confirm the exact structure of the film, the structural analysis was directed towards TEM. Then for both deposition methods, the grain size was measured and a fit to grain radius distribution was proposed.

## 6.6.1 Cadmium Sulphide Grown by CBD

For the CBD samples it was not possible to obtain data for as-grown samples since they broke upon chemical thinning. Therefore, only samples which were post-processed were investigated.

### Structural Analysis

Plan-view samples were examined and the images contained information about both the CdS and TCO layers. To decouple this information it was therefore necessary to use dark field imaging. The diffraction pattern from the plan view specimens contained rings from both the CdS and TCO layers. Since there is little known about the inter-planar spacings of this commercial ITO ($In_2O_3$-$SnO_2$ solid solution) the CdS rings were identified from the JCPDS data. Decoupling of the CdS from the TCO information was also assessed by the being a sample in which the CdS layer became detached from the ITO, making it possible to record ITO information alone. This is described later in this chapter.

Figure 6.10 shows the diffraction pattern and bright and dark field images of CBD CdS samples with the followed post-growth treatments: a) air annealed at 400°C for 1 hour and b) $CdCl_2$ evaporated following by air annealing at 400°C for 1 hour. The diffraction rings for both samples are continuous, indicating a large number of grains, having different orientations in the analysed area.

There was no noticeable difference in terms of recrystallisation between annealed and $CdCl_2$ treated samples that could be detected from the diffraction pattern. Bearing in mind that an increase in grain size results in a smaller number of grains diffracting the electron beam, and consequently, a smaller number of spots in the diffraction pattern, making the change from continuous to fragmented. Indeed both diffraction patterns were similar, indicating that both films had broadly similar grain sizes and crystal structure.

All the (hkl) indices of diffraction rings observed matched well with those of JCPDS 6-0314 [27] and JCPDS 10-0454 [28] for hexagonal and cubic CdS respectively as shown in the Table 6.5 and Table 6.6 for annealed and $CdCl_2$ treated samples. Most of the rings of hexagonal and cubic lattice have similar positions, but the hexagonal phase can be identified by few rings. The strong and medium intensity diffraction rings corresponded to the h(100), h(002)/c(111), h(110)/c(220), h(112)/c(311) and h(211) reflections of hexagonal (h) and cubic (c) of CdS. Therefore, the existing experimental results indicate that the structure of the annealed and $CdCl_2$ treated CBD CdS is mainly hexagonal – like in character.

It is also worth mentioning that XRD and TEM analysis do not provide the same information on the structural phase since some reflections observed in the TEM were not present in the XRD. An example the (103) hexagonal reflection was present in the XRD spectrum but not in the selective area diffraction (SAD). This anomaly could be due to the different volumes of the films sampled by TEM and GIXRD. While TEM samples the whole 30 nm thickness, GIXRD samples the uppermost 5 nm only. Other studies have reported that for thinner CDB samples, the orientation is more random than for thicker ones in which a preferred orientation develops [29-31]. Similar anomalies between XRD and transmission electron diffraction have been reported elsewhere [30-32].

## Grain Size Distribution Analysis

To form the dark-field images (DFI) of the CdS alone, the objective aperture was placed over either a single ring or groups of closely spaced rings from the CdS. For the grain size analysis dark-field TEM negatives were scanned and the individual grains were marked by hand on transparent foil. The grains obtained were re-scanned to give bitmaps that could be interpreted using "PC image" data analysis software. "PC image" recorded the area of each object defined; this data was converted to grain radii by assuming the grains to be circular. (This is a common assumption, the method of using the mean centroid to calculate the grain boundary distance is more complex to execute [20]).

Figure 6.11 shows the grain size distributions for the groups of rings listed in Table 6.7. Grain size distribution can be modelled by a number of functions. These functions are derived from a physical and theoretical basis, and often used to describe grain size evolution with time [33]. Two popular distributions were studied for the fitting of the experimental distributions, and are described below.

***The Rayleigh Distribution:*** This distribution resulted from Louat's analysis of grain boundary based on the random diffusion of sections of grain boundaries [34].

$$f(r) = ar \exp\left\{ -\left( \frac{r}{r_o} \right)^2 \right\}$$  Eq. 6.1

where a, $r_0$ are constants

***Log-Normal Distribution:*** This distribution differs from the Rayleigh distribution in that it was as a starting assumption from Feltham's model of grain growth [35]. In the form used by Feltham the log-normal distribution is

$$f(r) = \frac{a}{r_o} \exp\left\{ -\frac{\left[\ln\frac{r}{r_o}\right]^2}{2\sigma^2} \right\}$$

Eq. 6.2

where a, $r_0$ and $\sigma$ are constants

Figure 6.12 shows the two distributions fitted to an example of the actual data. In the majority of cases, it was found that the log-normal distribution provided the best fit to the data, whereas the Rayleigh fitting is not representative of the grain size distribution. This is, perhaps predictable as the equation contains three, rather than two variable parameters.

From Table 6.7, overall the $CdCl_2$ treated samples exhibited larger grains than the annealed in air samples. For the $CdCl_2$ treated samples there is a grain size of approximately ~23.0 nm, compared to 13.0 nm for the annealed one. These results are in agreement with those found from XRD analysis. Using both characterisation methods, it was found that the (002) reflection exhibited the largest grain size and that $CdCl_2$ treated samples showed significantly larger grains than did air annealed samples. A clear trend emerges from the dark-field images obtained using group A rings, i.e. the (100) and (002) reflections of hexagonal CdS that are stronger in the diffraction patterns.

A general conclusion about the GIXRD and TEM measurements is also that the nature of microscopic and diffraction measurements of grain size is fundamentally different and that direct (absolute) comparisons of the results of each are generally improper.

|  | a) CdS Air Annealed | b) CdS CdCl₂ + Air Annealed |
|---|---|---|
| DP | | |
| BFI | | |
| DFI | | |
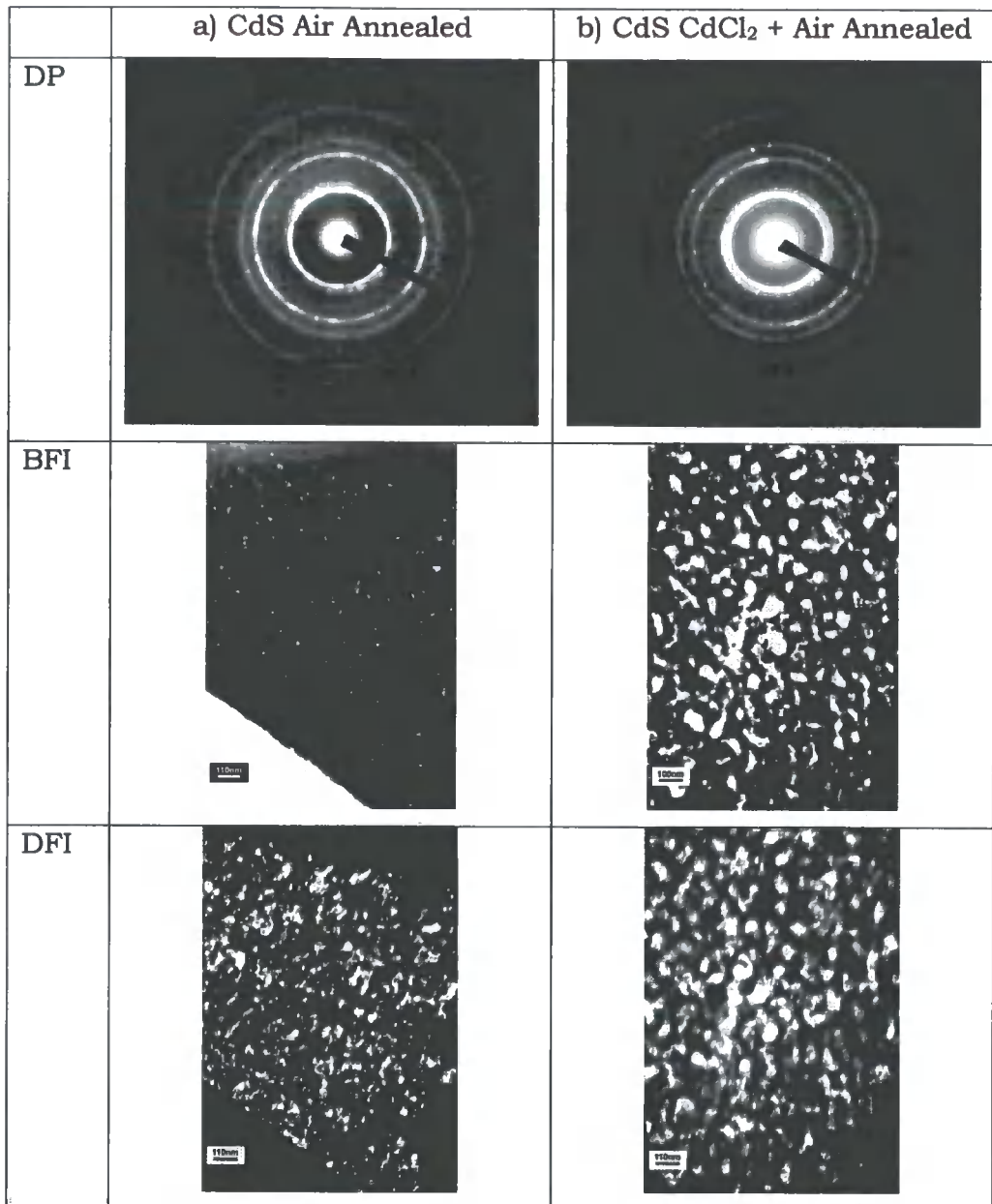
**Figure 6.10:** Diffraction pattern, bright and dark field images of CBD CdS a) air annealing at 400°C for 1 hour, b) CdCl₂ evaporation followed air annealing at 400°C for 1 hour. Hence, for the dark field images the objective aperture was placed over the 1st group of closely spaced rings from the CdS. This group includes the hexagonal (100 and 002) and the cubic (111) planes.

| Observed data | | | JCPDS Data | | |
|---|---|---|---|---|---|
| Ring No. | d spacing [Å] | Intensity | d spacing [Å] | hkl | Intensity [%] |
| 1 | 3.692 | strong | 3.569 | h100 | 60 |
| 2 | 3.262 | medium | 3.355 | c111 | 100 |
| | | | 3.341 | h002 | 44 |
| | | | 3.148 | h101 | 100 |
| | | | 2.906 | c200 | 23 |
| 3 | 2.540 | very weak | | | |
| | | | 2.439 | h102 | 26 |
| 4 | 2.102 | medium | 2.061 | h110 | 46 |
| | | | 2.055 | c220 | 52 |
| | | | 1.890 | h103 | 45 |
| | | | 1.784 | h200 | 7 |
| 5 | 1.793 | medium | 1.754 | h112 | 34 |
| | | | 1.752 | c311 | 39 |
| | | | 1.724 | h201 | 15 |
| | | | 1.678 | c222 | 5 |
| | | | 1.671 | h004 | 2 |
| 6 | 1.603 | very weak | | | |
| | | | 1.574 | h202 | 6 |
| | | | 1.513 | h104 | 2 |
| | | | 1.453 | c400 | 7 |
| | | | 1.393 | h203 | 14 |
| 7 | 1.356 | weak | 1.349 | h210 | 5 |
| | | | 1.333 | c331 | 13 |
| | | | 1.322 | h211 | 11 |
| | | | 1.299 | c420 | 6 |
| | | | 1.298 | h114 | 5 |
| | | | 1.252 | h105 | 9 |
| | | | 1.251 | h212 | 5 |
| 8 | 1.201 | very weak | 1.220 | h204 | <1 |
| | | | 1.190 | h300 | 6 |
| | | | 1.186 | c422 | 13 |
| | | | 1.171 | h301 | <1 |
| 9 | 1.150 | very weak | 1.154 | h213 | 14 |
| | | | 1.121 | h302 | 6 |
| | | | 1.118 | c511 | 7 |
| | | | 1.118 | c333 | 2 |
| | | | 1.114 | h006 | <1 |
| | | | 1.070 | h205 | 5 |
| | | | 1.063 | h106 | 1 |
| 10 | 1.051 | very weak | 1.050 | h214 | 1 |
| | | | 1.049 | h303 | <1 |
| | | | 1.030 | h220 | 4 |
| | | | 1.027 | c440 | 4 |
| 11 | 1.002 | very weak | | | |
| | | | 0.9898 | h310 | 2 |

**Table 6.5:** Comparison of the d spacings calculated from the TEM diffraction pattern of CBD CdS air annealed at 400°C for 1 hour above with the JCPDS data of Greenockite (h) and Hawleyite (c) CdS structure.

| Observed data | | | JCPDS Data | | |
|---|---|---|---|---|---|
| Ring No. | d spacing [Å] | Intensity | d spacing [Å] | hkl | Intensity [%] |
| 1 | 3.692 | strong | 3.569 | h100 | 60 |
| 2 | 3.221 | medium | ⌠ 3.355 | c111 | 100 |
|  |  |  | ⌡ 3.341 | h002 | 44 |
|  |  |  | 3.148 | h101 | 100 |
|  |  |  | 2.906 | c200 | 23 |
| 3 | 2.523 | very weak |  |  |  |
|  |  |  | 2.439 | h102 | 26 |
| 4 | 2.102 | medium | ⌠ 2.061 | h110 | 46 |
|  |  |  | ⌡ 2.055 | c220 | 52 |
|  |  |  | 1.890 | h103 | 45 |
|  |  |  | ⌠ 1.784 | h200 | 7 |
| 5 | 1.793 | medium | ⎮ 1.754 | h112 | 34 |
|  |  |  | ⌡ 1.752 | c311 | 39 |
|  |  |  | 1.724 | h201 | 15 |
|  |  |  | ⌠ 1.678 | c222 | 5 |
|  |  |  | ⌡ 1.671 | h004 | 2 |
| 6 | 1.603 | very weak |  |  |  |
|  |  |  | ⌠ 1.574 | h202 | 6 |
|  |  |  | ⌡ 1.513 | h104 | 2 |
|  |  |  | 1.453 | c400 | 7 |
| 7 | 1.428 | very weak |  |  |  |
|  |  |  | ⌠ 1.393 | h203 | 14 |
| 8 | 1.356 | weak | ⎮ 1.349 | h210 | 5 |
|  |  |  | ⎮ 1.333 | c331 | 13 |
|  |  |  | ⌡ 1.322 | h211 | 11 |
|  |  |  | 1.299 | c420 | 6 |
|  |  |  | 1.298 | h114 | 5 |
|  |  |  | ⌠ 1.252 | h105 | 9 |
| 9 | 1.278 | very weak | ⌡ 1.251 | h212 | 5 |
| 10 | 1.211 | very weak | 1.220 | h204 | <1 |
|  |  |  | ⌠ 1.190 | h300 | 6 |
|  |  |  | ⌡ 1.186 | c422 | 13 |
| 11 | 1.173 | very weak | 1.171 | h301 | <1 |
|  |  |  | 1.154 | h213 | 14 |
|  |  |  | ⌠ 1.121 | h302 | 6 |
|  |  |  | ⎮ 1.118 | c333 | 2 |
| 12 | 1.138 | very weak | ⎮ 1.118 | c511 | 7 |
|  |  |  | ⌡ 1.114 | h006 | <1 |

**Table 6.6:** Comparison of the d spacings calculated from the TEM diffraction pattern of CBD CdS CdCl₂ evaporation following air annealing at 400°C for 1 hour, above with JCPDS data of Greenockite (h) and Hawleyite (c) CdS structure.
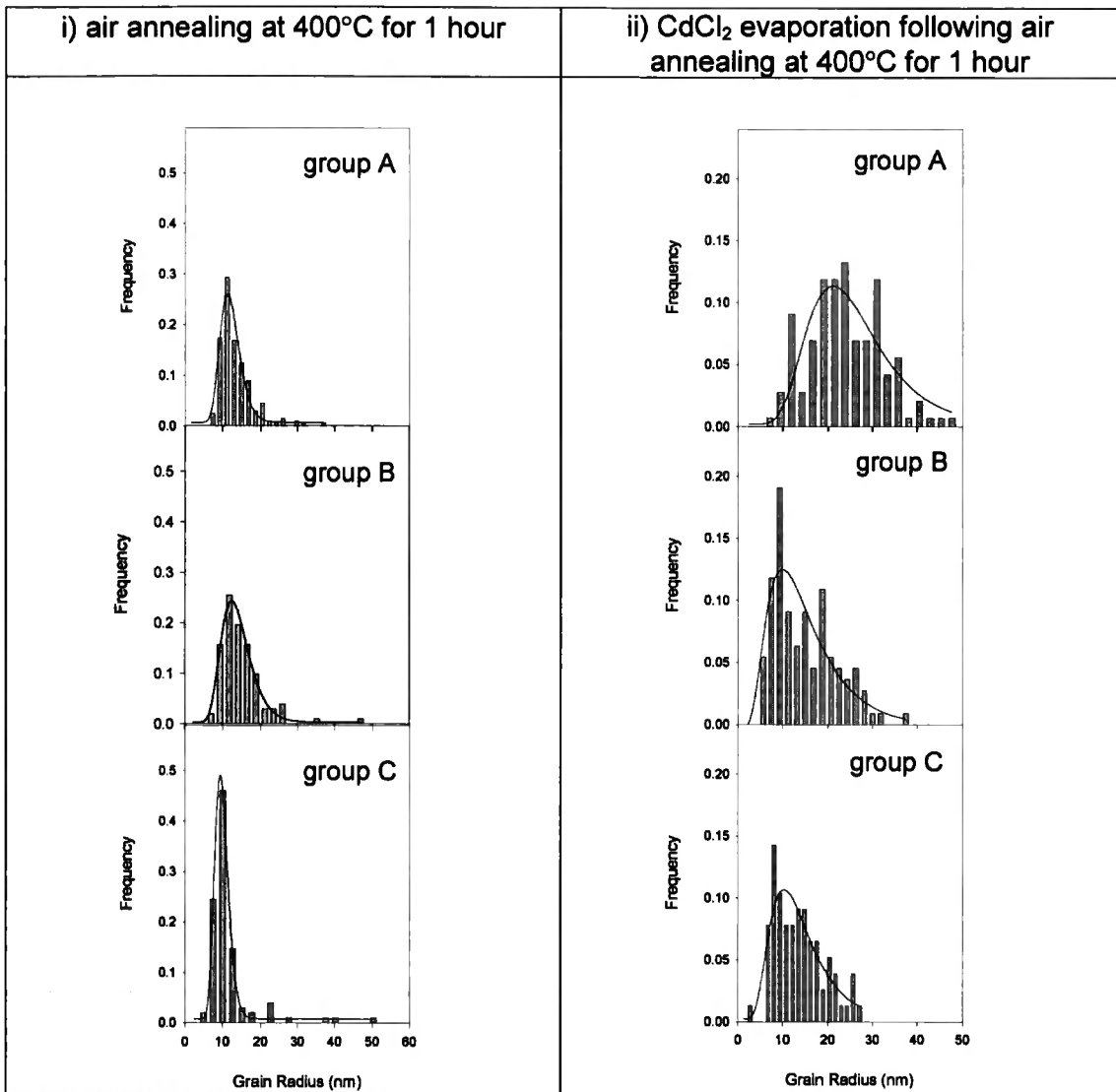
**Figure 6.11:** Grain size distribution for CBD CdS i) air annealing at 400°C for 1 hour, ii) CdCl₂ evaporation following air annealing at 400°C for 1 hour. A, B and C correspond to the groups of rings listed in Table 6.7. The log-normal distribution is shown with a solid line.
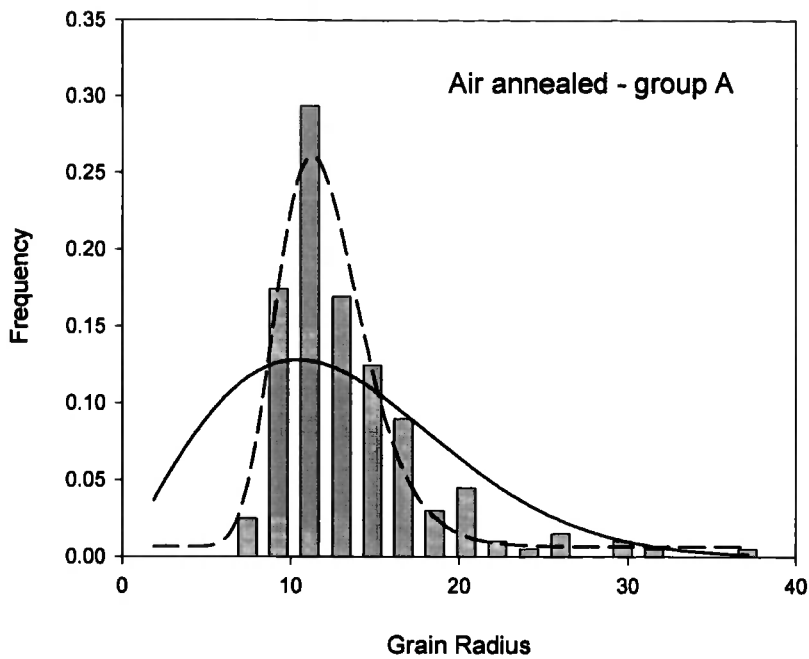
**Figure 6.12:** **Histogram of actual grain size data showing two different types of fit used to describe such distributions: Rayleigh (solid line) and log-normal (dashed). The log normal provides the statistically best fit in the great majority of cases.**

| Sample | group A h002/c111 h101 | | | | | group B h110/c220 | | | | | group C h112/c311 | | | | |
|---|---|---|---|---|---|---|---|---|---|---|---|---|---|---|---|
| | Mode | μ | $\sigma_{N-1}$ | α | N | Mode | μ | $\sigma_{N-1}$ | α | N | Mode | μ | $\sigma_{N-1}$ | α | N |
| As-grown | × | × | × | × | × | × | × | × | × | × | × | × | × | × | × |
| Air annealed | 8.2 | 12.9 | 6.8 | 0.5 | 202 | 8.9 | 15.2 | 9.9 | 1.4 | 49 | 1.7 | 10.2 | 5.7 | 1.1 | 29 |
| CdCl₂ treated | 22.7 | 22.7 | 8.1 | 0.7 | 143 | 5.2 | 14.0 | 6.9 | 0.7 | 110 | 7.4 | 13.0 | 5.5 | 0.6 | 77 |

**Table 6.7:** **CBD CdS grain radii statistics with values of the mode, the mean (μ), the standard deviation ($\sigma_{N-1}$), the standard error (α) and N, the count number. The 'x' label indicates that the data were not obtained. The values are expressed in nm.**

## 6.6.2 Cadmium Sulphide Grown by MOCVD

### Structural Analysis

MOCVD CdS samples were also investigated using the same plan-view TEM methods employed for CBD CdS,. As mentioned in the previous section, dark-filed imaging is used to decouple information about the ITO and CdS layers. However, for all of the MOCVD-grown CdS/ITO films, the two layers became accidentally separated during sample preparation. This is an opportunity to study both in bright filed mode individually. For all CdS thin films, TEM imaging shows the presence of two different layers which are superimposed, as shown in Figure 6.13.
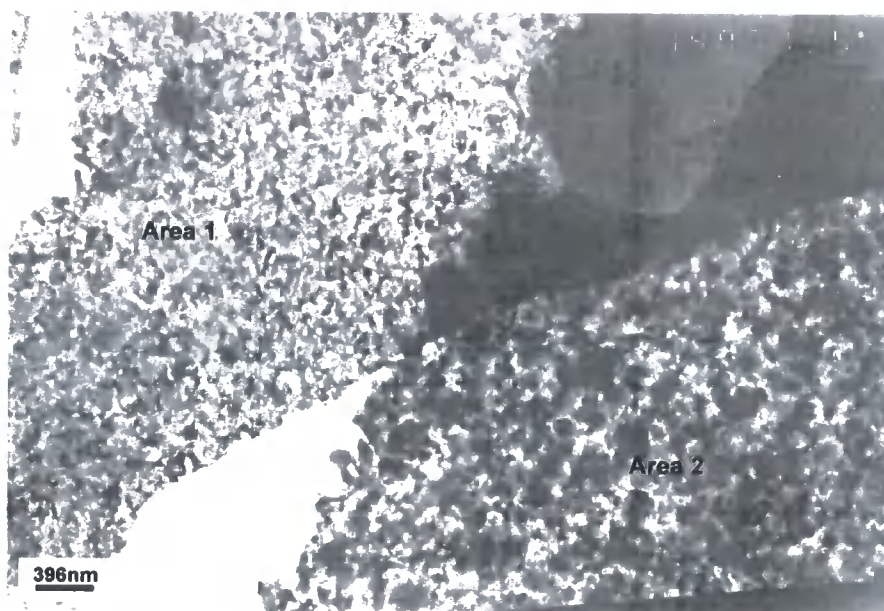


**Figure 6.13:** **Bright field image of CdS deposited at 330°C with a II/VI ratio of 1.0. It shows two different morphologies. The areas 1 and 2 correspond to the ITO and CdS layers respectively.**

As can be seen in Figure 6.13 and Figure 6.14, the two layers are different in terms of microstructure. By examining the diffraction pattern of each layer, it was possible to determine the crystallographic structure and phase of each layer. For the CdS, the indices of diffraction rings obtained matched well with those of JCPDS 6-0314 and JCPDS 10-0454 for

hexagonal and cubic CdS respectively, for the area 2 as shown in the Table 6.8. Therefore, the area 1 was ascribed to be the ITO. Comparison of the transmission electron diffraction pattern with the GIXRD patterns from the substrate can be also done. It was possible to identify the CdS layers in the same way for all samples investigated. Only one diffraction pattern of MOCVD CdS samples is presented since all the diffraction patterns obtained were quite similar.

|  | ITO | CdS |
|---|---|---|
| DP | | |
| BFI | | |
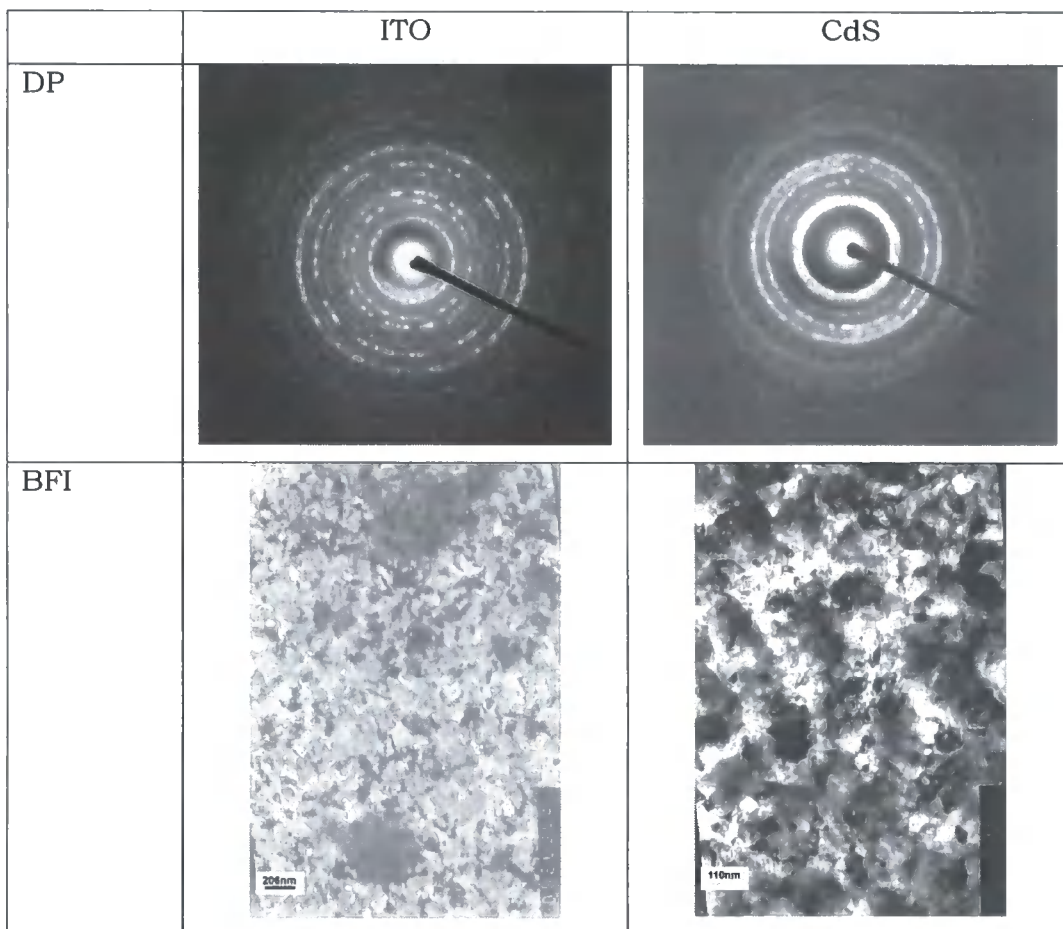
**Figure 6.14: Diffraction pattern and enlarged bright field images taken from the areas 1 and 2 (i.e. ITO and CdS layers) of Figure 8.16.**

From Table 6.8, it is clear that the structure of CdS grown by MOCVD is hexagonal phase. No cubic phase, no complex of cubic and hexagonal or any secondary phases were observed. Diffracted rings from (100), (002), (101), (102), (110) and (112) planes were observed. These results are confirmed and are in agreement with those found from the XRD analysis.

| Observed data | | | JCPDS data | | |
|---|---|---|---|---|---|
| Ring No. | d spacing [Å] | Intensity | d spacing [Å] | hkl | Intensity [%] |
| 1 | 3.692 | very strong | 3.569 | h100 | 60 |
| 2 | 3.379 | weak | ⌠ 3.355 | c111 | 100 |
|  |  |  | ⌡ 3.341 | h002 | 44 |
| 3 | 3.153 | strong | 3.148 | h101 | 100 |
|  |  |  | 2.906 | c200 | 23 |
| 4 | 2.481 | medium | 2.439 | h102 | 26 |
| 5 | 2.150 | strong | ⌠ 2.061 | c110 | 46 |
|  |  |  | ⌡ 2.055 | c220 | 52 |
| 6 | 1.931 | weak |  |  |  |
|  |  |  | 1.890 | h103 | 45 |
| 7 | 1.781 | strong | ⌠ 1.784 | h200 | 7 |
|  |  |  | ⎮ 1.754 | h112 | 34 |
|  |  |  | ⌡ 1.752 | c311 | 39 |
|  |  |  | 1.724 | h201 | 15 |
|  |  |  | ⌠ 1.678 | c222 | 5 |
|  |  |  | ⌡ 1.671 | h004 | 2 |
| 8 | 1.603 | weak |  |  |  |
|  |  |  | ⌠ 1.574 | h202 | 6 |
|  |  |  | ⌡ 1.513 | h104 | 2 |
|  |  |  | 1.453 | c400 | 7 |
| 9 | 1.428 | weak |  |  |  |
|  |  |  | 1.393 | h203 | 14 |
| 10 | 1.356 | medium |  |  |  |
|  |  |  | ⌠ 1.349 | h210 | 5 |
|  |  |  | ⎮ 1.333 | c311 | 13 |
|  |  |  | ⌡ 1.322 | h211 | 11 |
|  |  |  | 1.299 | c420 | 6 |
|  |  |  | 1.298 | h114 | 5 |
| 11 | 1.272 | weak |  |  |  |
|  |  |  | 1.252 | h105 | 9 |
|  |  |  | 1.251 | h212 | 5 |
|  |  |  | 1.220 | h204 | 1 |
| 12 | 1.205 | weak |  |  |  |
|  |  |  | 1.190 | h300 | 6 |
|  |  |  | 1.186 | c422 | 13 |
|  |  |  | 1.171 | h301 | <1 |
| 13 | 1.168 | weak |  |  |  |
|  |  |  | 1.154 | h213 | 14 |

**Table 6.8:** Comparison of the d spacings calculated from the TEM diffraction pattern of MOCVD CdS deposited at 330°C with a II/VI ratio of 1.0 with JCPDS data of Greenockite (h) and Hawleyite (c) CdS structure.

## Grain Size Distribution

Figure 6.15 shows the bright and dark field images of two MOCVD CdS samples deposited with a II/VI ratio of 0.78 at different growth temperatures. As we can see from the dark field images, the grains are larger when samples are grown at higher temperatures. Both growth temperature and II/VI ratio seem to influence the grain size distribution.

Figure 6.16 shows the grain size distribution for a different group of rings listed in Table 6.9. It is evident that the growth temperature is an important variable which can influence the grain size distribution. From the histograms, samples grown at higher temperature exhibited broader grain size distributions and higher mean values of radius. Grain size maximum varied up to 80 nm and 200 nm from growth temperature of 290°C and 330°C respectively, for a II/VI ratio of 0.78. A statistical study of the grain size distribution data is presented in Table 6.7. In general, group A which corresponds to the (100), (002) and (101) reflections of hexagonal CdS exhibits the largest grain size. The grain size is highly dependent on the growth temperature. MOCVD CdS has a grain size of about ~24.3 nm when grown at ~290°C, increasing to ~46.2 nm when grown at higher temperature of 330°C. The II/VI ratio also has a clear effect on the grain size; particularly at higher temperatures, it was found that at lower II/VI ratio of 0.78 the grains were larger than those grown at a II/VI ratio of 1.0. While at the low growth temperature, the II/VI ratio does not seem to affect the grain size. These is consistent with PL results found for low growth temperature; both II/VI ratio revealed similar properties and features.

Grain size distribution can be modelled by a number of distributions, as has been described in section 6.6.1. Figure 6.17 shows the two distributions fitted to the actual data. In the majority of cases, it was found that log-normal distribution provided the best fit to the data. However, in some cases this model could not be applied; for instance group B of SGEN23, instead of following a log-normal distribution like in the majority

of cases, had two local maxima at ~2 and ~28 nm and a mean value of ~21 nm. This kind of distribution is usually called bimodal distribution. This observation may suggest that some reflections do not have the same distribution which highly depends on the growth parameters. These results are not clearly understood and need to be further clarified.

| | i) II/VI=0.78<br>T=290°C | ii) II/VI=0.78<br>T=330°C |
|---|---|---|
| BFI |  |  |
| DFI |  |  |
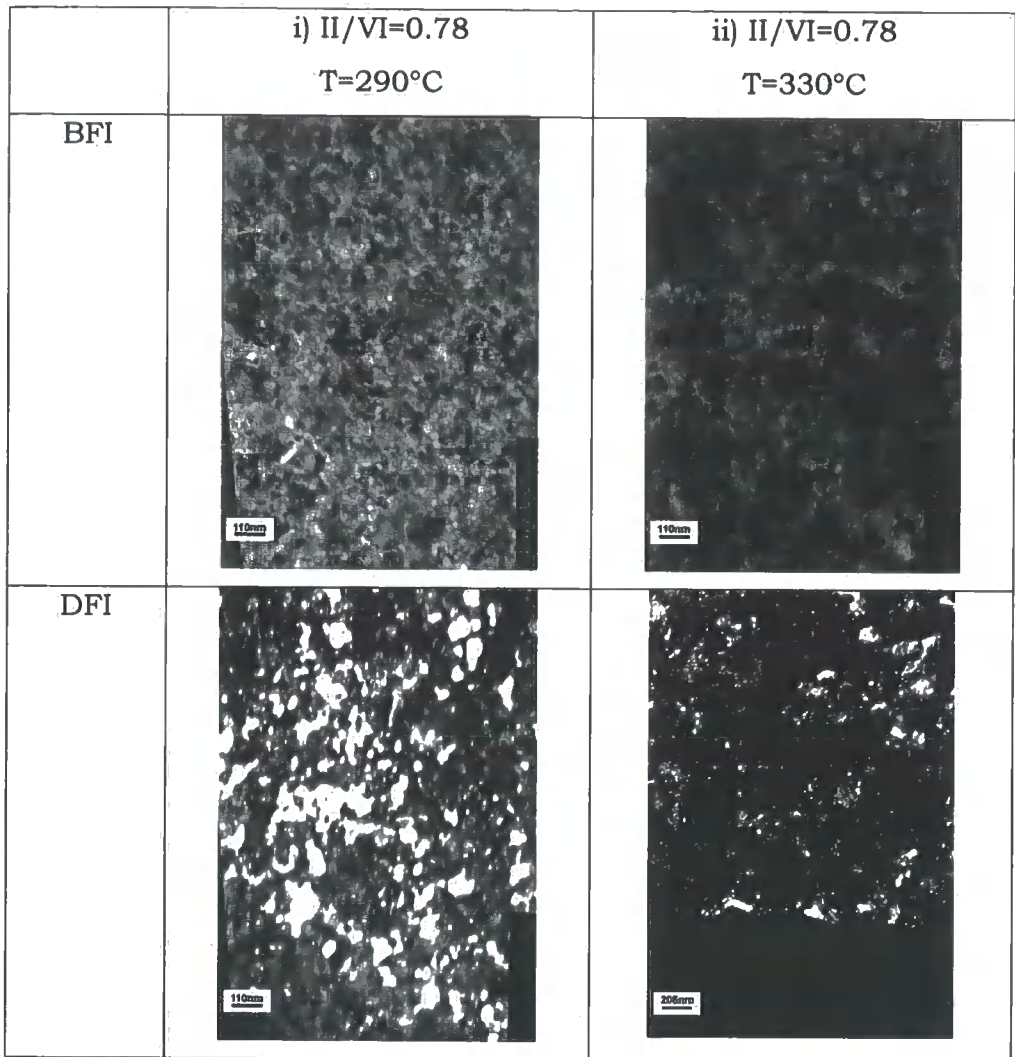
**Figure 6.15:** **Bright and dark field images of MOCVD CdS deposited at i) T=290°C, ii) T=330°C for a II/VI ratio of 0.78. Hence, for the dark field images the objective aperture was placed over the 1st group of closely spaced rings from the CdS. This group includes the hexagonal (100, 002 and 101) and the cubic (111) planes.**
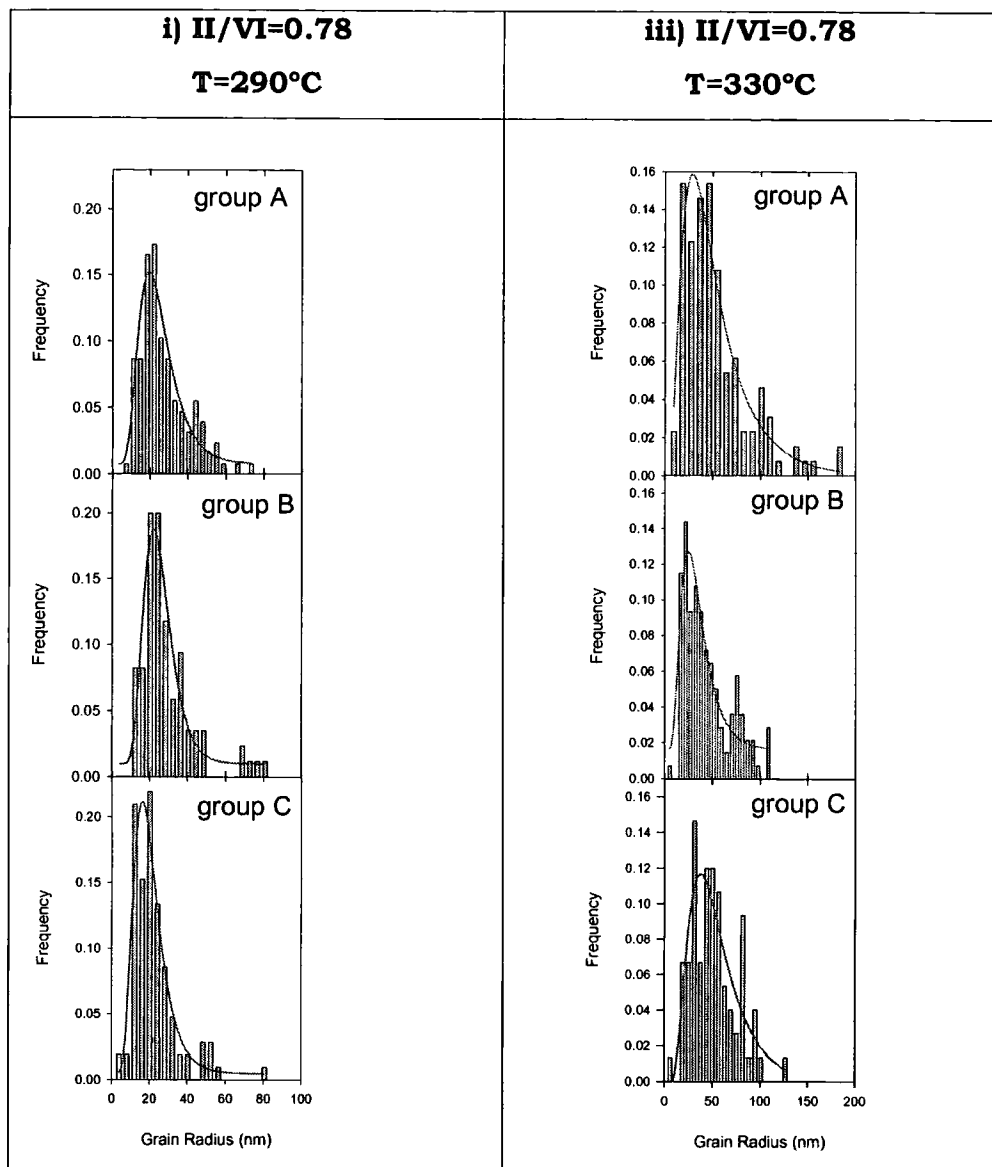
**Figure 6.16:** Grain size distribution for MOCVD CdS CdS layers deposited at 290 and 330°C for two different precursor ratios (II/VI) of 0.78 and 1.0. The groups A, B and C correspond to the groups of indexes listed in Table 6.8. The log-normal distribution is shown with a solid line.

| Sample | II/VI | T (°C) | TEM analysis | | | | | | | | | | | | | | |
| | | | group A h100 h002/c111 h101 | | | | | group B h110/c220 | | | | | group C h112/c311 | | | | |
| | | | Mode | μ | σN–1 | α | N | Mode | μ | σN–1 | α | N | Mode | μ | σN–1 | α | N |
| sgen 24 | 0.78 | 330 | 17.1 | 48.6 | 35.1 | 3.1 | 130 | 15.5 | 41.5 | 24.5 | 2.1 | 139 | 29.6 | 48.5 | 23.7 | 2.7 | 75 |
| sgen 23 | 1 | 330 | 21.0 | 37.6 | 27.4 | 3.8 | 52 | 1.7 | 21.3 | 22.7 | 2.8 | 65 | 22.2 | 25.2 | 12.3 | 2.0 | 36 |
| sgen 22 | 1 | 300 | 21.9 | 26.4 | 13.7 | 1.6 | 70 | 22.1 | 22.3 | 10.5 | 1.4 | 55 | 19.1 | 24.8 | 10.9 | 1.6 | 48 |
| sgen 20 | 0.78 | 290 | 16.7 | 25.3 | 12.9 | 1.1 | 127 | 23.5 | 27.1 | 14.4 | 1.6 | 85 | 26.0 | 20.5 | 12.3 | 1.2 | 105 |

**Table 6.9:** **MOCVD CdS grain radii statistics with values of the mode, the mean ($\mu$), the standard deviation ($\sigma_{N-1}$), the standard error ($\alpha$) and N the count number. The values are expressed in nm.**
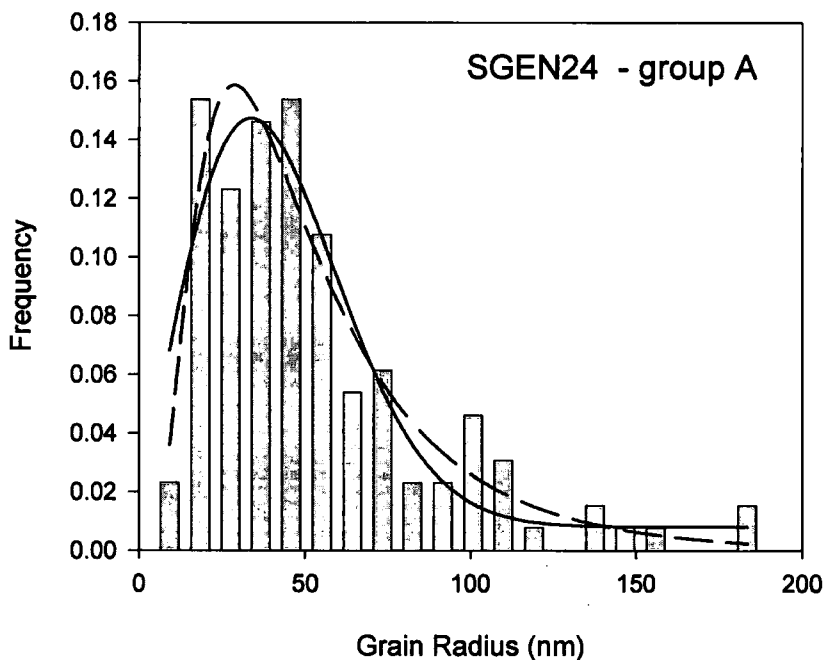


**Figure 6.17:** **Histogram of actual grain size data showing two different types of fit used to describe the distribution: Rayleigh (solid line) and log-normal (dashed). The log normal provides the best fit for most MOCVD-grown samples.**

# 6.7 Discussion

## 6.7.1 CBD CdS

In section 6.2.1, transmittance analysis showed a decrease in bandgap after air annealing and $CdCl_2$ treatment. It has been recently shown that the transition between cubic and hexagonal modifications in chemical bath deposited films as a function of annealed temperature resulted in a non-monotonic variation of bandgap values with the presence of a sharp minimum in $Eg=f(T)$ curve situated at about 250°C [4, 12, 23, 36, 37]. In other papers, a decrease in bandgap has also been reported for annealed treatments up to 400°C in air [38]. This indicates that a common phenomenon is probably responsible for this effect. Despite the formation of CdO as reported in section 6.5.1, the decrease in bandgap after post-treatment is likely a consequence of the transition processes between cubic and hexagonal structures. Furthermore, this reduction in bandgap could also be due to the development of grain-related states [7] or more likely due to a reduction of strain within the films. The presence of a CdO phase might be due to the oxidation of the CdS [1, 20]. Kylner et al. [21] has shown that heating in air eliminates water from $Cd(OH)_2$ to give CdO. The presence of this phase can be explained by a transformation of the cubic CdS (unstable compared to the hexagonal CdS) to give the CdO [22, 23]. The presence of CdO may also explain the reduction the optical bandgap of CdS.

In section 6.3.1, photoluminescence revealed an enhancement of crystallinity after $CdCl_2$ treatment evidenced by the presence of the bound exciton transition [10], whereas the as-grown and air annealed samples showed some similarities, including the presence of the red band which is commonly ascribed to either sulfur vacancy states [10] or surface states [11]. Also, a weak yellow band appeared after annealing; this arises from donor levels due to interstitial cadmium ($I_{cd}$) sites [10-12].

In section 6.4.1, SEM images showed that thermal stress on annealing resulted in the formation of fissures within the layers. These could affect the optimal operation of the solar cell device.

In section 6.5.1, XRD studies showed that all the samples have strong selected orientation along the (002) plane of the hexagonal CdS structure and a peak at about 48.9° which has been ascribed to the (103) plane of hexagonal structure. No phase transition has been noticed on annealing but some degree of recrystallisation was observed: the X-ray patterns were seen to be sharper and the crystallinity was found to increase modestly after both post-treatments. The crystalline sizes of the strong selected orientation were found to be 20.3±0.3, 21.3±0.3 and 26.7±0.1 nm for the as-deposited, air annealed and $CdCl_2$ treated samples.

In section 6.6.1, TEM diffraction pattern studies showed that both post-treated samples were a complex of cubic and hexagonal phases. Hence, XRD and TEM analysis do not provide exactly the same information on the structural phases. (Some reflections in the TEM were not present in the X-ray diffraction pattern). This anomaly could be either due to the difference in the sample thickness which is 30 nm for SAD and 5 nm for GIXRD, could be also due to the fundamental difference between the natures of microscopic and diffraction measurements, in terms of orientation selection. However, selective diffraction patterns should provide more precise analysis of structural changes, since SAD pattern shows all the phases present in the films. There was no apparent difference in terms of recrystallisation from the SAD patterns between the annealed and the $CdCl_2$ treated samples. Dark field (DF) images allow determination of the grain size radii. Firstly, both XRD and TEM analysis confirmed that larger grains are obtained after the $CdCl_2$ treatment than air annealing. However, the grain sizes measured from the DF images were larger than those determined by XRD analysis. For the $CdCl_2$ treated samples, the grain sizes measured from DF images were nearly two times larger than those obtained using Scherrer's formula. Hence, direct or absolute comparisons between grain sizes determined either by XRD and TEM seemed to be improper as

the natures of the microscopy and diffraction measurements are fundamentally different.

## 6.7.2 MOCVD CdS

In section 6.2.2 and 6.3.2, transmittance analysis showed that neither the II/VI ratio or the growth temperature affected the energy bandgap. Only a decrease of 10 meV in bandgap is observed from 290 to 330°C. However, photoluminescence measurements revealed that both parameters influence the luminescence of MOCVD CdS thin films. All the films exhibited a broad band centred at 2.0 eV: it has been previously associated with radiative transitions from donor levels arising from Cd atoms in interstitial sites ($I_{Cd}$) to conduction band [14]. By varying the growth temperature and II/VI ratio, this band changes in shape. However, the sample (SGEN24) grown at 330°C with a II/VI ratio of 0.78 revealed higher crystallinity due to the presence of the excitonic bound transition [10]. Therefore by modifying the II/VI ratio and the growth temperature it is possible to achieve better crystallinity.

In section 6.4.2, SEM images show that MOCVD CdS thin films were dense.

In section 6.5.2, XRD studies showed that MOCVD CdS thin films contained only hexagonal phases under most film growth and as the growth temperature increased, the selected (002) orientation became stronger. It showed also that the crystalline quality is best at the optimum growth temperature of 300°C and for a II/VI ratio of 0.78. This configuration also exhibited the largest crystalline size of about ~28 nm for the stronger selected orientation.

In section 6.6.2, TEM diffraction pattern studies showed that the structure of CdS grown by MOCVD is hexagonal phase, which is in agreement with XRD analysis. It was also found that the II/VI ratio also

has a clear effect on the grain size distribution in particular at a higher temperature of 330°C. It was found that at a lower II/VI ratio of 0.78 the average crystalline sizes were larger (~98 nm) than those grown at II/VI ratio of 1.0 (~78 nm). The crystalline size was determined using the group of rings which included the (002) reflection.

Both XRD and TEM analysis showed that sample grown with a II/VI ratio of 0.78 and at growth temperature above 300°C exhibited the largest grains. However, TEM grain size measured were more than four times larger than those determined by XRD. As described in section 6.7.1, direct or absolute comparisons of grain size between XRD and TEM analysis could be inappropriate.

By correlating the PL and TEM results, it was found that the sample sgen24 (growth temperature of 330°C and a II/VI of 0.78) promoted not only the largest grains (from TEM observations) but also an excitonic bound transition centred around 2.55 eV (observed in PL spectrum). This suggests that the excitonic bound transition could be a major factor in obtaining large grains.

By varying the II/VI ratio and the growth temperature and by the use of photoluminescence spectroscopy and XRD prior to TEM in which specimen preparation takes a long time, it is possible to estimate efficiently and rapidly the crystalline quality and the grain size.

The next two tables summarise the principles optical and structural properties of the CBD and MOCVD CdS.

| Samples | Principal properties |
|---|---|
| **As-grown** | *Optical transmittance:*<br>$E_g$= 2.51eV<br><br>*Photoluminescence:*<br>i) "Red Band" due to sulfur vacancies [10] or surface states [11]<br><br>*GIXRD:*<br>Strong selected (h002/c111) orientation<br>Maximum grain size ≈ 20 nm<br><br>*TEM:*<br>Structure: undetermined<br>Maximum grain size ≈ undetermined |
| **Air annealed** | *Optical transmittance:*<br>$E_g$= 2.38eV<br><br>*Photoluminescence:*<br>i) "Red Band" due to sulfur vacancies [10] or surface states [11]<br>ii) weak "Yellow Band" due transitions arising from donor levels due to interstitial cadmium ($I_{Cd}$) sites [10-12].<br><br>*GIXRD:*<br>Strong selected (h002/c111) orientation<br>Maximum grain size ≈ 21 nm<br><br>*TEM:*<br>Structure: Hexagonal<br>Maximum grain size ≈ 25.8 nm |
| **CdCl₂ treated** | *Optical transmittance:*<br>$E_g$= 2.44eV<br><br>*Photoluminescence:*<br>Green Band (GB) which is due to interstitial sulfur [11]<br>Bound exciton peak at 2.53 eV [10]<br><br>*GIXRD:*<br>Strong selected (h002/c111) orientation<br>Maximum grain size ≈ 26 nm<br><br>*TEM:*<br>Structure: Hexagonal<br>Maximum grain size ≈ 45.4 nm |

**Table 6.10:** **Principal properties of CBD CdS. The label "x" indicates that the value was not determined.**

| Sample | II/VI ratio | T (°C) | Principal properties |
|---|---|---|---|
| Sgen 20 | 0.78 | 290 | *Optical transmittance:*<br>$E_g$= 2.40eV<br>*Photoluminescence:*<br>Peak at 2.0 eV attributed to S vacancies [13]<br>*GIXRD:*<br>Structure: Hexagonal<br>Maximum grain size ≈ 23.1 nm<br>*TEM:*<br>Structure: Hexagonal<br>Maximum grain size ≈ 51 nm |
| Sgen 21 | 0.78 | 300 | *Optical transmittance:*<br>$E_g$= 2.41eV<br>*Photoluminescence:*<br>Peak at 2.0 eV attributed to S vacancies [13]<br>*GIXRD:*<br>Structure: Hexagonal<br>Maximum grain size ≈ 25.8 nm<br>*TEM:*<br>Structure: x<br>Maximum grain size ≈ x nm |
| Sgen 24 | 0.78 | 330 | *Optical transmittance:*<br>$E_g$= 2.41eV<br>*Photoluminescence:*<br>Peak at 2.0 eV attributed to S vacancies [13]<br>Green Band (GB) which is due to interstitial sulfur [11]<br>Bound exciton peak at 2.53 eV [10]<br>*GIXRD:*<br>Structure: Hexagonal<br>Maximum grain size ≈ 24.0 nm<br>*TEM:*<br>Structure: Hexagonal<br>Maximum grain size ≈ 97 nm |
| Sgen 19 | 1.0 | 290 | *Optical transmittance:*<br>$E_g$= 2.40eV<br>*Photoluminescence:*<br>Peak at 2.0 eV attributed to S vacancies [13]<br>*GIXRD:*<br>Structure: Hexagonal<br>Maximum grain size ≈ 23.1 nm<br>*TEM:*<br>Structure: x<br>Maximum grain size ≈ x nm |
| Sgen 22 | 1.0 | 300 | *Optical transmittance:*<br>$E_g$= 2.41eV<br>*Photoluminescence:*<br>Peak at 2.0 eV attributed to S vacancies [13]<br>*GIXRD:*<br>Strong selected (h002/c111) orientation<br>Maximum grain size ≈ 25.3 nm<br>*TEM:*<br>Structure: Hexagonal<br>Maximum grain size ≈ 53 nm |
| Sgen 23 | 1.0 | 330 | *Optical transmittance:*<br>$E_g$= 2.41eV<br>*Photoluminescence:*<br>Peak at 2.0 eV attributed to S vacancies [13]<br>*GIXRD:*<br>Structure: Hexagonal<br>Maximum grain size ≈ 25 nm<br>*TEM:*<br>Structure: Hexagonal<br>Maximum grain size ≈ 75 nm |

**Table 6.11:** **Principal properties of MOCVD CdS. The label "x" indicates that the value was not determined.**

# 6.8 Conclusion

In this chapter, optical and structural properties of thin film CdS grown by chemical bath deposition (CBD) and metalorganic vapour deposition (MOCVD) have been characterised by using optical transmittance, photoluminescence, SEM, GIXRD and TEM.

Three representative samples have been selected for CBD, allowing us to investigate the influence of post-deposition treatments such as air annealing and $CdCl_2$ treatment on the optical and structural properties of CdS layers. Both post-treatments resulted in a decrease of energy bandgap, which was likely due to transition phase processes. It also showed an enhancement of crystallinity and a modest increase in grain size after being post-growth treated.

The influence of growth parameters such as the II/VI ratio and the growth temperature has been investigated to study the optical and structural properties of MOCVD CdS. Optimisation of these two parameters was performed to obtain the largest grain size. Maximum grain size was obtained for samples grown at 330°C and for II/VI ratio of 0.78.

# 6.9 References

1.   H. Metin and R. Esen, *Annealing studies on CBD grown CdS thin films,* Journal of Crystal Growth **258** (2003) 141-148
2.   P. K. Nair, O. Gomez Daza, A. Arias-Carbajal Readigos, J. Campos, and M. T. S. Nair, *Formation of conductive CdO layer on CdS thin films during air heating,* Semicond. Sci. Technol. **16** (2001) 651
3.   J. M. Dona and J. Herrero, *Chemical Bath Deposition of CdS Thin Films: An Approach to the Chemical Mechanism Through Study of the Film Microstructure,* Journal of The Electrochemical Society **144** (1997) 4081-4091
4.   L. Hermandez, O. de Melo, O. Zelaya-Angel, and R. Lozada-Morales, *Electro-chemical characterization of sulfur-anneled chemical-bath deposited CdS films,* J. Electrochem. Soc. **141** (1994) 3238-3241
5.   O. Zelaya-Angel, J. J. Alvarado-Gil, R. Lozada-Morales, and H. Vargas, *Band-gap shift in CdS semiconductor by photoacoustic spectroscopy: Evidence of a cubic to hexagonal lattice transition,* Applied Physics Letters **64** (1994) 291-293
6.   J. G. Mendoza-Alvarez, J. Gonzalez-Hernandez, F. Sanchez-Sinencio, O. Zelaya, and S. S. Chao, *Luminescence and particle size in microcrystalline CdTe thin films,* Journal of Crystal Growth **86** (1990) 391-395
7.   A. E. Rakhshani and A. S. Al-Azab, *Characterization of CdS films prepared by chemical-bath deposition,* J. Phys. Condens. Matter **12** (2000) 8745-8755
8.   N. Romeo, A. Bosio, R. Tedeschi, A. Romeo, and V. Canevari, *A highly efficient and stable CdTe/CdS thin film solar cell,* Solar Energy Materials and Solar Cells **58** (1999) 209-218
9.   S. C. Park, B. W. Han, J. H. Ahn, B. T. Ahn, and D. Kim, *Effect of CdS annealing in (CdCl$_2$+CdS) atmosphere on CdTe cells,* IEEE (1997) 531-534
10.  J. Aguilar-Hernandez, *Photoluminescence and structural properties of cadmium sulphide thin films grown by different techniques,* Semicond. Sci. Techno. **18** (2003) 111-114
11.  M. Agata, H. Kurase, S. Hayashi, and K. Yamamoto, *Photoluminescence spectra of gas-evaporated CdS microcrystals,* Solid State Communications **76** (1990) 1061-1065
12.  R. Lozada-Morales and O. Zelaya-Angel, *Photoluminescence analysis of CdS thin films under phase transition,* Thin Solid Films **281-282** (1996) 386-389
13.  A. Romeo, D. L. Batzner, H. Zogg, C. Vignali, and A. N. Tiwari, *Influence of CdS growth process on structural and photovoltaic properties of CdTe/CdS solar cells,* Solar Energy Materials and Solar Cells **67** (2001) 311-321
14.  J. J. Ramsdem, S. Webber, and M. Gratzel, *Luminescence of colloidal CdS particles in acetonitrile and acetonitrile/water mixtures,* J. Phys. Chem. **89** (1985) 2740

15. T. Yodo and S. Tanaka, *Growth of CdS by atmospheric pressure metalorganic vapor-phase epitaxy at low temperature,* Journal of Applied Physics **72** (1992) 2781-2790

16. T. L. Chu, S. S. Chu, C. Ferekides, J. Britt, and C. Q. Wu, *Cadmium telluride films by metalorganic chemical vapor deposition,* Journal of Applied Physics **69** (1991) 7651-7655

17. H. C. Chou, A. K. Bhat, S. Kamra, A. Rohatgi, R. R. Arya, L. Russel, and R. K. Ahrenkiel, *The effects of Cd/Te mole ratio in the MOCVD growth ambient on the CdTe solar cells,* IEEE (1993) 481-485

18. J. S. Lee and H. B. Im, J. Mater. Sci. **21** (1986) 980

19. I. Kaur, D. K. Pandya, and K. L. Chopra, *Growth kinetics and ploymorphism of chemically deposited CdS films,* J. Electrochem. Soc. **127** (1980) 943-948

20. A. Cortes, H. Gomez, R. E. Marotti, G. Riveros, and E. A. Dalchiele, *Grain size dependence of the bandgap in chemical bath deposited CdS thin films,* Solar Energy Materials and Solar Cells **82** (2004) 21-34

21. A. Kylner, A. Rockett, and L. Stolt, *Oxygen in solution grown CdS films for thin films solar cells,* Solid State Phenomena **51-52** (1996) 533-540

22. N. Lejmi and O. Savadogo, *The effect of heteropolyacids and isopolyacids on the properties of chemically bath deposited CdS thin films,* Solar Energy Materials and Solar Cells **70** (2001) 71-83

23. S. A. Tomás, O. Vigil, J. J. Alvarado-Gil, R. Lozada-Morales, O. Zelaya-Angel, H. Vargas, and A. Ferreira da Silva, *Influence of thermal annealings in different atmospheres on the band-gap shift and resistivity of CdS thin films,* Journal of Applied Physics **78** (1995) 2204-2207

24. H. R. Moutinho, D. Albin, Y. Yan, R. G. Dhere, X. Li, C. Perkins, C.-S. Jiang, B. To, and M. M. Al-Jassim, *Deposition and properties of CBD and CSS CdS thin films for solar cell application,* Thin Solid Films **436** (2003) 175-180

25. H. R. Moutinho, M. M. Al-Jassim, F. A. Abulfotuh, D. H. Levi, P. C. Dippo, R. G. Dhere, and L. L. Kazmerski, *Recrystallization of CdTe thin films after CdCl2 treatment,* 26th IEEE Photovoltaic Specialists Conf., Anaheim (1997) p. 431

26. P. O'Brien, J. R. Walsh, I. M. Watson, L. Hart, and S. R. P. Silva, *Properties of cadmium sulphide films grown by single-source metalorganic chemical vapour deposition with dithiocarbamate precursors,* Journal of Crystal Growth **167** (1996) 133-142

27. Joint Committee on Powder Diffraction Standards (JCPDS), Card 6-0314, CdS (hexagonal) (1999)

28. Joint Committee on Powder Diffraction Standards (JCPDS), Card 10-0454, CdS (cubic) (1999)

29. A. G. Stanley, *Cadmium sufide solar cells,* Applied Solid State Science **5** (1975) 251-366

30. K. S. Ramaiah, R. D. Pilkington, A. E. Hill, R. D. Tomlinson, and A. K. Bhatnagar, *Structural and optical investigations on CdS thin films grown by chemical bath technique,* Materials Chemistry and Physics **68** (2001) 22-30

31. L. Wenyi, C. Xun, C. Qiulong, and Z. Zhibin, *Influence of growth process on the structural, optical and electrical properties of CBD-CdS films,* Materials Letters **59** (2005) 1-5

32. K. D. Rogers, J. D. Painter, M. J. Healy, D. W. Lane, and M. E. Ozsan, *The crystal structure of CdS-CdTe thin film heterojunction solar cells,* Thin Solid Films **339** (1999) 299-304

33. M. A. Cousins, *Microstructure of absorber layers in CdTe/CdS solar cells / By Michael Andrew Cousins.* (2001)

34. N. P. Louat, *On the theory of normal grain growth,* Acta Mettalurgia **22** (1974) 721-724

35. P. Feltham, *Grain growth in metals,* Acta Metallurgica **5** (1957) 97-105

36. O. Zelaya-Angel, L. Hermandez, J. J. Alvarado-Gil, R. Lozada-Morales, C. Falcony, H. Vargas, and R. Ramirez-Bon, *Band-gap shift in CdS: phase transition from cubic to hexagonal on thermal annealing,* Vacuum **46** (1995) 1083-1085

37. O. De Melo, L. Hernández, O. Zelaya-Angel, R. Lozada-Morales, M. Becerril, and E. Vasco, *Low resistivity cubic phase CdS films by chemical bath deposition technique,* Applied Physics Letters **65** (1994) 1278-1280

38. M. E. Ozsan, D. R. Johnson, M. Sadeghi, D. Sivapathasundaram, G. Goodlet, M. J. Furlong, L. M. Peter, and A. A. Shingleton, *Optical and electrical characterisation of CdS thin films,* Journal of materials science **7** (1996) 119-125

# Discussion and Conclusions

## 7.1 Discussion and Conclusions

The work in this thesis has principally been concerned with the investigation of optical and structural properties of single crystal and polycrystalline thin films CdS. Characterisation was performed using several methods including TEM combined with cathodoluminescence, PL spectroscopy, GIXRD. This chapter summarises the main findings of this work and gives some suggestions for future work. However, to begin with, the details of the CL formation modelling are outlined below followed by a quantitative study of noise in the TEM-CL instrument.

In Chapter 4 a model was developed for predicting the spatial distribution of cathodoluminescence (CL) formation for a focused electron beam incident on a thin cross section of a multi-layer system. This model was initially based on the convolution method described by Rechid et al. [1]. It was considered that the CL originated from both electron stimulation and its accompanying X-rays. To use a direct convolution method it is necessary to know the generation function of electron-hole pairs for the beam being at any position along a multi-layer system. For X-ray excitation sources, it was found that the broadening of the convolved peak depends highly on the mass attenuation coefficient (see section 4.6.3.2). For direct

electron excitation, by assuming that the generation volume of electron-hole pairs was Gaussian, it was seen that the broadening of the convolution peak (CL signal) depends highly on the standard deviation (or FWHM) of the Gaussian. Further investigations are required in order to apply this convolution method: such as determining the electron beam excitation volume as a function of the electron beam position using the method developed by Rechid et al. [1] or else in conjunction with simulation of electron-solid interactions using Monte-Carlo software, defining the modelling parameters.

A simple experiment was performed to investigate the limits of CL image contrast by measuring the signal-to-noise ratio. It was found to be low when the scanning transmission electron microscope was operating at high magnifications. This signal-to noise ratio decreased with the magnification: below the magnification of 3000 the CL signal was five times higher than the noise, whereas at higher magnification the signal-to-noise ratio tended to a value of 1.0. Studies based on the Rose visibility criterion [2] were carried out (see section 4.7). This revealed some limitations for acquiring CL images. The origin of the noise is still undefined.


In Chapter 5, a preliminary study of the viability of combined TEM-CL apparatus in the study of CdS for solar cell applications has been presented. Prior to commencing combined TEM-CL investigations of CdS it was essential to characterise the influence of ion beam thinning on its luminescence spectrum. A comparison of photoluminescence and cathodoluminescence spectra showed that $Ar^+$ and $I^+$ ion beam thinning used in thin foil TEM specimen preparation changed the emission spectrum of the CdS: there was an increase of the yellow (Y) emission (594nm) with both $Ar^+$ and $I^+$ ion beam thinning. However CL spectra recorded from CdS did not contain the red band (734nm) that was easily detected in PL spectra of the same samples. Its absence was tentatively ascribed to the excitation density in CL, since this was 7 orders of magnitude higher than in PL.

CL emission from CdS was observed to degrade under illumination from 80-200 keV electrons. At the electron dose levels investigated (up to $10^{23}$ e$^-$/cm$^2$) the degradation process was shown to be consistent with the introduction of non-radiative recombination centres. The lower STEM dose

rate in comparison to that of CTEM was demonstrated to degrade the CL from CdS at a much slower rate and is therefore recommended for initial specimen investigations and spectral acquisition/imaging before diffraction contrast imaging.

Linear image contrast features in STEM-CL images of CdS were correlated directly to dislocation images obtained in CTEM and STEM mode. However, the image contrast was weak in STEM-CL. Assessment of the imaging conditions using the Rose criterion [2] indicated that this CL work was done under conditions close to the limits of visibility for 5% contrast, and this accounted for the weakness of the contrast obtained. This was attributed to the low signal-to-noise ratio at high magnification found in chapter 4. In further work, enhancement of the image contrast by optimisation of the signal excitation could be carried out. Samples of solar cell material shall be investigated.

In Chapter 6, optical and structural properties of thin film CdS grown by chemical bath deposition (CBD) and metalorganic vapour deposition (MOCVD) were characterised using optical transmittance, photoluminescence, SEM, GIXRD and TEM.

Three types of samples were produced: a) as grown CdS, b) films annealed in air at 400°C for one hour and c) films with 150nm layer of evaporated $CdCl_2$ then annealed in air for 1 hour. Both post-growth treatments resulted in a decrease of energy bandgap, which was unlikely to have been caused by the phase change from cubic to hexagonal (see section 6.2.1). It also showed an enhancement of crystallinity and a modest increase in grain size after being post-growth treated. From the GIXRD data analysis, the untreated CBD films had a maximum grain size of 20 nm, while air annealed and $CdCl_2$ treated samples exhibited a maximum grain size of 25.8 nm and 26 nm respectively.

The influence of growth parameters such as the II/VI ratio and the growth temperature have been investigated on the optical and structural properties of MOCVD CdS. The crystalline quality of CdS thin films was related to the II/VI source gas mole ratio and the growth temperature. It was found that the FWHM of the (002) preferred orientation was smaller for

growth temperature above 300°C. GIXRD data analysis showed that the CdS structure remained hexagonal. From the TEM and photoluminescence measurements, it was concluded that the thin film grown at 330°C with a II/VI ratio of 0.78 revealed better crystallinity and the largest grain size of ~97 nm.

Both as-deposited CBD and MOCVD CdS films presented a hexagonal structure with a strong preferred orientation in the [002] direction. The full width at half maximum (FHWM) depends on the method of CdS film growth. The lower FWHM values of the (002) plane obtained for MOCVD-grown CdS films indicated that they have better crystallinity than CBD films. This was also confirmed by PL spectroscopy, which showed that CBD films have a defect band (red band) attributed to vacancies of sulphur, while in MOCVD films excitonic transitions were observed. The latter indicates a higher crystallinity (see section 6.3.2). The deficiency of sulphur in CBD-grown CdS may influence the interdiffusion processes in CdTe/CdS-based solar cells. This interdiffusion is known to play an important role not least due to its influence on optical absorption in the structure caused by the associated bandgap changes [3]. The SEM images of the CBD films showed that thermal stress relief on annealing resulted in the formation of fissures within the layers. These fissures could affect the optimal operation of the solar cell device as pinholes would. From TEM studies, grain sizes were larger for as-deposited MOCVD (i.e., 97 nm) than CBD films (i.e., 26 nm). Hence, MOCVD CdS films might be expected to be more suitable for solar cell devices than CBD films. Nevertheless, high efficiencies of 16.5% and 16.0 % have been previously measured for CBD and MOCVD-grown CdS, respectively [4, 5].

# 7.2 References

1.  J. Rechid, A. Kampmann, and R. Reineke-Koch, *Characterising superstrate CIS solar cells with electron beam induced current,* Thin Solid Films **361-362** (2000) 198-202
2.  P. J. Goodhew and F. J. Humphreys, *Electron microscopy and analysis.* 2nd edition (1988) Taylor & Francis
3.  K. Durose, P. R. Edwards, and D. P. Halliday, *Materials aspects of CdTe/CdS solar cells,* Journal of Crystal Growth **197** (1999) 733-742
4.  T. Aramoto and H. H. Seiji Kumazawa, Takashi Arita, Satoshi Shibutani, Tuyoshi Nishio, Junji Nakajima, Miwa Tsuji, Akira Hanafusa, Takeshi Hibino, Kuniyoshi Omura, Hideaki Ohyama, and Mikio Murozono, *16.0% Efficient Thin-Film CdS/CdTe Solar Cells,* Japanese Journal of Applied Physics, Part 1 **36** (1997) pp. 6304-6305
5.  X. Wu, J. C. Keane, R. G. Dhere, C. DeHart, D. S. Albin, A. Duda, T. A. Gessert, S. Asher, D. H. Levi, and P. Sheldom, *16.5 % Efficient CdS/CdTe ploycrystalline thin-film solar cell,* 17th European Photovoltaic Solar Energy Conference, Munich, Germany, (2001)

# Appendix A

## A.1 Convolution for X-Ray Source

program threelayers07

```
implicit none              ! No implicit variable types - declare everything!!

! Declarations:

real, allocatable, dimension(:) :: func1,func2,conv12 ! allocatable arrays
real            :: limit,resolution
integer         :: half_size
integer         :: n,m,nm                              ! Loop counters
real   :: x                                    ! Real positions on number line
real            :: A,mac1,mac2,mac3,B,t0,t1,t2          ! Constants

! Main program:

! Set constants
WRITE(*,*)'X-rays source: I=Io*exp{-factor*x}'
WRITE(*,*)'Amplitude Io?'
READ(*,*)A
WRITE(*,*)'Layer A,factor A?'
READ(*,*)mac1
WRITE(*,*)'Layer B,factor B?'
READ(*,*)mac2
WRITE(*,*)'layer C,factor C?'
READ(*,*)mac3
WRITE(*,*)'Position of the beam?'
READ(*,*)t0
WRITE(*,*)'Position of the first interface?'
READ(*,*)t1
WRITE(*,*)'Position of the second interface?'
READ(*,*)t2

! Set constant function 2
WRITE(*,*)'Amplitude of the window?'
READ(*,*)B

! Set the resolution of sampling
WRITE(*,*)'Resolution of sampling?'
READ(*,*)Resolution
```

```fortran
! Set limit of the function
WRITE(*,*)'Limit?'
READ(*,*)limit


! Calculate size of arrays
    half_size=int(limit/resolution)+1

! Allocate the arrays
allocate(func1(-half_size:half_size))
allocate(func2(-half_size:half_size))
allocate(conv12(-half_size:half_size))

! Now we want to put some numbers into func1 and func2...
! Loop over array elements

do n=-half_size,half_size

    ! Work out where this point is on the real number line
    x=real(n)*resolution

    ! func1 will be exp(-|factor*x|)

    ! Emission beam in layer A
if (t0+0.0<0.0+t1) then

    if (x<=0.0+t1) then
       func1(n) = A*exp(-abs(mac1*(x-t0)))
    end if

    if (t1+0.0<=x.and.x<=0.0+t2) then
       func1(n)=A*exp(-abs(mac1*(t1-t0)))*exp(-abs(mac2*(x-t1)))
    end if

    if (t2+0.0<=x) then
       func1(n)=
       (A*exp(-abs(mac1*(t1-t0))))*exp(-abs(mac2*(t2-t1)))*exp(-abs(mac3*(x-t2)))
    end if

end if

    ! Emission beam in layer B
if (t1+0.0<=t0.and.t0<=0.0+t2) then

    if (x<=0.0+t1) then
       func1(n) = A*exp(-abs(mac2*(x-t0))) * exp(-abs(mac1*(x-t1)))
    end if

    if (t1+0.0<=x.and.x<=0.0+t2) then
       func1(n)=A*exp(-abs(mac2*(x-t0)))
    end if

    if (t2+0.0<=x) then
       func1(n)= A*exp(-abs(mac2*(t2-t0))) * exp(-abs(mac3*(x-t2)))
    end if
```

```
end if

        ! Emission beam in layer C
if (t2+0.0<=0.0+t0) then

        if (t2+0.0<=x) then
           func1(n)= A*exp(-abs(mac3*(x-t0)))
        end if

        if (t1+0.0<=x.and.x<=0.0+t2) then
           func1(n)= A*exp(-abs(mac3*(t2-t0))) * exp(-abs(mac2*(x-t2)))
        end if

        if (x+0.0<=0.0+t1) then
           func1(n)=
           A*exp(-abs(mac3*(t2-t0))) * exp(-abs(mac2*(t1-t2))) * exp(-abs(mac1*(x-t1)))
        end if

end if


        ! func2 will be B for w_min<x<w_max, and 0 elsewhere

        if (t1+0.0<=x.and.x<=0.0+t2) then
           func2(n)=B
        else
           func2(n)=0.0
        end if

end do   ! Functions now defined


        ! Now lets calculate the convolution

        conv12(:)=0.0

        do n=-half_size,half_size

          do m=-half_size,half_size
             nm=m+n
          if (abs(nm)>half_size) cycle                     ! i.e. quit do-loop
             conv12(n)=conv12(n)+func1(m)*func2(nm)*resolution
          end do

        end do


! Open files with x, func1, func2 and conv12

        open(unit=20,file='summary_out.txt')

          do n=-half_size,half_size
             x=real(n)*resolution
             write(20,*) x,func1(n),func2(n),conv12(n)
          end do

        close(20)
```

```
open(unit=20,file='parameters_out.txt')

    write(20,*)'Summary of parameters:'
    write(20,*)
    write(20,*)'X-rays source'
    write(20,*)'Io                                    ',A
    write(20,*)'(μmρ)a. of layer A                    ',mac1
    write(20,*)'(μmρ)b of layer B              ',mac2
    write(20,*)'(μmρ)c of layer C              ',mac3
    write(20,*)'Position of beam              ',t0
    write(20,*)'1st interface position        ',t1
    write(20,*)'2nd interface position        ',t2
    write(20,*)
    write(20,*)'D(x) function'
    write(20,*)'Amplitude                             ',B
    write(20,*)
    write(20,*)'Resolution                            ',resolution
    write(20,*)'Limit                         ',limit

close(20)
```

*! Should free up memory from allocatable arrays*

```
deallocate(func1)
deallocate(func2)
deallocate(conv12)
```

**end program threelayers07**

# A.2 Convolution for Electron Source

**program Gaussian1**

```
implicit none   ! no implicit variable types - declare everything!!

! Declarations:
! allocatable arrays
real, allocatable, dimension(:) :: func1,func2,conv12,parameters
real     :: resolution,limit
integer :: half_size
integer :: n,m,nm                          ! Loop counters
real :: x                                  ! Real positions on number
line
real :: w_min,w_max,B,FWHM,SD,func10,G,u        ! Constants

! Main program:

! Set constants

! Set constant function 1
WRITE(*,*)'Function 1: Gaussian function'
WRITE(*,*)'FWHM?'
READ(*,*)FWHM
WRITE(*,*)'Amplitude?'
READ(*,*)G
WRITE(*,*)'mean u?'
READ(*,*)u
SD=FWHM/2.3548
func10=1.0/(SD*SQRT(2.0*3.14159265358979))*EXP(-SQRT((x)))/(2.0*SD**2))

! Set constant function 2
WRITE(*,*)'Function 2'
WRITE(*,*)'Enter the Amplitude of the window'
READ(*,*)B
WRITE(*,*)'Enter the minimum position of the window'
READ(*,*)w_min
WRITE(*,*)'Enter the maximum position of the window'
READ(*,*)w_max

! Set the resolution of sampling
WRITE(*,*)'Resolution of sampling?'
READ(*,*)Resolution

! Set limit of the function
WRITE(*,*)'Limit?'
READ(*,*)limit

! Calculate size of arrays
half_size=int(limit/resolution)+1


! Allocate the arrays
allocate(func1(-half_size:half_size))
allocate(func2(-half_size:half_size))
```

```
allocate(conv12(-half_size:half_size))
```

*! Now we want to put some numbers into func1 and func2...*
*! Loop over array elements*

```
do n=-half_size,half_size

   ! work out where this point is on the real number line
   x=real(n)*resolution

   ! func1 will be Gaussian
       func1(n)=1.0/(SD*SQRT(2.0*3.14159265358979))*EXP((-(x-
       u)**2)/(2.0*SD**2))*G/func10
   if (w_min+0.0<=x.and.x<=0.0+w_max) then
      func2(n)=B
      else
      func2(n)=0.0
   end if

end do   ! functions now defined
```

*! Now lets calculate the convolution*
```
conv12(:)=0.0

do n=-half_size,half_size

   do m=-half_size,half_size
     nm=m+n
     if (abs(nm)>half_size) cycle                    ! i.e. quit do-loop
     conv12(n)=conv12(n)+func1(m)*func2(nm)*resolution
   end do

end do
```

*! Write files with func1 and func2...*
*! Open file for func1, func2, conv12*
```
open(unit=20,file='response_out.txt')

   do n=-half_size,half_size
          x=real(n)*resolution
          write(20,*) x,func1(n),func2(n),conv12(n)
   end do

close(20)
```

*! Open file for parameters*

```
open(unit=20,file='parameters_out.txt')
   write(20,*)'Summary of parameters:'

   write(20,*)
   write(20,*)'Gaussian function'
   write(20,*)'FWHM            ',FWHM
```

```
write(20,*)'Amplitude              ',G
write(20,*)'Standard deviation     ',SD
write(20,*)'mean u                 ',u
write(20,*)
write(20,*)'D(x)'
write(20,*)'Amplitude              ',B
write(20,*)'W_min        ',w_min
write(20,*)'W_max        ',w_max
write(20,*)
write(20,*)'Resolution             ',resolution
write(20,*)'Limit        ',limit

close(20)

! Should free up memory from allocatable arrays

deallocate(func1)
deallocate(func2)
deallocate(conv12)
```